OH Absorption Spectroscopy to Investigate Light-Load HCCI Combustion

by

Sean J. Younger

A thesis submitted in partial fulfillment

of the requirements for a degree of

Master of Science

(Mechanical Engineering)

at the

University of Wisconsin – Madison

2005

Approved: _____

Jaal B. Ghandhi

Professor – Mechanical Engineering
University of Wisconsin – Madison

Date: _____

Abstract

Absorption spectroscopy of the OH molecule was used to examine the light-load limit of the HCCI combustion process. Optical results were compared to cylinder pressure and emissions data, with a focus on the transition from low to high engine-out CO emissions. The goal of the work was to experimentally verify a low-load emissions limit to practical HCCI combustion that has been predicted by detailed kinetic simulations.

Two diluent mixtures were used along with 100% air to create intake charges with varying specific heats in order to highlight the temperature dependence of OH formation. Peak OH concentration data show a correlation with temperature, which agrees with theory. In general, OH absorption decreased monotonically with the mass of fuel injected per cycle for all diluent cases. The absorption spectra, which were taken with 400 μs time resolution (~1.8 CAD at 600 RPM) show that OH forms during the second-stage heat release and remains in the cylinder well into the expansion stroke. Spectral resolution did not allow a temperature measurement from absorption, so temperature was measured separately. Emissions data showed low exhaust CO concentrations at high fuel rates, and higher CO concentrations at low fueling rates.

Qualitatively, the detection limit for OH coincided with the onset of increased engine-out CO emissions and the transition from strong to weak second stage heat release. These data suggest that the three phenomena are linked. As increased CO emissions are the practical limitation to the light-load operation of the HCCI engine, this transition is the light-load limit. Due to noise issues in the temperature data, the temperatures at which these transitions happened could not be determined exactly.

Acknowledgements

"And the LORD replied to Moses, 'I will indeed give you success, for you have found favor with me, and you are my friend.'" –Exodus 33:17

First and foremost, I must thank God. He led me to the University of Wisconsin, and it is by His grace alone that I have found the strength and motivation to succeed here. I thank my parents for their love, support, and willingness to help make my ends meet as I continue to avoid getting a "real job." I would not have made it through these two-plus years with my sanity intact without my girlfriend Le Ondra Clark, who is the love of my life. Thank you for encouraging and inspiring me daily.

My advisor, Dr. Jaal Ghandhi, deserves the bulk of the credit for any success this thesis earns. His guidance and experience were always appreciated and respected. He is truly a brilliant man, and a great experimentalist. As if that weren't enough, he is also an extremely nice guy who has put considerable time into making this project work. I am very happy to have had the opportunity to work with him, and I hope to be able to return his kindness some day.

Next, I need to thank my colleague Mark Schrewe. He and I started graduate school at the same time, doing similar projects on the same engine. This allowed us to work together, for the most part, and learn from each other. I'm sure that if he hadn't been here, the learning curve in the lab would have been much tougher to overcome. Thanks and good luck to you.

Dr. Tongwoo Kim deserves credit for teaching Mark and me how to run that lab. As his Ph.D. experiments were done there, he was extremely knowledgeable, and his patience and diligence were invaluable to this work. Also, thanks go to Rinaldo Augusta for showing me how to use the camera and its software, and to Laura Kranendonk for putting in extra hours helping to acquire temperature data.

Ralph Braun's expertise in machining and general ability to help with anything ERCs needed to make or fix was invaluable. If not for him, I'd probably still be looking for some tool or other. Susie Strzelec and Deanna Duerst deserve the same credit for handling administrative tasks quickly and professionally.

My past and present officemates, Ryan Rudnitzki, Tim Pfeifer, Brian Albert, and Dennis Ward were a welcome distraction from the daily grind. Thanks for listening to me gripe about how often things break in my lab, and making the time pass so quickly. I enjoyed getting to know you and the rest of the ERC students. It has been a great pleasure working with you all.

I should thank Kelly Burton and Dr. Doug Henderson, administrators of the Graduate Engineering Research Scholars (GERS) fellowship program. The GERS community made my transition to graduate school and to Madison incredibly easy. Thank you for being advocates and for putting the energy that you did into this program. Thanks also to my fellow GERS scholars. I know I will see each of your names again in the future. Keep up the good work!

In closing, I must thank Jialin Yang, Tom Kenney, and the researchers at Ford R&D who decided to use the UW as a resource for research. Their contribution to this project has been much more than just money. I'm grateful to have had the opportunity to work on it.

Table of Contents

List of Figures

1. Introduction

1.1. The Homogeneous Charge Compression Ignition (HCCI) engine.

The concept of HCCI combustion is a relatively new development in the field of internal combustion (IC) engines. This chapter will discuss some characteristics of HCCI combustion and will highlight the factors that lead to the questions this research attempts to answer.

HCCI engines essentially combine the physical operation of the gasoline spark-ignited (SI) engine and the Diesel compression-ignited (CI) engine. In short, a homogeneous air/fuel mixture is drawn into the cylinder during the intake stroke as in SI operation, and the mixture is then compression ignited as in CI operation. This process results in a new mode of IC which is entirely distinct from both gasoline SI and Diesel CI combustion [1].

1.2. Advantages over other combustion systems

The HCCI engine can run at low loads with no throttling losses because it is not restricted to operate near a stoichiometric air/fuel ratio, and can be made to operate with better emissions than a comparable Diesel engine while producing similar indicated specific fuel consumption (ISFC).

1.2.1. Diesel

The HCCI engine matches the Diesel for fuel economy at light-load because it is does not require a throttle to control load. Instead the HCCI engine accomplishes load control by varying the amount of fuel like a Diesel engine. The Diesel engine, however,

suffers from increased emissions of NOx and particulates due to the elevated temperatures caused by their high compression ratios and the stoichiometric combustion, respectively.

The other principal advantage of the HCCI engine over the more established Diesel cycle is that the intake charge is a homogeneous air/fuel mixture. High efficiency low-load operation can be achieved without locally rich regions or stoichiometric flame fronts since the homogeneity of the mixture guarantees that combustion is *locally* lean in addition to overall lean [2]. The high temperatures—and thus high NOx emission—seen in the Diesel cycle are not an issue for the HCCI engine [3]. Indeed, HCCI combustion follows "low-temperature/cool-/blue-flame" hydrocarbon oxidation kinetics [3, 4, 5].

1.2.2. Gasoline SI

1.2.2.1. Throttling losses

HCCI's advantages over conventional gasoline SI operation are numerous. Most obvious is the facility of unthrottled light-load operation. For most engine applications, especially automotive, the engine spends nearly all of its life at part-load. In a gasoline engine, operating conditions are restricted to a very narrow band around stoichiometric air/fuel ratio. To achieve less than full output, less fuel must be injected and thus less air can be taken into the cylinder. Until very recently, throttling the intake air has been the only solution.

Throttling is a very effective solution to the load control problem in an SI engine, but it creates other issues. First, the purpose of any throttle is to create a pressure drop in a flow passage. An internal combustion (IC) engine with atmospheric pressure (at best) upstream of the throttle will result in a vacuum downstream of the throttle at the intake

manifold. Any decrease in intake pressure can be associated with a loss due to greater pumping work [5]. In addition, the throttled intake charge, having less mass, also has less momentum available for mixing through swirl and tumble processes than an unthrottled "full" charge.

For these reasons, gasoline engines are most efficient at "wide open throttle" (WOT) where the throttle is essentially eliminated. So whenever a throttle can be bypassed, either by being absent from the system or by being as open as possible, there is a benefit to be had. The HCCI engine receives this benefit automatically.

1.2.2.2. Rate of heat release

Another advantage of HCCI combustion over the conventional SI engine is the high heat release rate due to spontaneous ignition at many points in the cylinder and the relative unimportance of the flame front propagation speed. The lack of a time lag due to a sparked flame kernel generation, a rate-limiting flame speed, or a related mixing constraint causes a fast heat release which is more thermodynamically efficient.

Clearly this type of engine holds the possibility of a "best of both worlds" approach to the future of internal combustion. As such, it is desirable from a research perspective to investigate further the operation and limits of the HCCI engine for both light- and heavy-duty applications.

1.3. Drawbacks and limitations

Some concerns about the practicality of the HCCI engine exist. At the moment, there is no good method for controlling the start of HCCI combustion. In the SI engine, the spark starts combustion and being an electrical impulse can be easily controlled even

on a cycle-to-cycle basis, using a modern computerized engine control unit (ECU). In the Diesel engine, conditions are made such that the fuel burns shortly after it is injected due to elevated temperatures and pressures created by their characteristically high compression ratios. The start of combustion is thus controlled by when that fuel is injected.

The HCCI engine relies on an autoignition process whose start time relative to the cycle depends on many variables including, but not limited to: charge homogeneity, temperature history, exhaust gas recirculation (EGR) ratios, fuel concentration and fuel type, compression ratio, cylinder wall temperature, and severity of wall quenching [3]. In short, there is no way to force the combustion to start when it is desirable to do so [3]. Indeed, no outside influence can be exerted on the air/fuel mixture after intake valve closing. As power conversion depends critically on the combustion timing, this is somewhat problematic. Control strategies are being developed, mainly focusing on controlling charge temperature through direct heating, turbocharging, and EGR percentage.

It is desirable to make the HCCI engine run at conditions as lean as possible so as to receive the best fuel economy at the light-load situations encountered in most driving. A limit does exist, however, and this limit has been shown to adversely affect the emissions. It has been established that low in-cylinder temperatures result in high levels of unburned hydrocarbon (uHC) and carbon monoxide (CO) emissions [6]. Additionally, it is known that under increasingly light load (lean operation), the HCCI engine sees decreasing peak combustion temperatures [3]. Measurement of CO emissions has shown

that for all fuels tested at a wide range of operating conditions, incomplete CO oxidation in the bulk mixture is the cause of high CO emission at low equivalence ratios [7].

Computerized chemical kinetic models have been employed to help establish the light-load limit for HCCI combustion. It has been shown that the light-load limit based on an acceptable CO emission level corresponds to a peak charge temperature of 1500K. This limit remains the same regardless of fuel type and combustion phasing [7].

This computational analysis is an important first step in establishing the light-load limit of the HCCI engine. The goal of this thesis work is to use a quantitative measurement of OH concentration to measure the relative completeness of HCCI combustion and move toward an experimental verification of the calculated low-load limit.

2. Background

2.1. HCCI Development

This chapter is meant to present the foundation of knowledge upon which this research is built. Previous work in the field will be discussed with a focus on optical techniques and quantitative concentration analysis.

2.1.1. Early Work

2.1.1.1. Two-Stroke HCCI

Onishi *et al.* and Noguchi *et al.* pioneered HCCI combustion in two-stroke IC engines in the late 1970s. Both researchers were able to show that the HCCI concept was workable and that improvements in fuel economy, emissions, and cycle-to-cycle variation (CCV) could be achieved. The basis for their discovery was the study of auto-ignition and an attempt to put that abnormal—and usually undesirable—phenomenon to good use [1, 4].

Both of the Japanese teams—Onishi by Schlieren imaging and Noguchi by use of a quartz window and high-speed camera—showed that HCCI combustion was initiated at many points in the combustion chamber. While Onishi concluded that flame front propagation was not discernable, Noguchi *et al.* claimed that their flames spread very quickly in all directions. Both teams saw their methods of compression igniting a homogeneous air/fuel mixture result in a combustion duration much shorter than in other IC engines [1, 4].

Onishi *et al.*, who termed their combustion method "active thermo-atmosphere combustion" (ATAC) found that HCCI worked best in operating regimes where the ratios

of fresh charge to exhaust gas recirculated (EGR) was close to unity. Here the mean charge temperatures are highest, and combustion was easy to initiate. ATAC/HCCI failed in their engine at light loads due to charge temperatures insufficient for combustion completion. At high loads, lack of a sufficient residual gas quantity led to low charge temperatures and caused misfire. These results are summarized in Figure 2.1.

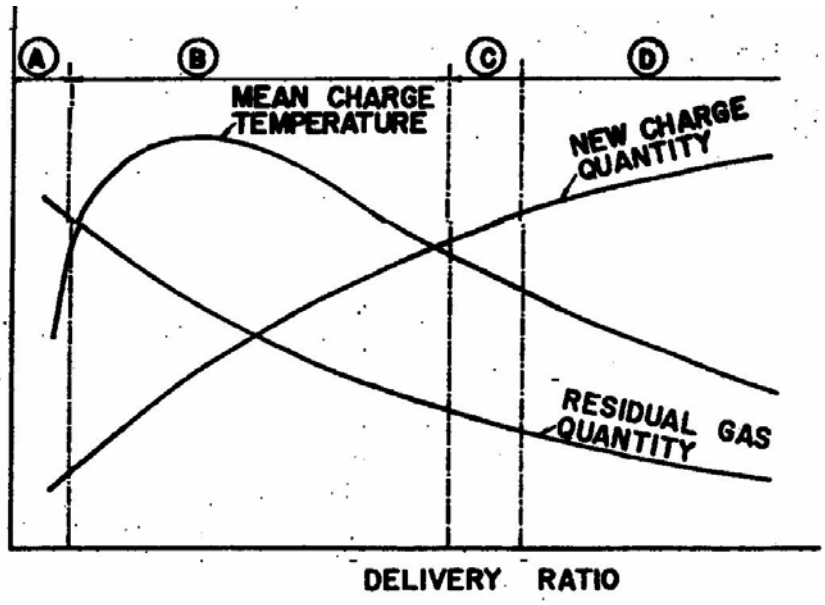

Figure 2-1. A performance map showing the influence of residual quantity and mean charge temperature at beginning of compression. Reprinted from [1].

In region A, gas temperatures were too low to sustain combustion. The most favorable conditions for ATAC/HCCI are found in region B at the maximum charge temperatures. Region C is where both ATAC/HCCI and spark-ignition can occur interchangeably. Conventional spark-ignition combustion occurs in region D.

The most important data from Onishi, from a fuel economy standpoint, was that his group was able to achieve stable combustion with air/fuel ratios from 11:1 to 22:1 which showed considerable promise for operation far lean of stoichiometric at 14.7:1. Their data show a significant decrease in fuel consumption at operating conditions run in

ATAC/HCCI mode compared to the unmodified two-stroke. To quote their 1979 paper: "It is evident that fuel consumption is remarkably better than … conventional two- or four-stroke engines." [1] The group also found that unburned hydrocarbon (uHC) emissions were significantly decreased, but due to the nature of two-stroke engine design high uHC emissions are systemic and these results will not be discussed here.

Noguchi *et al.* called their HCCI method "Toyota-Soken" (TS) combustion after Toyota Motor Company and Nippon Soken, Inc., the employers of the authors. They noted that uHC emissions were drastically reduced, and that fuel consumption improved by 40% compared to the conventional two-stroke SI engine. They went further in depth in detection of reactive products of combustion using chemiluminescence imaging, specifically CHO, HO2, O, H, CH, C2, and OH [4].

Noguchi's team used knowledge of OH radical appearance at the initial stages of ignition to identify the start of combustion, and they were able to confirm that with their camera images. Their results showed that CHO, HO2, and O radicals appear before OH and the start of combustion. They concluded that these radicals must appear from cracking of fuel components in the EGR, and that these radicals serve as ignition kernels for TS/HCCI combustion [4].

2.1.1.2. Four-Stroke HCCI

Najt and Foster in 1983 first confirmed experimentally that HCCI operation could be achieved reliably in a four-stroke engine at a relatively wide range of fuel types, loads, EGR ratios, and intake air temperatures. The Compression Ignited Homogeneous Charge (CIHC) engine, as they called it, exhibited auto-ignition that was not violent like a knock,

but rather a smooth and continuous energy release. Furthermore, CIHC operation caused no harm to the engine like a prolonged knocking condition would [8].

Najt and Foster saw no evidence of flame front propagation or "hot spots" of ignition—combustion was found to be essentially homogeneous. Najt and Foster used knowledge of temperature-dependent alkane reaction routes to study the CIHC combustion process on a chemical kinetic basis. This was significant because HCCI combustion falls across two of the three established reaction regimes. Briefly, these regimes are:

1. Below 750K: chain propagation involving O2 yielding partially oxidized species
2. Between 800 and 950K: chain propagation yielding alkenes and HO_2 radicals
3. Above 1000K: thermal decomposition by Carbon-Carbon bond breakage

The compression processes of CIHC combustion were found to occur at less than 950K, and the ignition and main heat release above 1000K, placing the kinetics in (2) and (3) from the above list, thereafter referred to as the "low temperature" and "high temperature" regimes. Other important results are summarized below [8]:

- Increased compression ratios allow for lower intake temperatures and/or lower delivery ratios.
- Energy release rates (ERR) increase with compression ratio, and become violent around a 10:1 compression ratio.
- As equivalence ratio approaches stoichiometric from the lean side, ignition advances and ERR increases.
- Engine speed has no direct effect on fuel kinetics, but to avoid misfire at high speeds reaction rates must be increased through higher gas temperatures.

- Increased EGR has a large effect on ignition advance because reaction kinetics are susceptible to temperature changes.
- Chemical species in the recirculated exhaust do not enhance the ignition process—the contribution of EGR is mainly to charge temperature.

By 1989, the term for a compression ignited, homogeneous charge engine had settled to "HCCI" which has been used widely since. In that year, Thring was the produced more detailed maps of HCCI operating conditions than that shown in Figure 2.1. His maps, reprinted in Figures 2.2-2.3 were fully quantitative, and created based on fuel equivalence ratio versus percent EGR in an engine running on either gasoline or Diesel fuel with a 15:1 compression ratio [2].

The map shows a satisfactory region bounded by three unsatisfactory conditions: the "misfire region", the "power-limited region," and the "knock region." In the knock region, combustion was extremely rapid and violent leading the author to conclude that the engine was, in fact, knocking. This agreed well with findings from Najt and Foster about knocking conditions occurring at higher compression ratios and lower EGR percentages.

Misfire and power-limited regions were characterized by excessively rich and lean conditions, respectively, in combination with too much EGR. Thring noted that combustion was still steady and smooth in the power-limited region, and that the only difficulty was indicated power not exceeding friction power. These conditions did not occur until equivalence ratios less than 0.4 were encountered, hinting at the light-load

applicability of the HCCI engine [2]. The favorable part of the map agrees with the findings of Onishi concerning EGR, temperature and equivalence ratio.

When engine speeds were slowed, the map changes such that the misfire region is pushed to higher equivalence ratios such that it is no longer of interest. The satisfactory region is expanded in the range of moderate EGR, and the knock region is pushed to higher equivalence ratios. Thring noted this last point as interesting since the tendency for an SI engine to knock is increased at lower engine speeds due to the greater time available for knock to occur in the end gases. He states in that paper, however, that the entire HCCI charge can be considered an "end gas," and there is no chance for pre-knock reactions to occur outside of a flame front since the entire charge ignites at essentially the same time [2].

Thring's engine maps are reproduced in Figures 2.2 and 2.3. Of interest is the dotted line overlay of Figure 2.2 on Figure 2.3, which illustrates the changes in the shape and size of the satisfactory region as engine speed is reduced.

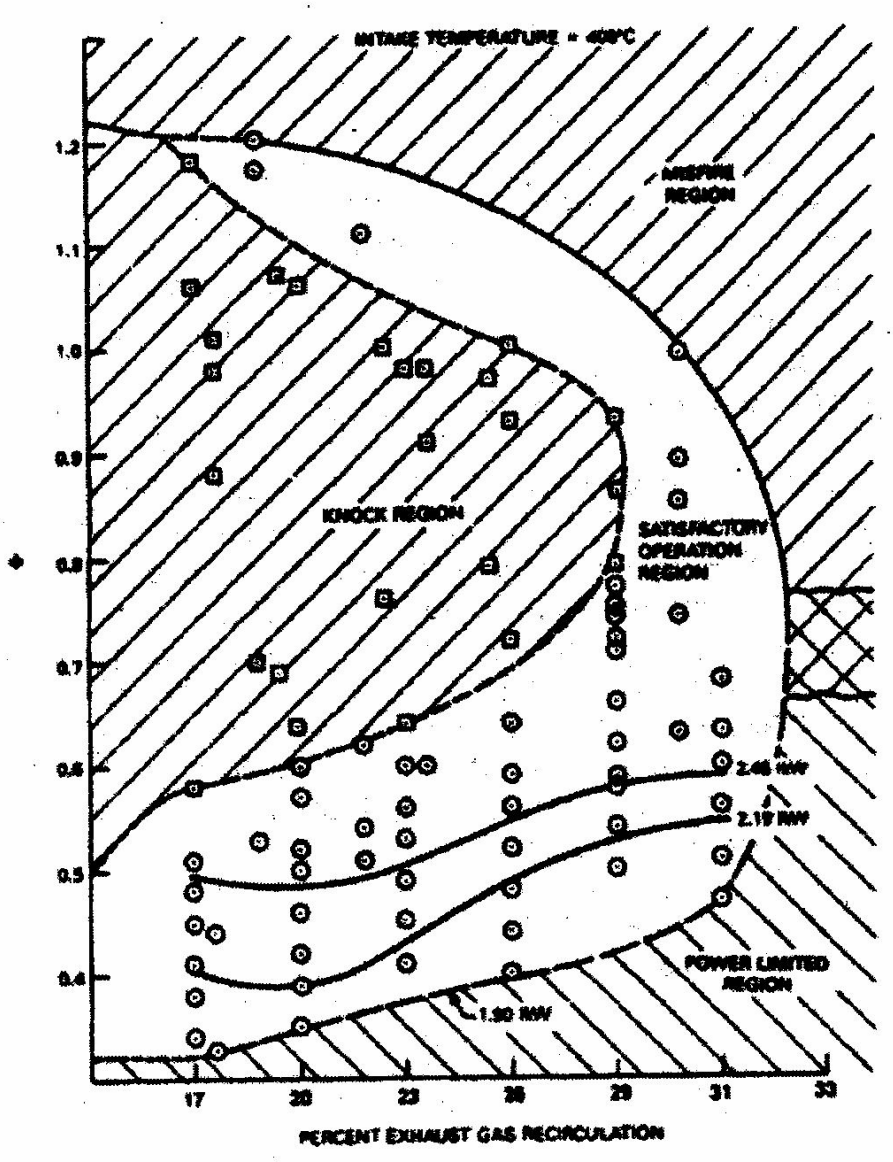

Figure 2-2. HCCI Operation map: 1500 RPM, $T_{in} = 400°C$. Reprinted from [2].

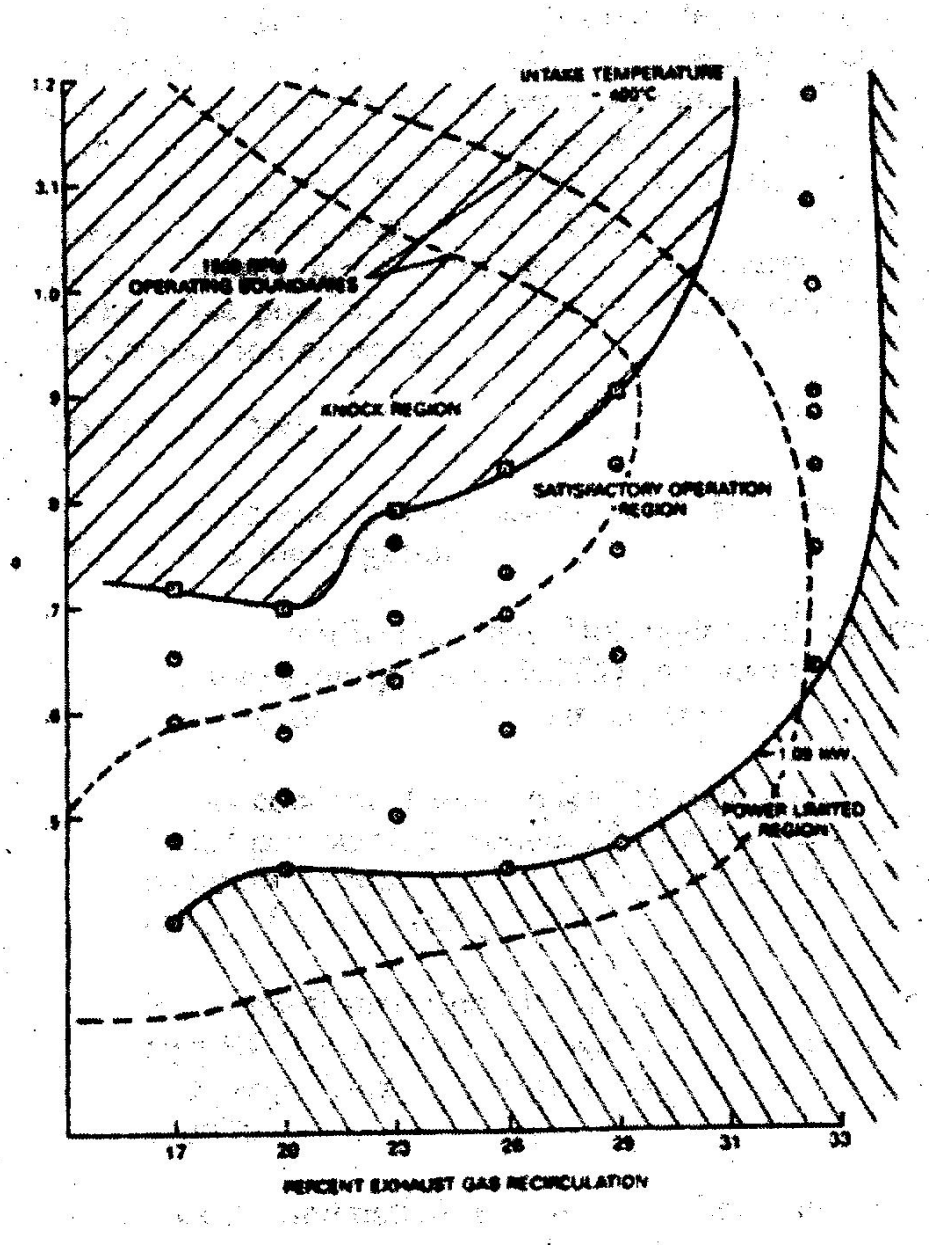

Figure 2-3. HCCI Operation map: 1000 RPM, $T_{in} = 400°C$. Reprinted from [2].

Under Thring's testing conditions, and considering the definition of his "power-limited" region, the light-load limit from a power perspective seems to occur at an equivalence ratio of 0.4 to 0.5 [2].

2.2. Emissions and the $CO \Rightarrow CO_2$ oxidation reaction

2.2.1. HCCI Emissions

The biggest emissions advantage of the HCCI engine is a 90-98% improvement in NOx emission which is noted by several sources [9, 10]. This is due to the low-temperature nature of the HCCI combustion process which slows the thermal NOx mechanism down considerably. Stanglmaier and Roberts developed a numerical model of NOx production from HCCI combustion of Diesel fuel. They were then able to compare this result to those from a standard Diesel simulation. These results are presented in Figure 2.4.

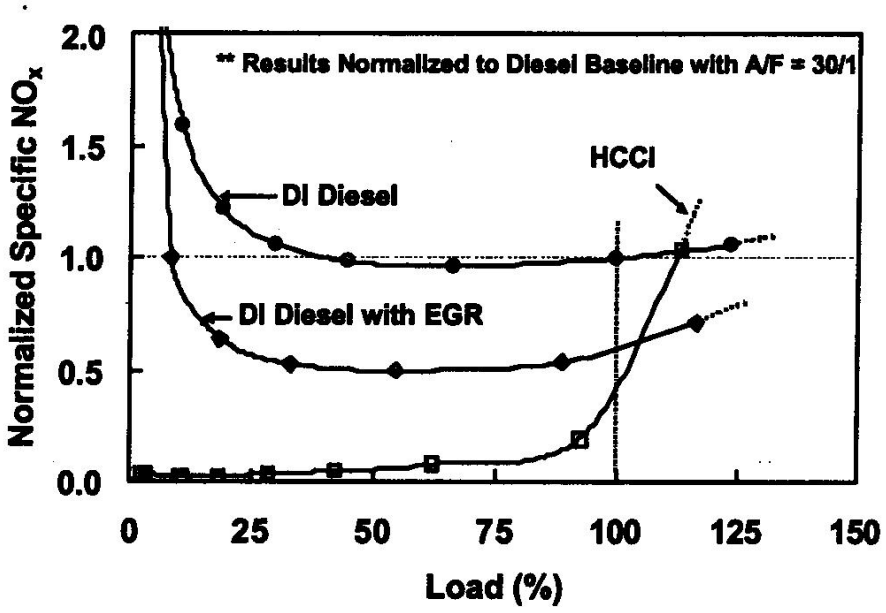

Figure 2-4. Predicted NO_x Emissions vs. load for HCCI and Diesel combustion. Reprinted from [3].

HCCI does suffer from higher uHC and CO emissions than a comparable Diesel engine. According to Najt and Foster, problems with uHC should be tied to insufficient cylinder temperatures as the C-C bond breakage occurs from the high-temperature stage

of HCCI combustion. CO emission occurs because of an insufficient oxidation rate, which is again dependent on temperature. So the same low cylinder temperatures that are beneficial for low NOx are the cause of the incomplete combustion of the fuel [3, 5, 7].

2.2.2. The role of the OH radical in combustion reaction kinetics

The rate of CO oxidation in the HCCI engine is primarily determined by three reactions [7, 8, 11]:

$CO + OH \Rightarrow CO_2 + H$ (78% of total CO2) (1)

$CO + HO_2 \Rightarrow CO_2 + OH$ (7.2% of total CO2) (2)

$CO + O_2 \Rightarrow CO_2 + O$ (1.5% of total CO2) (3)

$O + H_2O \Rightarrow OH + OH$ (4)

$H + O_2 \Rightarrow OH + O$ (5)

It is obvious upon inspection that the presence of the OH radical is crucial in order to achieve near-complete combustion of the fuel carbon. It combines directly with CO in reaction (1), which is most important in terms of total CO2 production, and it is a product of the chain branching reaction (2). Reactions (4) and (5) are included for completeness and illustrate the production of the OH radicals. OH concentrations drop significantly with decreasing combustion temperatures, and HCCI combustion temperatures drop with decreasing load, so there must be a temperature at which the OH concentration becomes so low that sufficiently complete CO oxidation is impossible [3, 7]. Thus, the practical light-load limit for HCCI combustion is the temperature limit for complete combustion.

2.2.3. Computational analysis of the light-load limit

Dec and Sjöberg studied the relationship between HCCI combustion temperatures and CO emissions for several fuels under various conditions. They noted that, in general, as fuel equivalence ratio is reduced, the amount of exhaust CO increases. In some cases, such as those on the order of an idling Diesel engine, more than 60 percent of the fuel carbon remains at the CO stage. These results are depicted in Figures 2.5 and 2.6. The first plot shows experimental validation of the technique, and the second shows results of a numerical model using a single-zone CHEMKIN-III analysis for a wider variety of fuels. The temperature values plotted are bottom dead center (BDC) temperatures which were required to place the 50 percent burn at top dead center (TDC) [7].

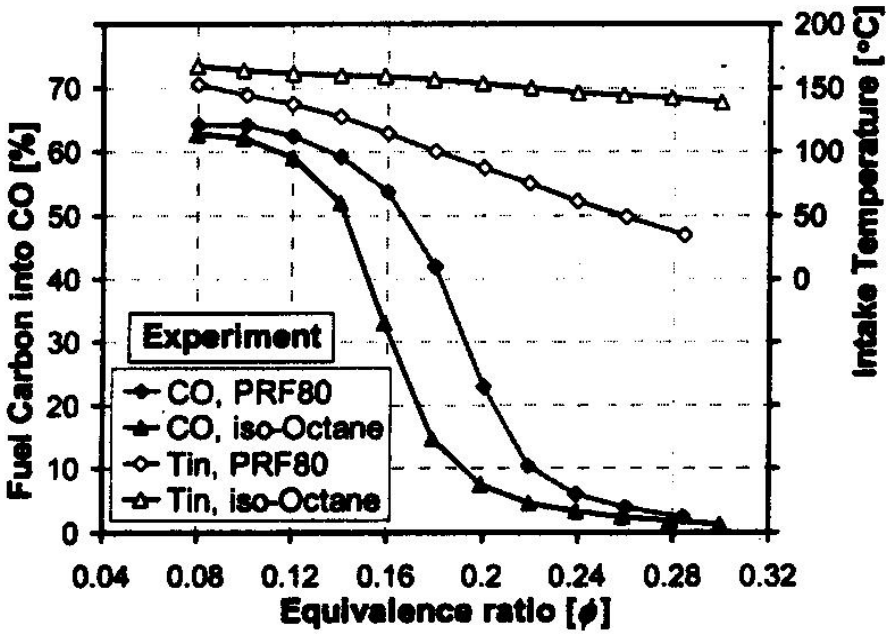

Figure 2-5. Experimentally measured exhaust CO and intake temperature vs. equivalence ratio for two fuels. Reprinted from [7].

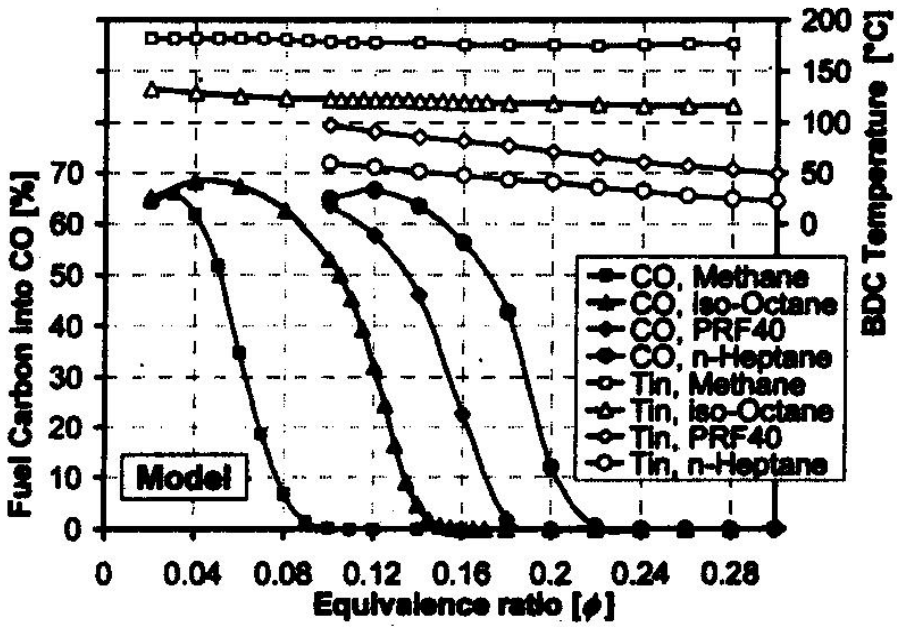

Figure 2-6. Modeled exhaust CO and intake temperature vs. equivalence ratio for four fuels. Reprinted from [7].

One point to note from these plots is that the incomplete reaction occurs at higher equivalence ratios in a fuel with a lower octane rating. At first this seems counterintuitive, as the lower octane fuel should want to burn more easily than the higher octane fuel. The explanation offered by the authors is that the higher fueling rate is necessary for PRF80 to reach the same combustion temperatures as iso-octane, and this compensates for the lower bulk gas temperatures encountered during compression. Fuels which are harder to auto-ignite necessarily require a higher intake temperature to place 50 percent burn at TDC [7].

Figure 2.7 replots modeled CO data for all fuels versus peak charge temperature. All curves in this graph "collapse" on each other whereas they are essentially separate in Figure 2.6. So the correlation to temperature is stronger than to equivalence ratio for all

fuels tested, and this confirms that peak combustion temperature is the most important metric in analysis of HCCI combustion completion.

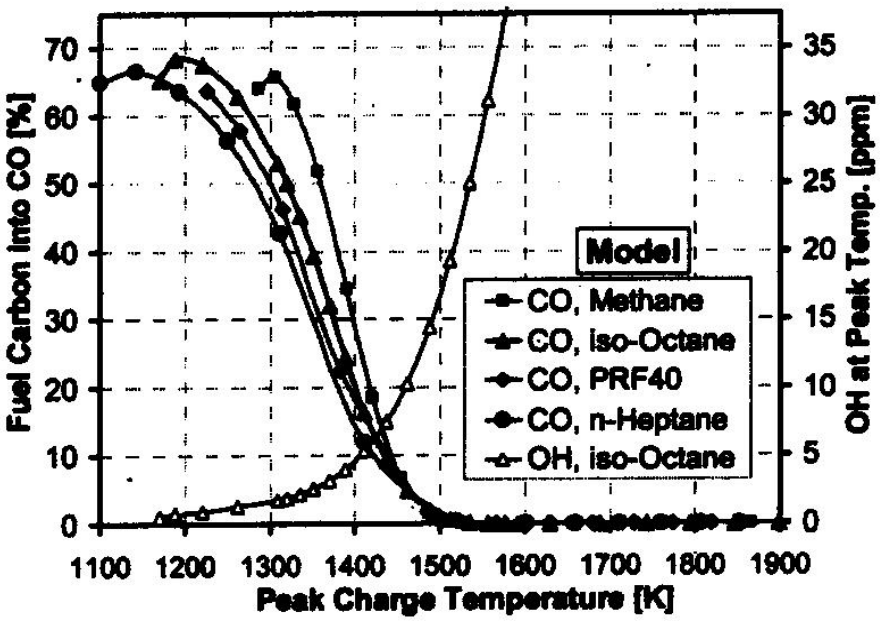

Figure 2-7. CO emission and OH concentration data for all fuels vs. peak charge temperature. Reprinted from [7].

Also of note here is the concentration of OH plotted against peak charge temperature on the right-hand vertical axis. The trend of increasing OH concentration with increasing charge temperature is clear [7].

The only difference between the modeled and experimental data is a more gradual rise in CO emission with decreasing fueling rate in the experimental case. The authors offer that this is due to the presence of crevice volumes and a thermal boundary layer in the physical engine, which creates temperature conditions that are less than optimal for CO oxidation compared to the bulk gas temperature. However, this fact motivated the

choice of a single-zone model since that was necessary to resolve the critical combustion temperature [7].

Because the correlation between temperature rise and percent CO emission was so strong based on their model prediction, Dec and Sjöberg predicted that to achieve HCCI combustion which is what they call "marginally complete" (less than one percent fuel carbon left as exhaust CO) a peak charge temperature of 1500 K is required at 1200 RPM and 18:1 compression ratio [7]. This minimum peak temperature can be considered the calculated "light-load limit" of practical HCCI engine operation without catalysis for all fuel types.

2.3. Quantitative species analysis

2.3.1. Absorption Spectroscopy

Absorption spectroscopy is a method of determining chemical concentration in a gaseous mixture using relative intensities of incident and transmitted light. It is based on the research of Johann Heinrich Lambert and August Beer. Their discoveries led to the development of the "Lambert-Beer Law", which relates the absorbance to the concentration of that substance, the pressure, and the path length that the incident light transverses.

$$Transmission = 1 - absorption = \frac{I_{trans}}{I_0} = \exp(-absorbance) = \exp(-k_\nu PXL) \qquad (2.1)$$

Where P, X, and L represent pressure, mole fraction, and path length, respectively. The proportionality constant, k_ν, is a function of wavelength, and is specific to the substance

based on its quantum mechanical properties. k_ν is also a function of temperature and pressure through their effects on line shape and number density, respectively.

2.3.2. Absorption Spectroscopy in engines

Corcione *et al.* used absorption spectroscopy and laser induced fluorescence to detect concentrations of OH and NO, respectively, in a Diesel engine. They were able to show the changes in concentration gradients of these two chemicals over time using the Lambert-Beer Law and knowing local temperatures. Figure 2.8 shows the absorption cross section of the OH molecule, which is the same species used for this research [12].

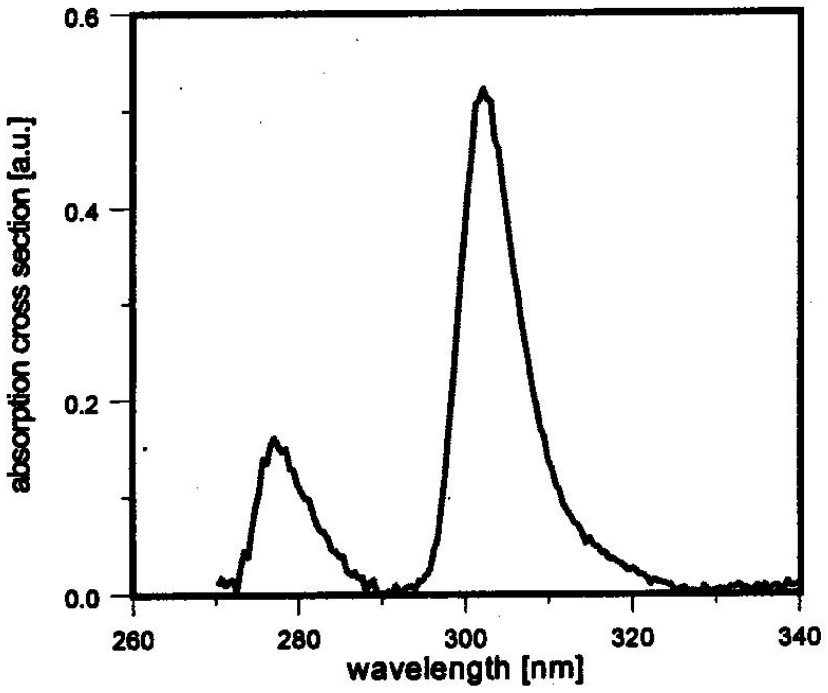

Figure 2-8. Ultraviolet Absorption cross-section. Reprinted from [12].

By measuring the absorbance as a function of time, Corcione's group was able to show the point in the cycle where OH first appears in the "cool flame" regime of Diesel combustion. In crank angles, this corresponded to about 15º before top dead center

(BTDC). Relative to events in the cylinder, OH appeared about 0.5º after the start of combustion. They then tracked an increase in OH concentration to the start of the "hot flame" period and saw its eventual extinction in the "post oxidation" phase [12]. Figure 2.9 shows the time evolution of the in-cylinder absorption, and Figure 2.10 shows the spatial distribution of number concentration at four different times in the cycle [12].

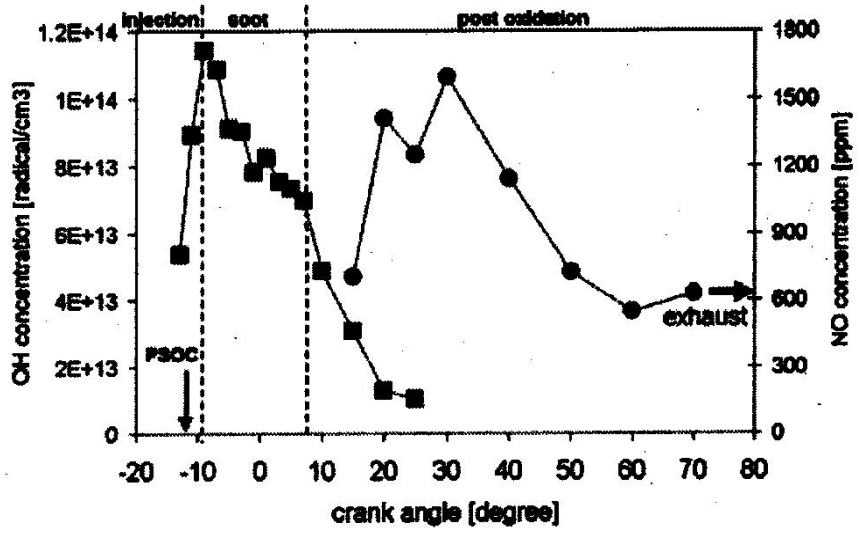

Figure 2-9. Temporal evolution of OH and NO concentrations averaged over the combustion chamber volume. Reprinted from [12].

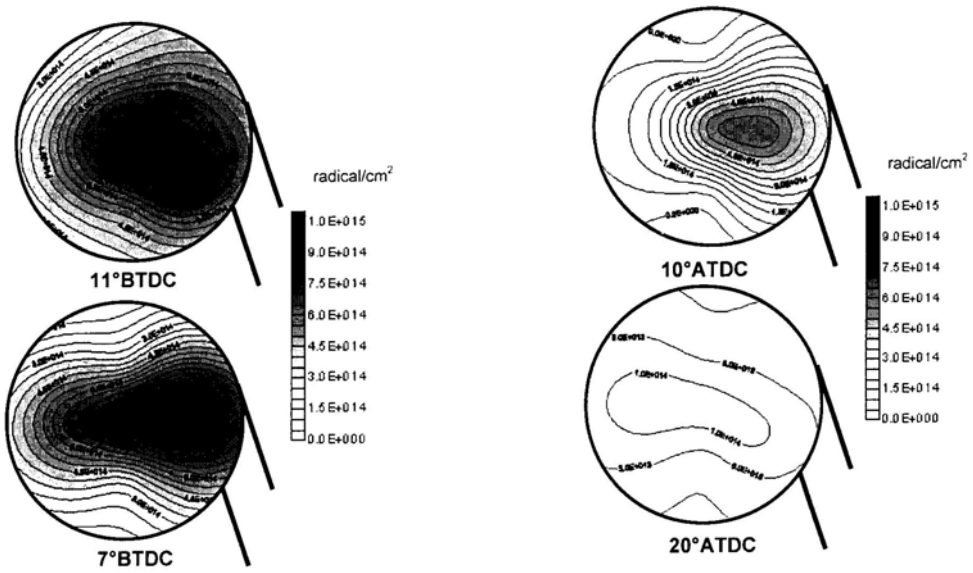

Figure 2-10. Spatial distribution of OH concentration at 11º BTDC, 7º BTDC, 10º ATDC, and 20º ATDC. Reprinted from [12].

Richter *et al.* applied absorption spectroscopy to an HCCI engine in order to show the evolution of the total absorption of the combustion process over the heat release. Their experimental setup was very similar to this work in that they employed a Deuterium light source, collimated through an optically accessible clearance volume. This light was collected into a spectrograph and imaged onto an intensified charge-coupled device (iCCD) camera [13]. Their research employed a variety of fuels, and it was noted that the cool flame, two-stage heat release only happened with the iso-octane/n-heptane fuel mixture. Pure iso-octane had no such cool flame behavior [13]. Figure 2.11 shows a plot of their pressure and heat release curves. The cool flame can be seen around 20º BTDC and corresponds to the first pressure rise.

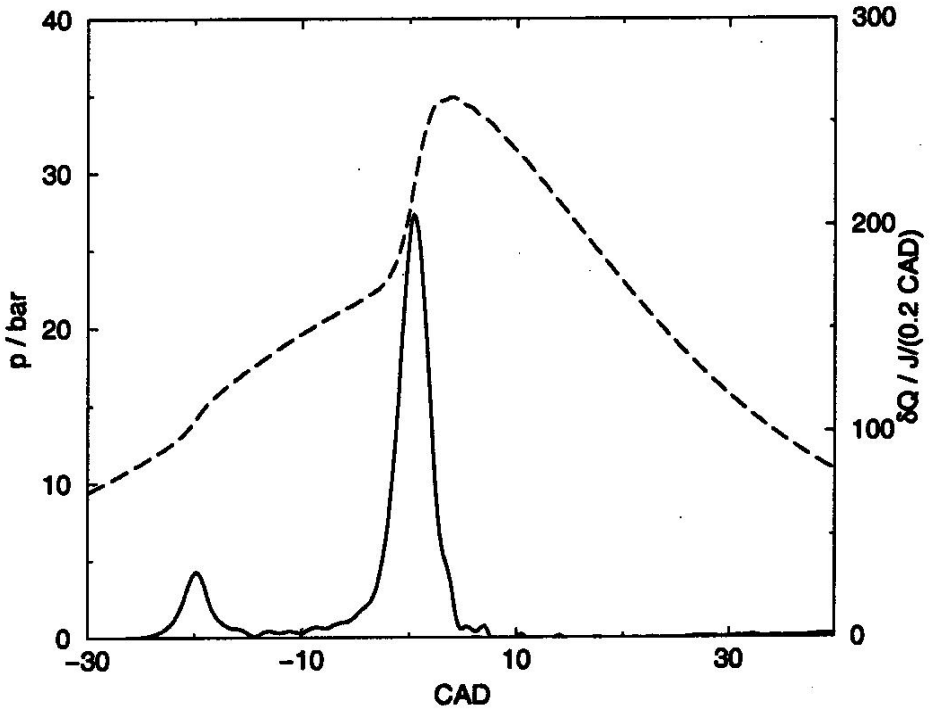

Figure 2-11. Pressure trace and calculated heat release with an iso-octane/n-heptane fuel mixture. Reprinted from [13].

To collect a strong enough signal, the authors used an exposure time of 300μs, which corresponded to 1.8 crank angle degrees (CAD) at 1000 rpm. The authors note that this relatively long exposure time causes some smearing in the collected data [13].

All fuels tested showed a similar absorption cross-section, except for the iso-octane/n-heptane mixture. This mixture showed a particularly strong absorption in the ultraviolet (UV) range, a reflection of the cool flames unique to the n-heptane fuel [13]. These results are shown in Figure 2.12.

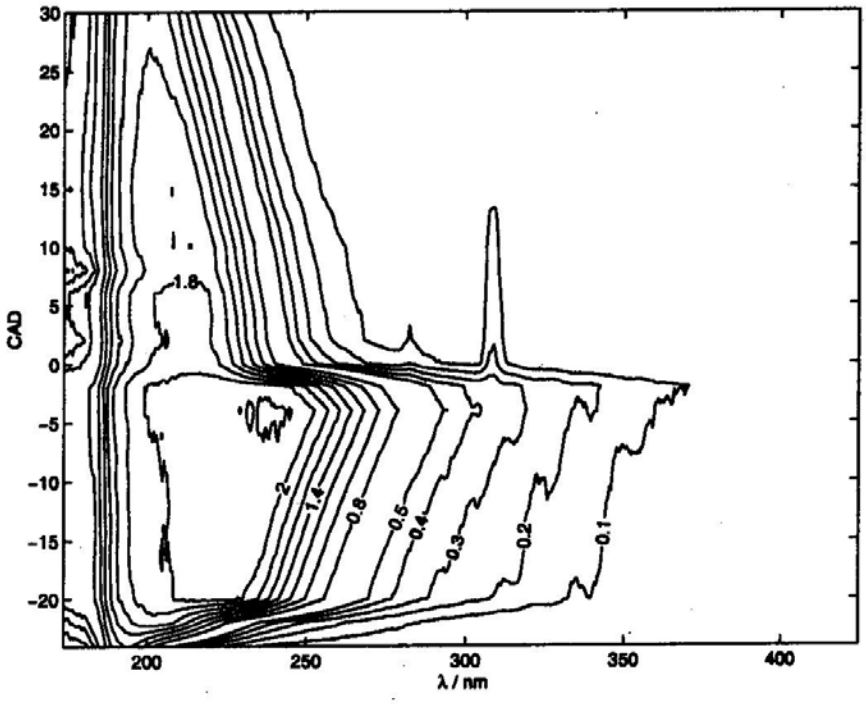

Figure 2-12. Absorption at various crank angle times with an iso-octane/n-heptane fuel mixture. Reprinted from [13].

Detection of OH seems feasible, but the absorption bands specific to OH at 310 and 284 nm were not resolvable before TDC. Richter *et al.* note that the choice of light source is extremely important to the work because the absorption characteristics of various fuels are so different [13].

2.4. Temperature measurement

2.4.1. Problem

A piece of information that is essential to the absorption spectroscopy measurement—mostly for the prediction of spectra—is the accurate knowledge of temperature and pressure of the gas mixture. Since cylinder pressure determines force on the piston and thus torque and power outputs, it is of prime interest to the engine

researcher. Thus, suitable methods of obtaining pressure information are readily available. Temperature is often a much harder variable to measure. While the pressure is uniform across the volume of the cylinder and can be measured anywhere, the temperature is not uniform. Intrusive measurements of temperature are difficult to manage with the high peak temperatures that occur in engines, and methods such as sampling valves are relatively slow and can change the value of the temperature variable itself as well as the chemical composition of the sampled gas [12]. Estimation of temperature through calculation such as the ideal gas law or an isentropic compression/adiabatic flame process can lead to considerable error.

Temperature is especially important to this experiment in order to compare results against those calculated by numerical models. The low-load limit established by Dec and Sjöberg was established on a temperature basis [7].

2.4.2. Some solutions for non-intrusive bulk temperature measurement

Noguchi et.al used an Indium-Antimony detector to measure intensity of infrared radiation from CO2 gases in the cylinder. This technique was valid for temperatures less than 1000 degrees Celsius. For temperatures above 1000 degrees Celsius, the researchers detected light emission from Li and Na seeded into the fuel at concentrations of 0.3 g/L-fuel and 0.04 g/L-fuel, respectively. The second technique proved to be the most accurate according to their error analysis, and the seeding was found not to affect the combustion in a significant way [4].

Corcione *et al.* calculated temperature numerically using a modified version of the KIVA-3, a fluid mechanics code developed at Los Alamos National Laboratories. They

input a measured pressure trace into the numerical simulation, which output the cylinder temperature as a function of crank angle [12].

2.4.3. Wavelength-Agile Laser Sensor Measurement

Wavelength-agile sensing, an emerging method of temperature measurement, is the one chosen for these experiments. Wavelength-agility refers to the capability of a laser system to quickly change its output wavelength to the point that the wavelength sweep time is much less than the experimental unit of time—in this case, engine speed or crank angle time [14, 15].

These lasers allow broad absorption measurements to be taken continuously, and most systems have a time response that can achieve crank angle time resolution. In addition, these systems are less affected by issues such as beam steering and window fouling which often plague optical combustion measurements [15]. The drawback to a wavelength-agile measurement is that its data is a line-of-sight average and the results may be skewed if the target is highly stratified or in a heterogeneous mixture. This is a less significant problem in an HCCI engine measurement. Because of the homogeneity, the line-average is more representative of the entire mixture [14, 15].

Using this technique to measure temperature involves comparison of an absorbed spectrum, water in this case, to an appropriate simulated spectrum in a database created using HITEMP. As pressure is known in the experiment, that spectrum is compared to spectra in the database with a similar pressure, but different temperatures. The spectrum most similar to the experimental spectrum is assumed to be the one with the correct temperature for the conditions.

Obstacles to this technique do exist and can be significant. These include etalon noise, and non-zero background absorption. The noise is resolved by convolving the target spectrum with a relatively broad Gaussian curve. This precludes measurement of pressure from the absorption, but pressure can be reliably measured in other ways. Baseline absorption from other species and beam steering is minimized by differentiating the absorption curve with respect to wavelength since differentiation emphasizes the desired features over the slowly changing background. Finally, a least squares fit is employed to find the best fit between the database and the experimental data. The temperature in the database with the smallest least-square sum is then chosen as the measured temperature [14, 15].

3. Experimental Setup

This chapter will attempt to summarize the specifications of the equipment used for all phases of experimentation so that results are easily repeatable by other researchers.

3.1. Engine and Mechanical Systems

3.1.1. Engine

The engine used for these experiments was a single-cylinder GM Research "Triptane Base 4" block design with an overhead valve setup. The head design includes two spark plug receptacles. One space was occupied by the pressure transducer, and a "blank" was installed in the other as spark plugs are unnecessary for HCCI operation. A spacer ring was installed between the head and the block and its design allowed direct optical access to the combustion chamber. The piston was a Bowditch design, which allowed optical access through top of the piston crown. Such access was not required for these experiments and the piston will not be discussed further. The combustion chamber was a "double-pancake" shape as the piston crown was recessed into the piston cap.

Compression ratio could be changed by choice of several different piston crowns, their height determining the size of the recess into the cap. The maximum compression ratio possible was approximately 15:1. These experiments used a 9.64:1 compression ratio, calculated from Equation 3.1 based on displacement and clearance volumes [6].

$$r_c = \frac{V_d + V_c}{V_c} \tag{3.1}$$

Engine specifications are listed in Table 3-1.

Displacement	511 cm^3
Clearance Volume	59.1 cm^3
Compression Ratio	9.64:1
Bore	92.4 mm
Stroke	76.2 mm
Con. Rod Length	144.8 mm
Intake Valve Dia.	26.5 mm
Exhaust Valve Dia.	26.5 mm
IVO/IVC	349/-180
EVO/EVC	115/365

Table 3-1. Engine Specifications and Geometry

3.1.2. Fluid systems

3.1.2.1. Coolant

The block and head of the engine were liquid cooled in a closed loop, using external hoses to connect block, head, and reservoir. A 50/50 water-antifreeze solution was used to protect against corrosion. An electric heating element is placed in the coolant loop, and was operated continuously. In order to achieve control of the temperature around a set point, a solenoid valve is used, which when opened exposes the hot coolant to a counter-flow of cold building water in a cross-flow heat exchanger. Previous experiments on this engine have shown 68º C to be the optimum coolant temperature [17].

3.1.2.2. Lubrication

An external pump provided oil pressure and flow at the bearing surfaces of the engine. Oil blow-by from the crankcase, past the oil control ring, to the cylinder can significantly foul the optics involved in these experiments. To help prevent optical window fouling, a vacuum pump was fitted to the crankcase.

3.1.3. Dynamometer

Power to motor the Triptane engine came from a General Electric 440 VAC three-phase dynamometer connected after the flywheel. Dyno control was performed by a Reliance Electric Max Pak Plus VS Drive Box. The system could handle motoring or generating up to 30 kW at up to 1500 RPM. Dyno speed was controlled by use of a coarse and fine potentiometer adjustment on the drive box. These controls set the voltage that drives the dyno. Since the input is a voltage, speed control could also be accomplished by use of a computer. That method was not used in these experiments since engine speed remained constant during all tests, and an accurate and repeatable control of a change in engine speed was not required.

3.2. Air and Fuel Handling

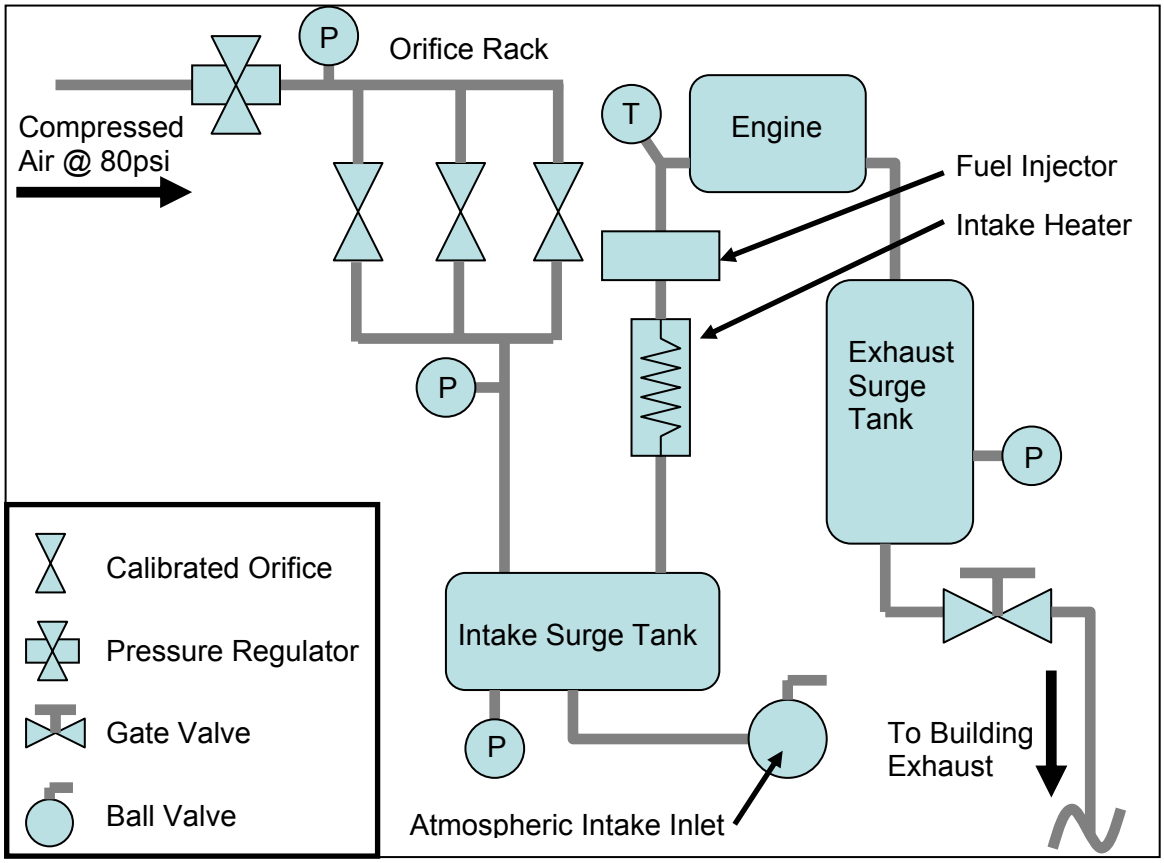

Figure 3-1. Air Flow Schematic.

3.2.1. Fresh Air Intake

To meter the fresh intake charge to the engine, compressed air was regulated to control the upstream pressure for one of three calibrated orifices of different sizes. The orifices were operated at choked conditions so that the mass flow through them is linear with upstream pressure. This pressure was monitored at gauge with a Heise pressure gauge with an accuracy of 0.69 kPa, and this was used as a set point for mass flow according to the various orifice calibrations. Calibration data are included in Appendix A. The intake surge tank was downstream of the orifices and was used as a mechanical capacitor so that the engine encountered a constant intake pressure at steady state

conditions. Surge tank pressure was monitored by a Wallace & Tiernan absolute pressure gauge accurate to 0.69 kPa, which was also could be routed to measure exhaust and atmospheric pressure.

3.2.2. Charge heating

In order to achieve HCCI combustion at a relatively low compression ratio, some form of intake heating is required. In these experiments, the intake air was directly heated with no EGR. An electrically powered in-line heater was installed directly downstream of the intake surge tank. Closed-loop control of the heater was accomplished by use of a Love Controls 1600-series temperature/process controller. The controller took temperature data from a thermocouple placed immediately upstream of the intake valve. In this way, the cylinder intake temperature was accurately controlled within 1º C even though the heater could not be placed immediately upstream of the intake valve.

3.2.3. Seeding and Diluent Addition

The setup used was capable of seeding the intake charge with a liquid such as water, or adding a gaseous diluent. Liquid seeding was not used in this research and will not be further discussed. Gaseous diluents were introduced directly into the intake surge tank from their respective reservoirs through a quarter-inch line. This input was upstream of the heater. Diluent level was estimated by the reduction in air mass flow in order to achieve an atmospheric intake surge tank pressure. It was also measured directly using the emissions analysis. These two values agreed quite well, and are discussed in further detail in Chapter 5.

3.2.4. Fuel Delivery

These experiments used Orbital air-assisted fuel injector installed just downstream of the charge heater. This setup is used in the Mercury Marine Optimax 2-stroke outboard engine line as a gasoline direct injection (GDI) system. Good air/fuel mixing at injection time is a requirement in this application since GDI arrangements are not allowed much time to homogenize after injection and before ignition. The air-assist injector consists of a standard fuel injector, which injects first into an air injector. The air injector acts as a mixing chamber and its own injection further atomizes the fuel. For these experiments, the injector rail was installed about 1m upstream of the intake valve so that additional charge homogeneity could be achieved through mixing time. Fuel homogeneity from this system has been verified through in-cylinder measurement by other researchers [16, 17].

Air pressure for the air injector was regulated to 550 kPa. Fuel was contained in a liquid accumulator and its pressure was maintained by nitrogen at 620 kPa. Fuel-air differential pressure has the largest effect on mass of fuel injected, so this differential was maintained at 70 kPa through use of a separate differential regulator. Figure 3.2 shows a schematic of the fuel delivery system and points out several important features.

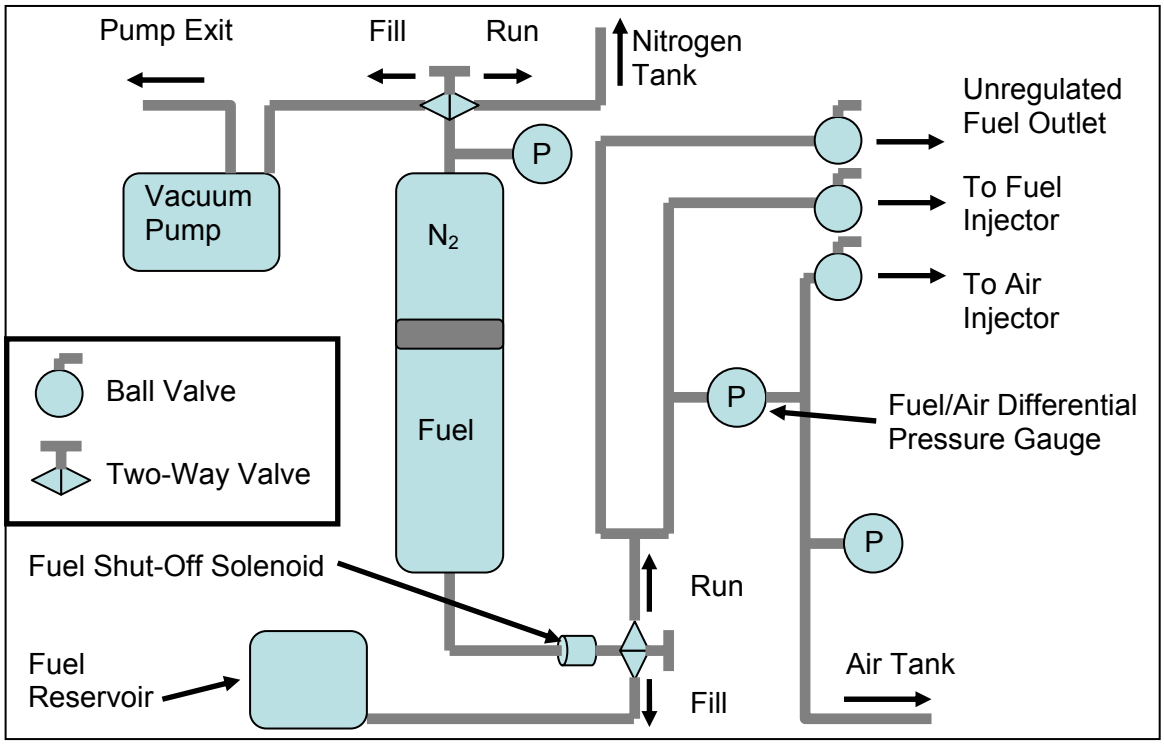

Figure 3-2. Fuel system schematic.

Refilling of the fuel accumulator was accomplished by releasing the fuel pressure at the top two-way valve and applying a negative pressure from a vacuum pump. The unregulated fuel pressure outlet was used mainly for emptying the fuel tank in order to switch fuels for other experiments on the same engine.

The fuel used was a >99% pure n-Heptane solution obtained from Aldrich Chemical, catalog number 15,487-3. Its characteristics are listed in Table 3.2.

Fuel Type:	n-Heptane
Chemical Formula	C_7H_{16}
Chemical Structure	$CH_3(CH_2)_5CH_3$
Octane Number	0
Molecular Weight	100.2 [kg/kmol]
Lower Heating Value	44.93 [MJ/kg]
Specific Heat	2.24[a] 1.61[b] [kJ/kg-K]
Min. Ignition Energy	14.5 [mJ]
Auto-Ignition Temp	204 [ºC]

[a]liquid at 25º C [b]vapor at 25º C

Table 3-2. Fuel Characteristics.

3.2.5. Exhaust

Exhaust gases were expelled from the engine to the exhaust runner. A percentage of the gas was sampled to the emissions bench. The remainder entered an exhaust surge tank whose pressure could be measured separately. The exhaust surge tanks exited to the building exhaust system which runs at a slight vacuum of approximately 96 kPa. Exhaust pressure was not controlled in these experiments, but some control could be achieved by partially closing the gate valve downstream of the exhaust surge tank. In this way, pressure could be raised to a more realistic value if necessary.

3.3. Controls and Data Acquisition

3.3.1. Electronic controls

Base engine control was performed by the MotoTune software package from MotoTron, Inc. This software made parameters such as spark timing and fuel injection programmable by the user through the engine control unit (ECU). The primary

advantage of this software is its support for the Orbital air-assist fuel injection system, including injection calibration inputs. The MotoTune system can output up to six spark TTL signals which can be used to trigger external systems. In this experiment, the camera was triggered by such a spark signal.

Pressure data were acquired by use of a water-cooled AVL QC42D-E piezoelectric pressure transducer and a Kistler 5010A12 charge amplifier. Voltage from the charge amplifier was passed to a Hi-Techniques data acquisition system running an acquisition program called REVelation. Piezoelectric pressure transducers have a tendency to drift, but are very good at measuring relative changes in pressure, so for each cycle the recorded pressure was pegged by the software to a value of one atmosphere at -180 CAD. Pressure data were taken in sets of 100 cycles and averaged by the software.

More information about the engine control and pressure monitoring systems can be found in previous theses whose data was taken on this engine [17-19].

3.3.2. Exhaust Emissions Analysis

A five-gas emissions analyzer from Horiba Instruments, Inc. was used to measure steady-state emissions of CO, CO_2, O_2, uHC, and NO_x. Gas samples were routed to the emissions bench from the exhaust tank through an electrically heated line, controlled at 170º C. The heated line was used to prevent hydrocarbon and water condensation. A vacuum pump integrated into the bench ensured an adequate flow rate.

As the exhaust stream reached the emissions bench, it passed through a chilled bath maintained at 0º C in order to condense the water in the exhaust directly before gas analysis to prevent damage to the analyzers. Volumetric concentration of CO and CO_2 are measured by Nondispersive Infrared analyzers. Oxygen concentration is measured by

a Magnetopneumatic analyzer. A Flame Ionization Detector measures the uHC emissions, and a Chemiluminescent Analyzer measures the NO concentration.

Outputs of all analyzers were passed to signal amplifiers at which a voltage could be read corresponding to concentration according to each system's calibration curve. CO and CO_2 analyzers required a third-order polynomial curve fit, and were calibrated at 11 points using a Stec SGD-710C gas divider. CO and CO_2 analyzer calibration curve data can be found in Appendix B. The other three analyzers operated linearly, and could be calibrated using a two-point (zero and span) method. Calibration checks were performed on all analyzers each time data were taken.

Outputs from the signal amplifiers were conditioned through an analog-to-digital (A/D) converter and recorded on a PC using a LabView program window. This program could be used to monitor either concentration or raw voltage signal in real time, or averaged over a given time frame.

3.3.3. Spectroscopy

The light source used in these experiments was a Hamamatsu L7893-01 Deuterium lamp. It was chosen for its power in the desired wavelength range and output stability compared to other manufacturers. Light from the lamp was focused into an Ocean Optics model P600-1-SR, 600 μm diameter anti-solarization fiber 1 m in length. Light was collimated to pass through the clearance volume by an Ocean Optics model 74-UV Collimating Lens. Lens specifications are listed in Table 3.4.

Model	Diameter	Focal Length	Material	Wavelength	Operating Temp.	Connector
74-UV	5 mm	10 mm	f/2 fused silica Dynasil	200-2000 nm	70º C	SMA 905, 6.35 mm ferrule, 3/8-24 external thread

Table 3-3. Collimation lens Specifications.

Light was collected on the exit side of the clearance volume and focused into an Ocean Optics model P200-2-UV-VIS, 200 μm fiber 2m in length. This collection fiber was chosen because its diameter was large enough to collect a sufficient percentage of the delivered light, and not so large that it contributed unnecessarily to the spectral broadening of the system. Collection fiber broadening characteristics are discussed in section 4.1.

An Oriel MS260i 1/4m spectrograph was used to separate light according to wavelength and project it onto the camera. The F/# of the spectrograph is 3.9. Input and exit focal lengths are 220 and 259 mm, respectively. These experiments used a 600 lines/mm grating which could be automatically positioned using software. Information on available gratings is listed in Table 3.5. The light path from this instrument is illustrated in Figure 3.3.

Model	Line Density	Blaze Wavelength	Peak Efficiency	Spectral Resolution	Bandpass	Wavelength Region
	[lines/mm]	*[nm]*	*[%]*	*[nm]*	*[nm]*	*[nm]*
74166	600	400	85	0.5	165	250-1300
74172	300	500	80	0.98	325	250-1150

Table 3-4. Grating specifications.

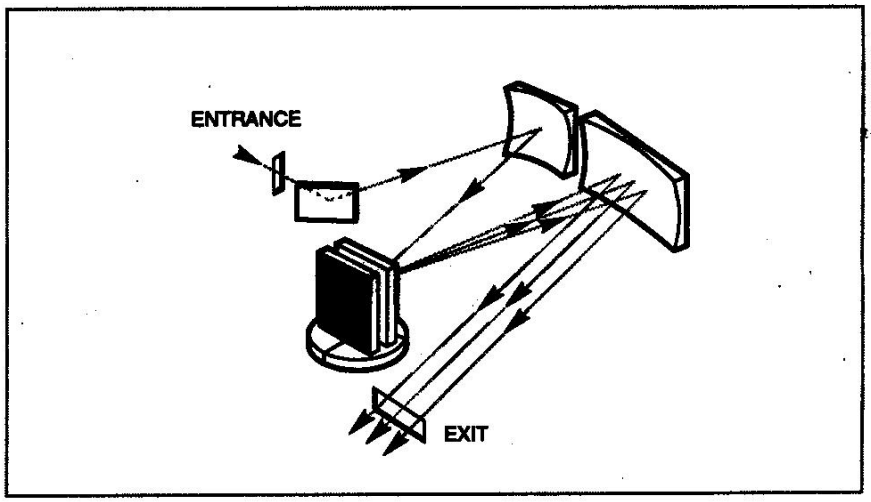

Figure 3-3. Spectrograph light path.

The spectrograph's input slit was replaced by a fiber optic input that incorporated a degree of freedom in the vertical direction. By turning a micrometer, the vertical position of the image of the input fiber could be positioned manually at any point on the camera. This was important to the data acquisition as will be described in section 4.3.1.

The camera used was an Andor Technology back-illuminated, slow scan charge-coupled device (CCD). This type of camera converts incident photons into an electric charge, the magnitude of which is determined by the number of photons received. Its recording surface consists of a 512 x 512 square of pixels or "bins" in which charge can be held. Pixel size is 13 x 13 μm.

Andor MCD data acquisition software controlled the CCD camera and spectrograph. The camera software allows charge on various pixels to be added and shifted in various ways according to the needs of the user, and output to an Andor Tecnology model CCI-010 PCI A/D converter card.

An example light spectrum taken from the lamp through the previously described system is shown in Figure 3.4, and a 200 cycle average of that spectrum is shown in Figure 3.5. The error bars in Figure 3.6 show the variance of mean over the 200 cycles shown in the average case.

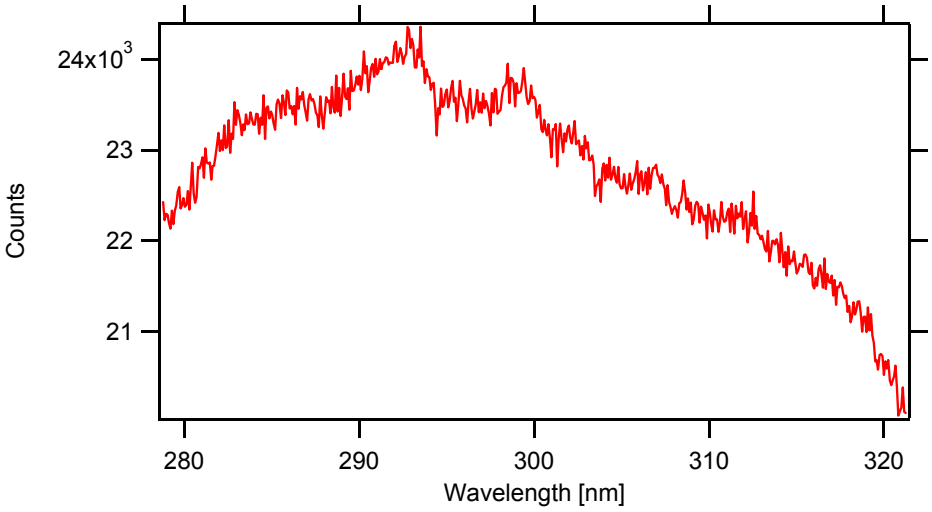

Figure 3-4. Lamp spectrum.

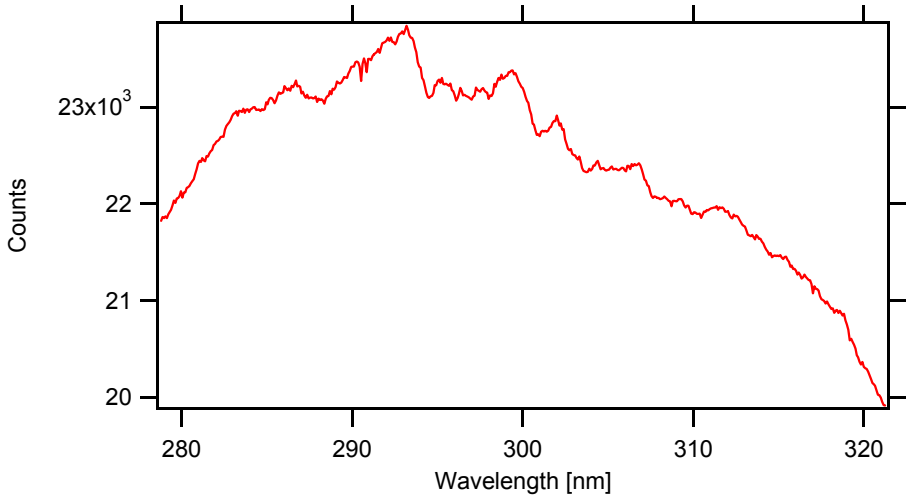

Figure 3-5. Lamp spectrum averaged over 200 cycles.

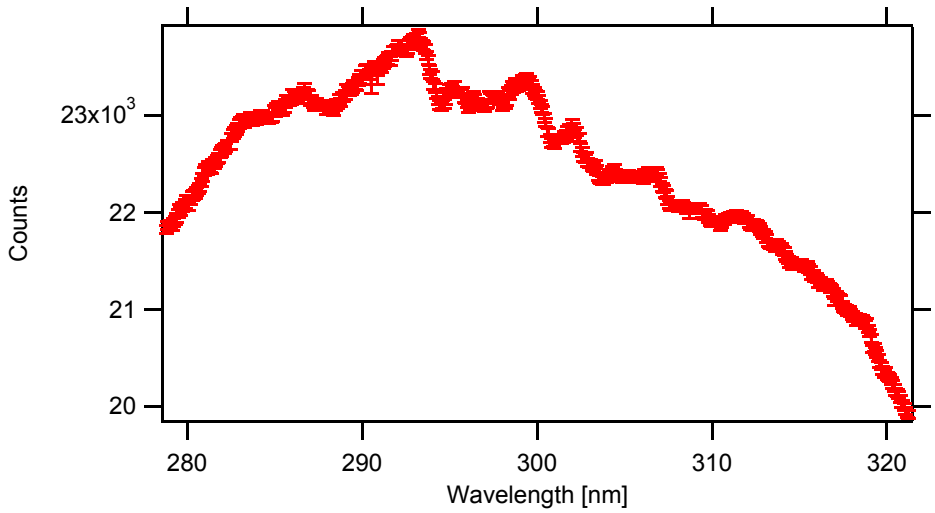

Figure 3-6. Variance of the mean in the lamp spectrum average.

4. Optical system development and analysis

This chapter will include descriptions of some of the measurement techniques used and peculiarities of the systems that are unique to these experiments. The focus will be on optical data, since those data were of the greatest importance in determining the concentration of OH in the cylinder.

4.1. Image pre-processing, and characterization of instrument broadening

Collecting light through a fiber of a finite size and imaging through a spectrograph causes a loss of resolution that tends to broaden and flatten all spectral features measured. Instrument broadening was characterized in this experiment by observing the broadening of an isolated emission line from a Mercury calibration lamp. A Mercury lamp was chosen because they have strong, narrow spectral lines in and around the wavelength region of interest of this research. The line at 312.57 nm was selected for further examination, as it is the strongest in the 270-330 nm range.

Spectra were recorded with three input fibers with core diameters at 50, 200, and 600 μm. The selected peaks were fit to a Gaussian function using IgorPro. Unbroadened, the peaks should be only a few pixels wide, but the Gaussian fit shows how this width changes for each input fiber as a result of the spectral broadening that each contributes to the system. The Full-Width, Half-Maximum (FWHM) of the Gaussian shape is the width of the curve at half of the total height, and is a standard measure of the breadth of the Gaussian.

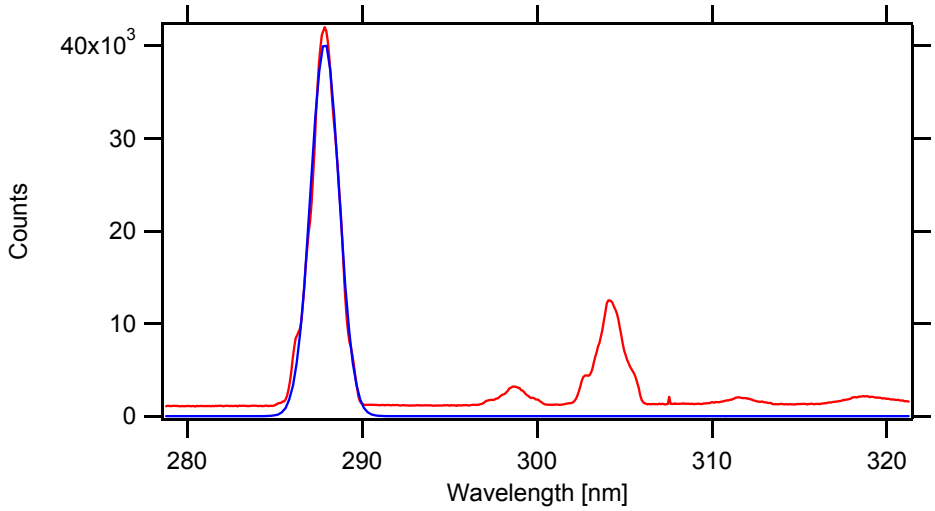

Figure 4-1. Mercury lamp spectrum with a 50 µm input fiber. FWHM measured is 1.1474 nm.

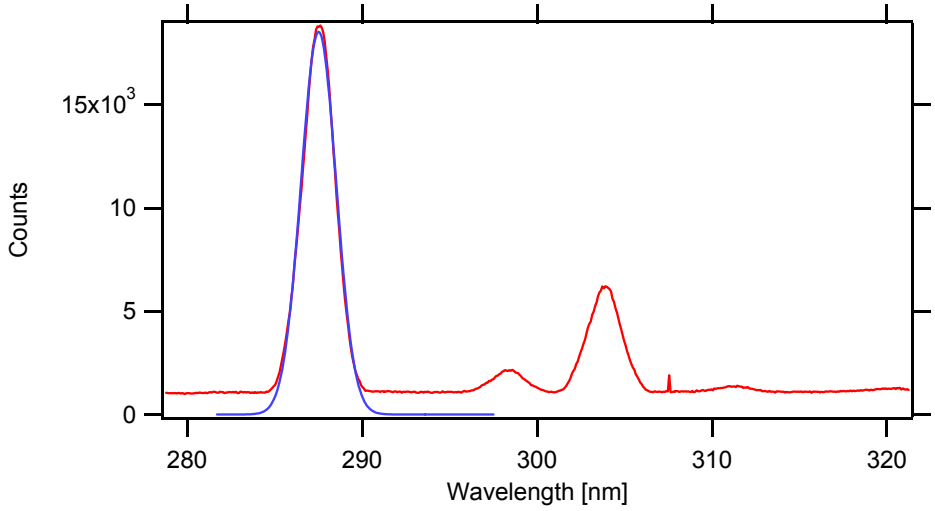

Figure 4-2. Mercury lamp spectrum with a 200 µm input fiber. FWHM measured is 1.4225 nm.

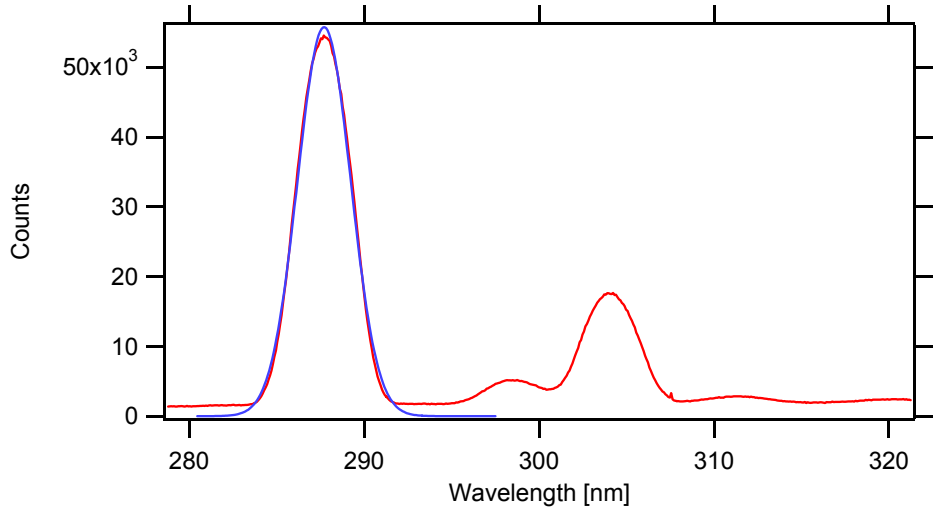

Figure 4-3. Mercury lamp spectrum with a 600 µm input fiber. FWHM measured is 2.1444 nm.

It is clear in Figures 4.1-4.3 that fibers with smaller core diameters contributed less to total instrument broadening. However, as mentioned in Chapter 3, output power was of great concern to these experiments. While the 50 µm fiber showed better resolution than the 200 µm fiber, it could only transmit $1/16^{th}$ the total light that the 200 µm fiber can, since it is proportional to the cross-sectional area of the fiber core. Thus, the 200 µm fiber was used in these experiments as it represented a compromise between signal strength and spectral resolution.

It should be noted that the spectra in Figures 4.1-4.3 are essentially mirrored around the center wavelength axis. The reasoning for this effect will be discussed in section 4.4. Mirroring only changes the position of the 312 line, not its FWHM.

4.2. Spectrum prediction

In order to quantify the concentration of OH, the optical data of these experiments were compared to predicted spectra at the same conditions. Most of the variables in the

Lambert-Beer law are known constants and easily measured variables, such as path length or pressure. But the absorption coefficient is not easily known and must be simulated by programs that calculate these values based on quantum mechanics. To accomplish this, two externally written computer programs were used in conjunction with each other.

4.2.1. LIFBASE Code

The LIFBASE program, written by J. Luque and D.R. Crosley can generate absorption and emission spectra for rotational and vibrational lines in any wavelength range for OH and other molecules [20]. This program is very versatile, but its absorption coefficient calculation was limited because the results were always normalized to a value of 100. This made it difficult to track changes in coefficient magnitude at particular wavelengths from one case to another. The algorithm by which the program made this normalization could not be determined, and LIFBASE alone could not yield the absorption coefficient data required. A sample LIFBASE output for conditions of 1500K and 20 atm is shown in Figure 4.4.

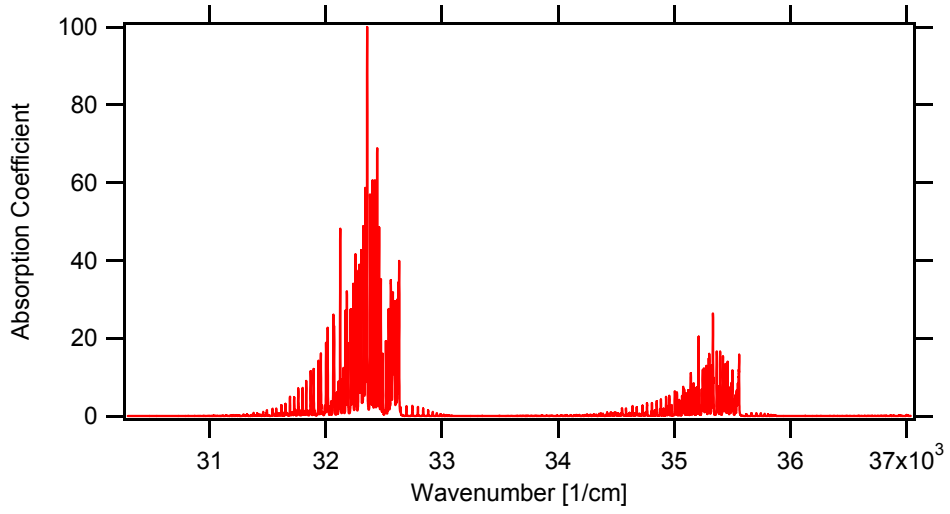

Figure 4-4. LIFBASE output. 1500K, 20 atm.

4.2.2. Davidson-Herbon Code

The second program was a FORTRAN code originally written by D.F. Davidson *et al.* to generate spectra for the OH bandhead [21]. This program was then modified by J.T. Herbon to include more rotational lines, and modifications to the rotational and vibrational energy expressions used by the code [22]. This program takes as inputs temperature and pressure and outputs a string of absorption coefficients versus wavelength (in cm^{-1}). A sample Herbon output at 1500K and 20atm is shown in Figure 4.5.

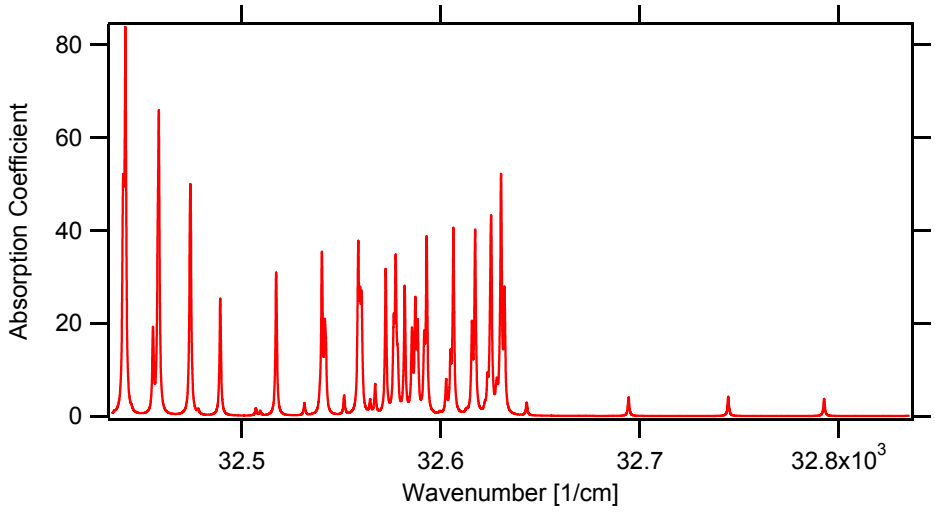

Figure 4-5. Herbon output. 1500K, 20 atm.

This program—hereafter referred to as "Herbon"—was useful because of its accurate prediction of absorption coefficient magnitude, but it had a very limited wavelength range. Absorption coefficients were only calculated from 32435 to 32835 cm^{-1} (304-308 nm). As such, this program could quantify the magnitude for absorption coefficients, but only for a small part of the wavelength spectra this work was interested in.

4.2.3. Spectral synthesis

The solution proposed was to make these two programs work together. For each relevant temperature and pressure, an output was made from each of the previous two programs. The Herbon code was run at its narrow wavelength range (304-308 nm), and LIFBASE was run at the full wavelength range of interest (270-330 nm) in wavenumber units so as to match Herbon. The instrument broadening factor in LIFBASE was set at a very low value, 1 cm^{-1}.

A third program, which will be referred to as "Peg-and-Convolve" written in the C environment, takes as inputs the outputs of the Herbon and LIFBASE programs. Peg-and-Convolve then chooses the wavelength range within the LIFBASE output that matches the Herbon range. The LIFBASE output magnitude is then pegged to the magnitude of the Herbon output. This eliminates the automatic normalization that the LIFBASE output is subject to.

Peg-and-convolve then converts the wavelength axis of the pegged LIFBASE output from wavenumber (cm^{-1}) to nm. Finally, a convolution integral is performed, which convolves the conditioned LIFBASE output with a Gaussian of the same FWHM as that measured for the system's spectral response, described in section 4.1. The program outputs a broadened spectrum that approximates the absorption actually seen through the real optical apparatus. A sample of a convolved output spectrum is shown in Figure 4.6, corresponding again to 1500K and 20 atm. The original LIFBASE spectrum is also shown to illustrate the change in coefficient magnitude and the consistency in the convolved shape.

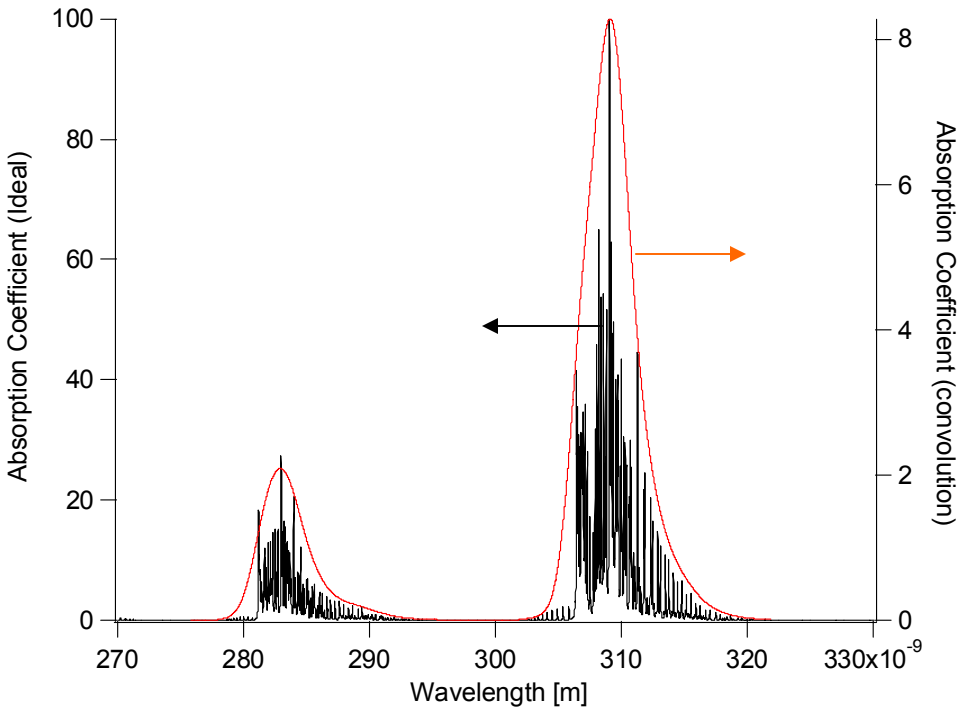

Figure 4-6. Convolved spectrum prediction.

The program was set up such that it could convert multiple sets of files at once for ease of use. The code for the Peg-and-Convolve program can be found in Appendix C.

4.3. Fast kinetics acquisition

4.3.1. Software

One of the goals of this experiment was to measure the concentration of OH within one cycle. This requires time resolution on the order of one crank angle degree (CAD). Even at a low engine speed such as 600 RPM, the passing of one crank angle corresponds to approximately 0.278 msec. This is an extremely short time and the difficulty in recording a series of spectral data with a camera is that a physical shutter cannot be made to move this fast.

The Andor MCD program includes a "Fast Kinetics" data acquisition mode, which is designed to take one or more row-images on the microsecond scale. In Fast Kinetics mode, the spectrum to be recorded is projected only at the very top of the CCD surface. The area where this image appears is referred to as the "sub-area". The unilluminated area is used to "store" spectra until they can be read out. Once a row image accumulated, the charge on the sub-area is shifted down by the sub-area height, and a new image can be taken [23]. This process of imaging on a sub-area and shifting is illustrated in Figure 4.7.

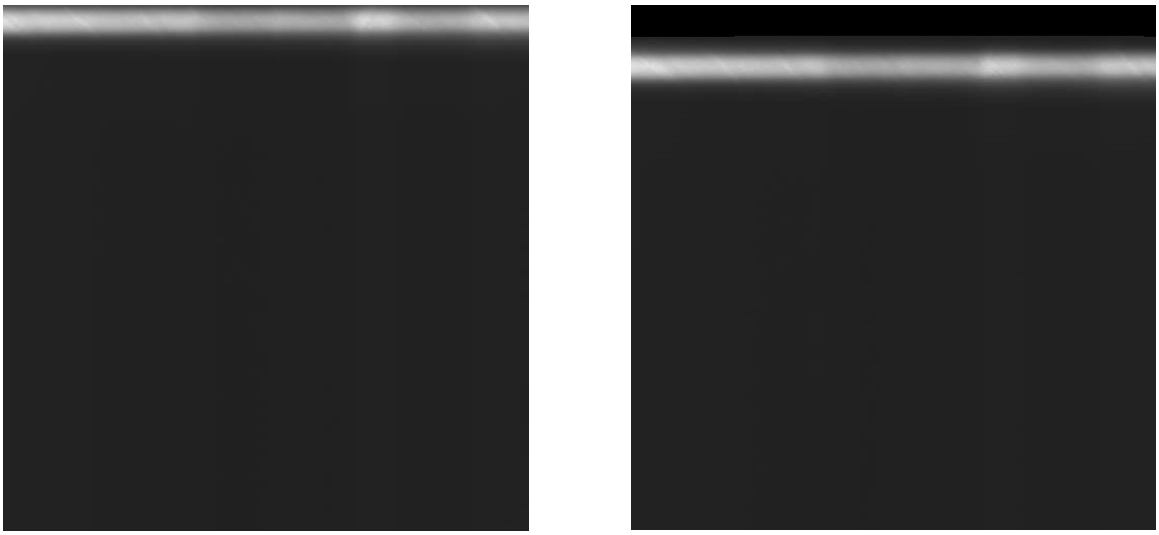

Figure 4-7. Fast kinetics acquisition process. An image is taken at the very top of the CCD, and its charge is then shifted down. This leaves the original sub area clear to acquire a new image.

By repeating the imaging and shifting processes several times until the CCD is full, the result is a picture that can be interpreted as wavelength versus time. It should be noted that sub-area charge shifting time is much less than A/D readout time, allowing pictures to be taken very rapidly. The micrometer-adjustable inlet slit on the spectrograph mentioned in Chapter 3 was used specifically to position the image at the desired place on the CCD [23].

As signal-to-noise ratio (SNR) is always a consideration in quantitative measurement, averaged data was favored over single-shot data. To collect average data, an acquisition program, written by Augusta in Andor's native BASIC programming environment was used [24]. This program takes as input a number of cycles that the user wishes to average over, and is designed to work with the native auto-save mode, which automatically saves all files generated in a specified folder with similar filenames and a numerical increment. The program then runs the camera in fast kinetics mode at the same point in the cycle for the number of times specified.

The program was triggered to start externally by a spark signal from the ECU. Since the spark signal can be set at any crank angle using the MotoTune ECU software, the camera can be made to record at any point in the cycle. The program was designed such that if the next combustion cycle starts before the camera is finished dumping its full CCD data to the A/D card it will wait until the camera is ready and then record at the next available cycle [24]. An outside program can then be run to collect all data and output an average count for all images in the series.

4.3.2. Fast Kinetics settings

As the "storage" space is finite according to the size of the CCD array, and the image quality depends on the number of incident photons, compromises must be made in order to maximize efficiency and data quality. Obviously, choosing a larger sub-area size—a larger percentage of the CCD—will mean that fewer images can be taken. Therefore, these parameters must be carefully chosen.

The fiber was 200 μm in size, corresponding to approximately 15.3 pixels in height. The spectrograph has an internal vertical magnification of 1.6, increasing this

height to 24.6 pixels. Broadening as illustrated in Figure 4.1-4.3 causes the height to increase further and the image to blur in the vertical direction. A sub-area height of 25 pixels chosen for this setup as it was found to include the part of the curve inside the FWHM of the vertical Gaussian shape.

Figure 4-8. Spectrograph image.

Charge from the 25 sub-area rows was added, or "binned," vertically so that each set of 25 rows could be viewed as one piece of data, and so that image intensity could be further increased by taking the entire fiber image at a given wavelength as one input.

The exposure time used was 400 μs. This time is long compared to other literature [13], but output intensity was a greater concern than time resolution loss due to blurring effects.

Time resolution can be inferred from the vertical shift speed of 4 μs. Vertical shift speed is the speed at which the charge is moved, as a row, across the CCD chip. Raising this speed may cause part of the charge to be "left behind" on the chip [23]. The time it takes the shifting process to complete can be expressed as follows:

$$ShiftTime = ExposureTime + \left(VerticalShiftSpeed * SubAreaHeight\right) \quad (4.1)$$

Likewise, the total time for the acquisition of 15 pictures is:

$$TotalTime = ShiftTime * NumberOfExposures \quad (4.2)$$

With the parameters selected for these experiments, *ShiftTime* is 500 μs, which corresponds to 1.8 CAD at 600 RPM. This is the absolute time resolution for the optical data presented in this thesis. *TotalTime* is 7.5 ms, and subtracting the final shift scheme time from *TotalTime* gives 7.4 ms, the time span over which the 15 pictures are taken. This corresponds to a 26.64 CAD sweep for optical data.

A/D readout time selected was 16 μs. This was chosen because it was the highest readout time with the available A/D card. Longer readout times are desirable because they can cause noise in the data to be reduced. A detailed procedure for acquiring and processing data using the Fast Kinetics auto save program is given in Appendix D.

4.4. System peculiarities and characterization

4.4.1. Optical aberration in the spectrograph

During testing, it was noted that the images projected at the top of the camera all looked somewhat similar. Whereas changing the center wavelength projected to the camera should shift the features according to the lamp's spectral characteristics, it did not in the case of the spectrograph-camera setup used previously. This effect is illustrated in Figure 4.9. Figure 4.9 (a) shows the observed image at experimental conditions (centered at 300 nm). Figures 4.9 (b) and (c) attempt to make the features in figure 4.7 (a) move according to the wavelength shifts applied to them (-15 and +15, respectively). The original center wavelength of 300 nm is marked on each picture. It is clear that the features in the three images do not move at all.

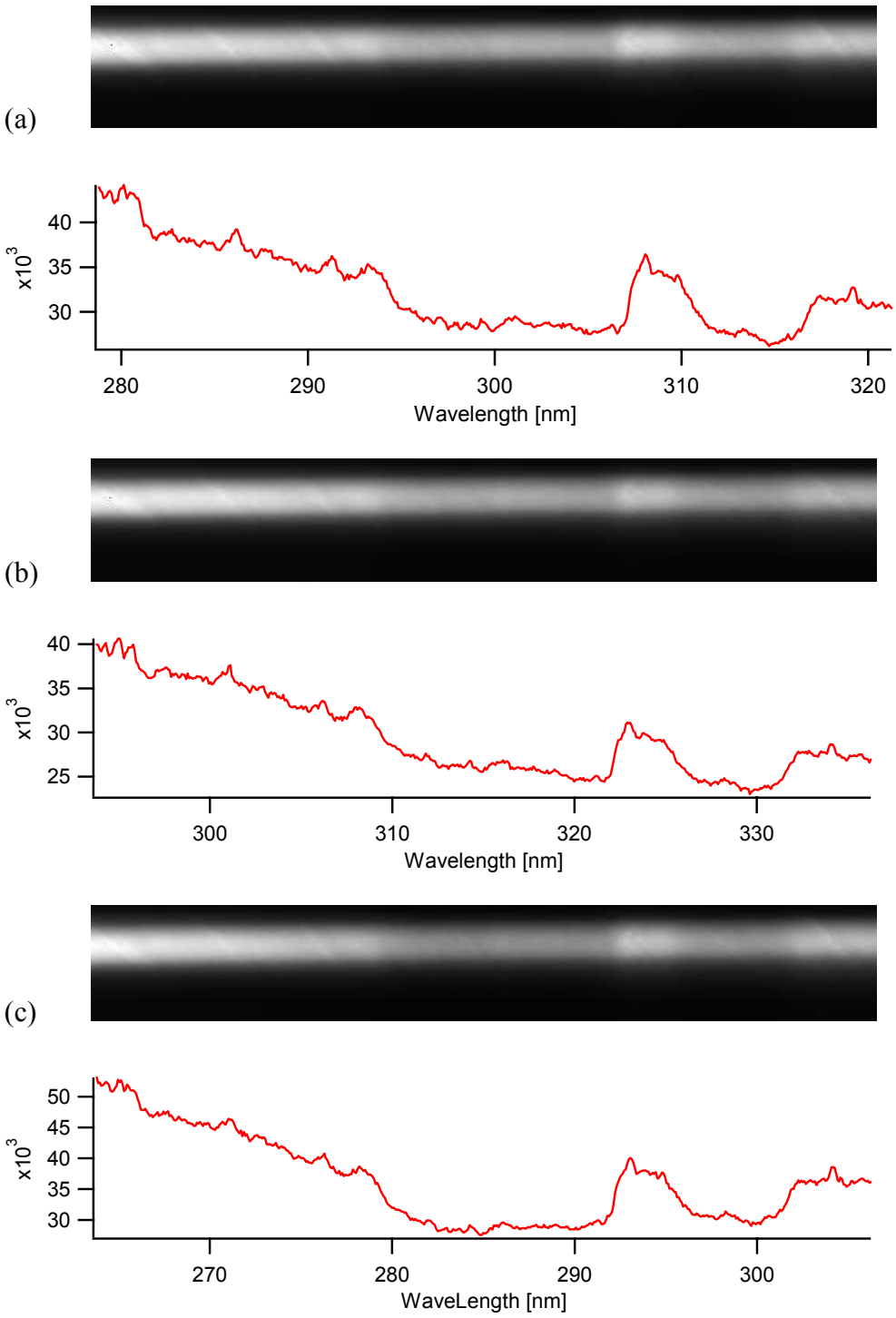

Figure 4-9. Comparison of spectrograph images at various center wavelengths: (a) centered at 300 nm, (b) centered at 315 nm, (c) centered at 285 nm. The spectral shape of these images does not shift when the wavelength shifts.

This behavior was finally attributed to picking up extraneous light or aberrations in the spectrograph mirrors due to the input slit being pushed to the extreme top of the CCD. The solution proposed was to turn the camera upside down with respect to the spectrograph. The switch made no difference to the camera, but it forced the Fast Kinetics image to be placed at the "bottom" of the CCD surface rather than the top. The advantage gained was that the input slit and the resultant image were positioned at a different place on the spectrograph mirrors, and the optical aberration was bypassed. Figure 4.10 shows a comparison of an image from the same light source at the same wavelength range, one projected at the top of the camera, and one at the bottom. The difference in clarity and intensity is clear. Figure 4.11 shows that the spectral shape seen in Figure 4.9 is indeed an artifact of the spectrograph system. The second spectrum in Figure 4.12 looks similar to the unaveraged lamp spectrum in Figure 3.4.

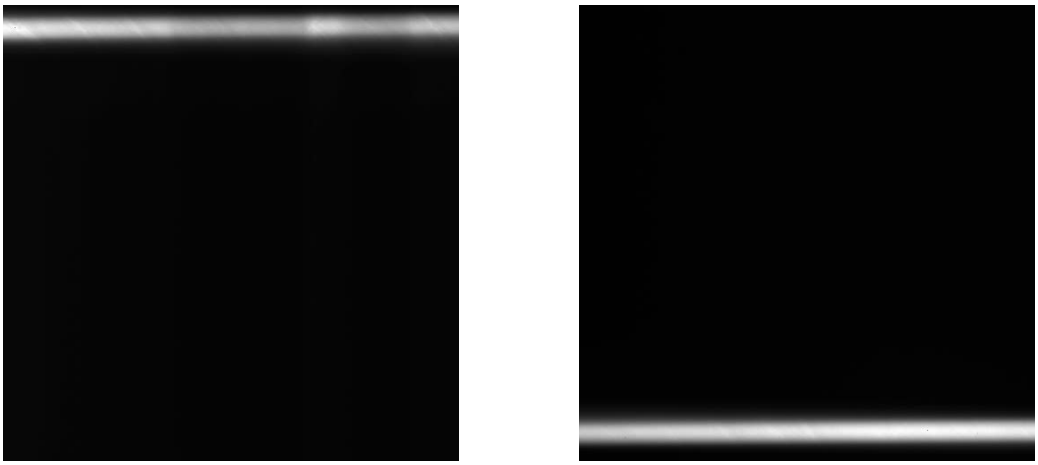

Figure 4-10. Comparison of input fiber location.

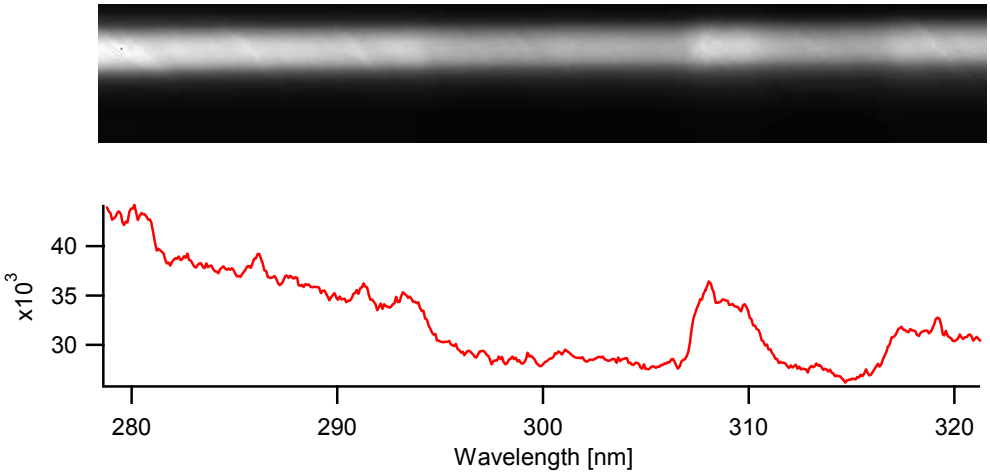

Figure 4-11. Lamp spectrum with fiber to top of camera.

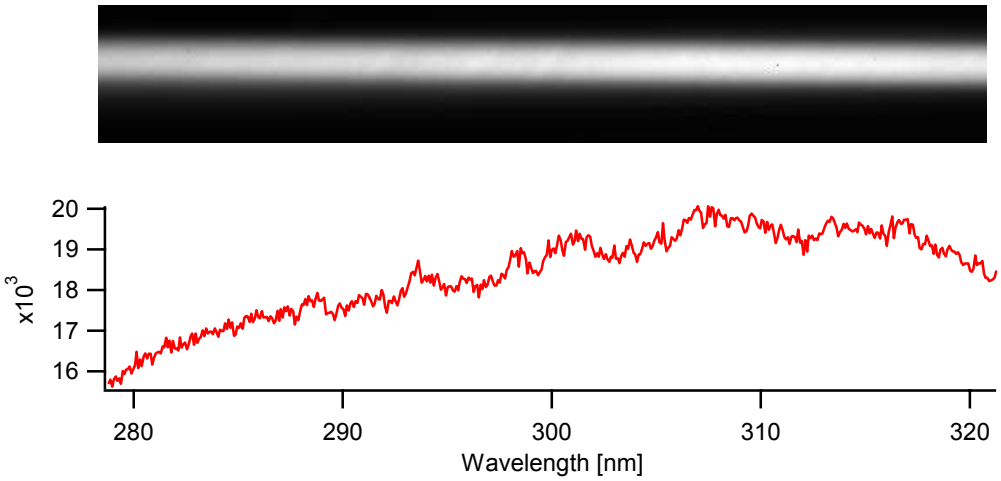

Figure 4-12. Lamp spectrum with fiber to bottom of camera.

The negative side effect of turning the camera over was that the left and right sides of the camera were reversed. So the wavelength axis on the observed picture was actually mirrored about the center wavelength set by the spectrograph. Since the data must be passed to another program to perform averaging, this problem was easy to fix. The output section of the data averaging code switches the data about the center

wavelength axis by writing the wavelength column in the forward direction, and writing the data columns backward. The averaging code is included in Appendix E.

Any wavelength shift due to the center axis of the camera not remaining at exactly the same spot when turned over was easy to account for since a wavelength shift must be included at some point to match wavelengths with those from the Mercury calibration lamp. In this case, the shift was included in the compiler program described in section 4.5.

4.4.2. Image post-processing

When comparing incident spectra to transmitted spectra, a general change in the shape of the curves was noted. If OH was the only molecule absorbing, the parts of the transmitted spectra outside of where absorption was predicted (e.g. see Figure 4.4) should remain the same shape as those of the incident (lamp) spectra. According to the Lambert-Beer law, a transmission spectra is the most general comparison of incident to transmitted spectra:

$$Transmission = 1 - Absorption = \frac{I}{I_0} \tag{4.3}$$

In these experiments, the motored data are considered the incident spectrum, I_0, and the fired data are the transmitted spectrum, I. Figure 4.13 shows the locations of predicted absorption, and Figure 4.14 a sample transmission spectrum. Here in Figure 4.14, a background slope can be seen even in places where OH does not absorb (areas close to zero in Figure 4.13). This indicates that the overall shape of the motored trace is not the same as that of the fired trace—if it was, a ratio of output to input such as the transmission spectra would have no slope in these areas.

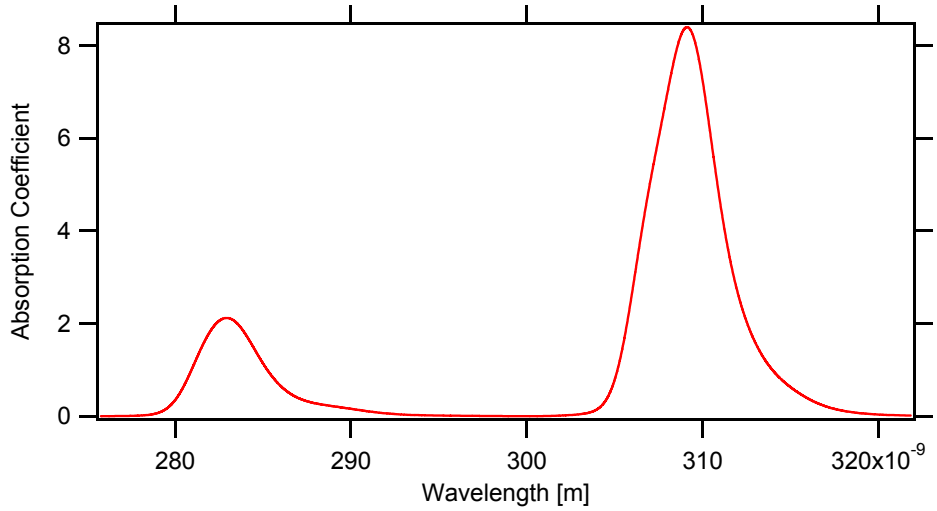

Figure 4-13. Predicted absorption spectra.

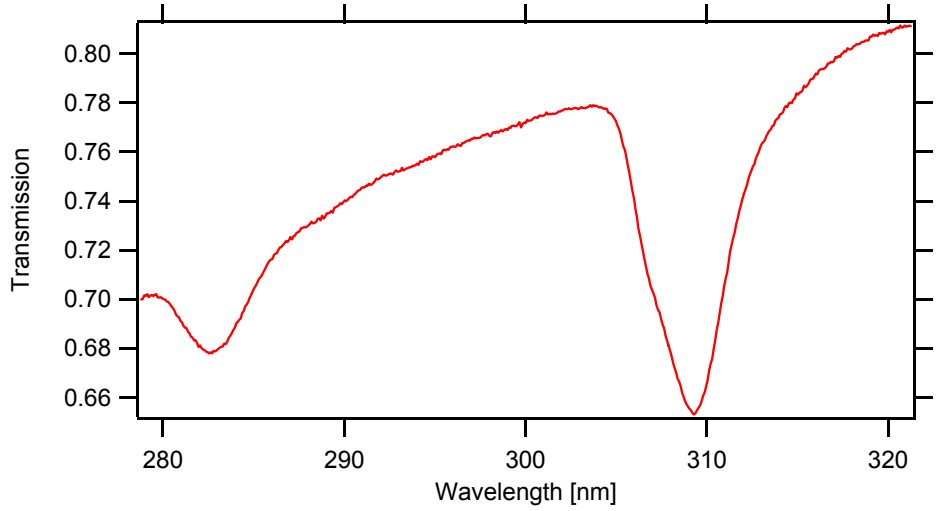

Figure 4-14. Transmission spectrum highlighting broadband absorption.

This background shape change was very regular in cases that exhibited absorption, and was attributed to a broadband absorption caused by other combustion intermediates. Figure 4.15, a direct comparison of motored and fired spectra, indicates that they are in fact not the same shape, so a correction factor had to be introduced in order to isolate the OH absorption from the broadband absorption.

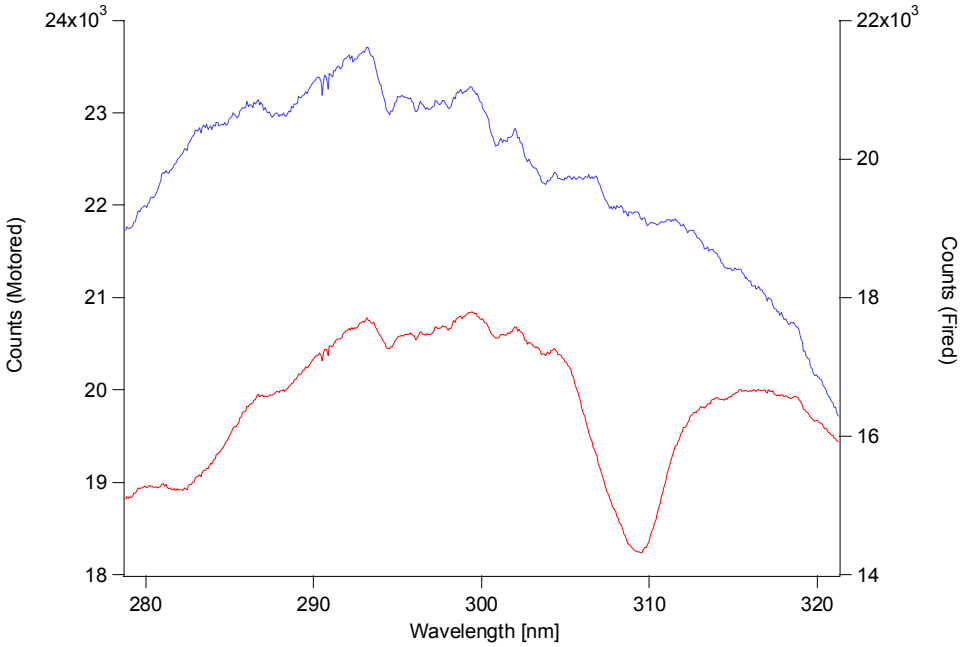

Figure 4-15. Transmission spectrum highlighting broadband absorption.

4.4.3. Characterization of background absorption

It was found that a second order polynomial of the form shown in Equation 4.4 very closely approximates the phenomena seen in Figures 4.10 and 4.11.

$$N_i = a_0 + a_1\lambda_i + a_2\lambda_i^2 \tag{4.4}$$

The fit was produced by choosing three points at wavelengths of 279, 297, and 320 nm, which are outside of the OH absorption as illustrated in Figure 4.16.

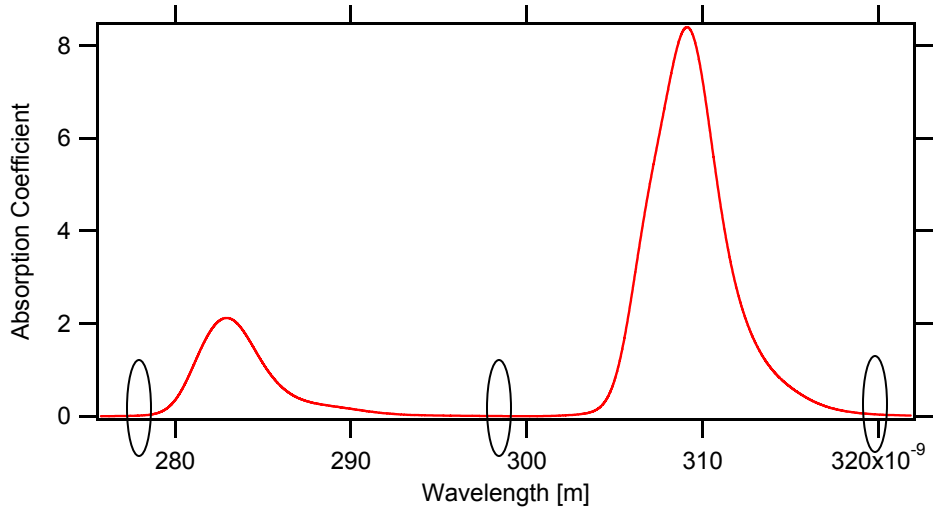

Figure 4-16. Convolved Spectrum highlighting three non-absorbing points (279, 297, and 320 nm) chosen for background fitting.

An EES program calculates a multiplier (N_1, N_2, and N_3) that is a ratio of the magnitude of the fired spectrum to the motored spectrum at each of the three non-absorbing wavelengths. Finally, a set of three equations and three unknowns (Equations 4.5-4.7) are solved to create the polynomial coefficients (a_0, a_1, and a_2) for the fit.

$$N_1 = a_0 + a_1\lambda_1 + a_2\lambda_1^2 \tag{4.5}$$

$$N_2 = a_0 + a_1\lambda_2 + a_2\lambda_2^2 \tag{4.6}$$

$$N_3 = a_0 + a_1\lambda_3 + a_2\lambda_3^2 \tag{4.7}$$

The corrected incident spectrum is then given as:

$$I_{0,CORR} = I_0\left(a_0 + a_1\lambda + a_2\lambda^2\right) \tag{4.8}$$

$I_{0,CORR}$ is then used in equation 4.3 in place of an uncorrected I_0 as the transmission spectrum which is compared to prediction. Figure 4.17 illustrates this comparison of corrected and uncorrected transmission spectra, to the corresponding predicted spectrum, using the baseline curve fit calculated by the EES program.

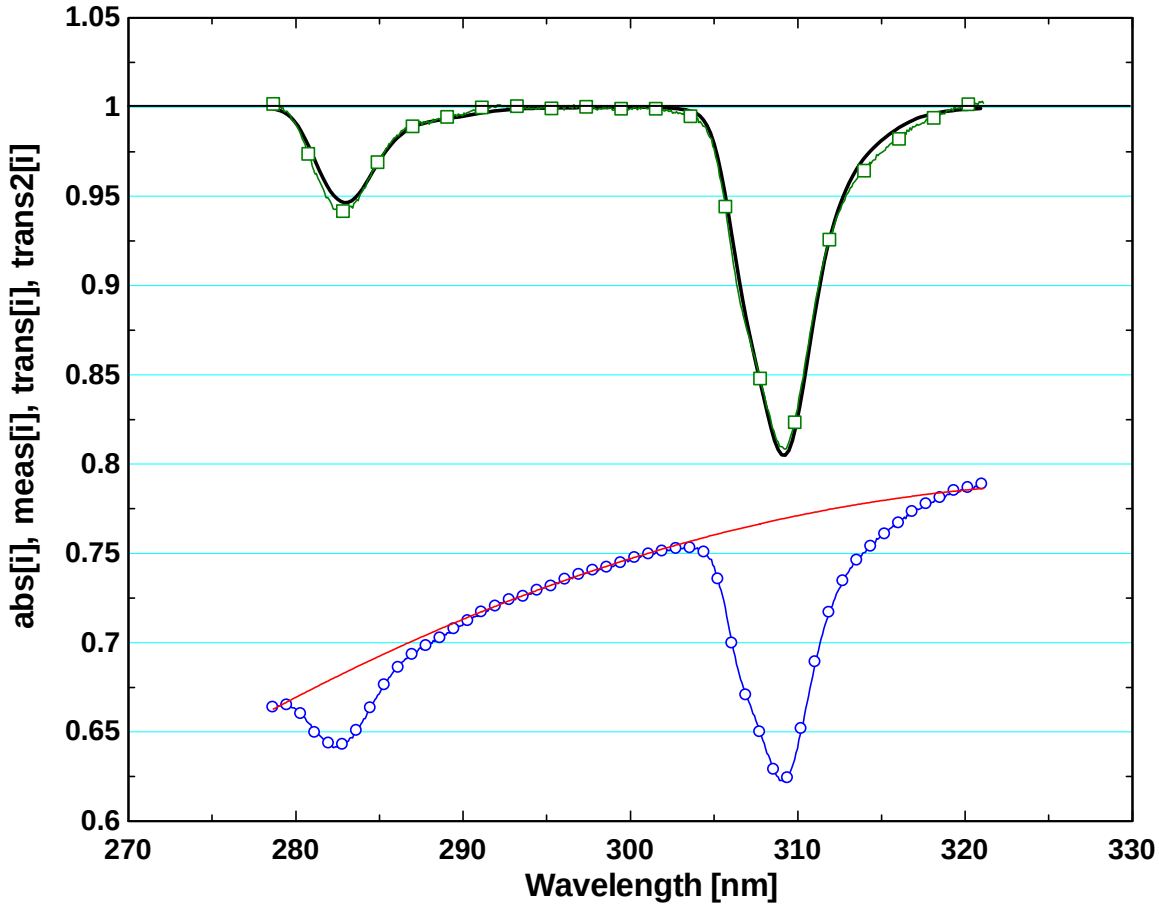

Figure 4-17. Comparison of $\frac{I}{I_0}$ (circular markers), $\frac{I}{I_{0,CORR}}$ (square markers), and calculated absorption (solid line). The baseline curve fit is shown next to the uncorrected spectrum.

The difference in corrected and uncorrected cases is clear. As all non-absorbing wavelengths show a value very close to one in the corrected transmission spectrum, the fit proposed seems appropriate. The EES code for this process is reproduced in Appendix F.

4.5. Final data processing and comparison to prediction

Finally, a program was needed to compile all the data and fit the experimental data to predicted spectra for the same conditions. This program was created in the EES

environment, and includes the polynomial fit described in the previous section. For each case, the EES program takes as inputs: the motored and fired optical data, the fired pressure trace, and cylinder temperature as a function of crank angle. Each run of the program processes these data at points corresponding to the fifteen unique spectra taken by the CCD camera. Pressure and temperature at these points are used to choose the closest match from a database of simulated spectra output by the Peg-and-Convolve program. The measured spectrum, corrected by the process in the previous section, is then compared to the simulated spectrum and the mean squared error between the two is minimized using concentration of OH as the independent variable. The computed best value of [OH] is taken as the observed concentration in the cylinder for that measurement. A sample graph which compares these data is shown in Figure 4.18.

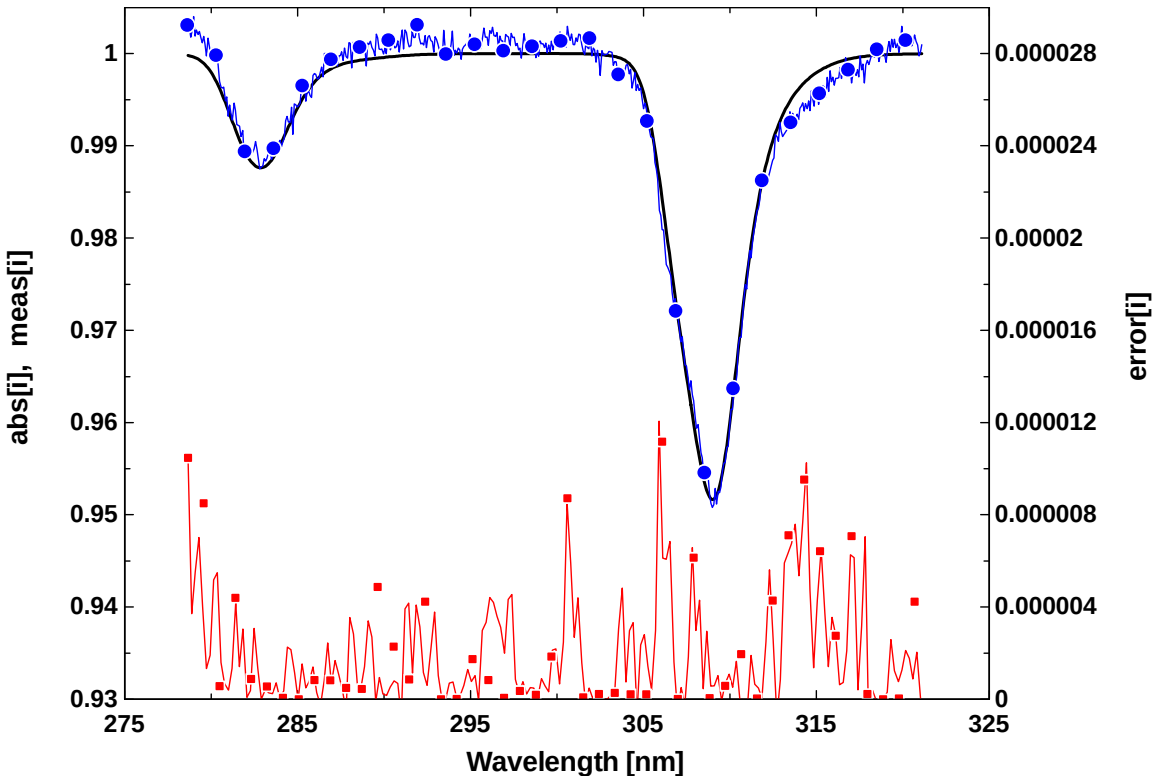

Figure 4-18. EES compiler program output, comparison of prediction to experiment, and measure of error.

Here, the solid curve at the top represents the predicted transmission derived from the database. The curve with circular markers represents the corrected, measured transmission spectrum from the camera. The bottom curve, measured on the right-hand axis, represents the error between the two. At all wavelengths, error is low compared to the magnitude of absorption. The close agreement seen in the non-absorbing regimes—both should be essentially zero—can be attributed to the success of the polynomial baseline fit. Similar graphs will be used to discuss optical results throughout Chapter 5. The EES code for this program which includes the background characterization described in section 4.4.3 can be found in Appendix F.

5. Results

This chapter will summarize the optical, pressure, and emissions data collected and show how these data relate to each other.

5.1. Testing Procedure

All optical data taken were averaged over 200 cycles unless noted, and were obtained in three parts. First, an incident spectrum was taken while the engine was motored. Next, the transmitted spectrum was taken while the engine was fired. Lastly, a second incident spectrum was taken while motored. This was done because fouling of the windows in the spacer ring could significantly change the shape and intensity of output spectra. By taking both pre-fired and post-fired motored spectra, this effect could be quantified and examined. Results of this examination are presented in section 5.4.1. Pressure data were acquired simultaneously during the pre-motored and fired spectrum acquisition.

Data were taken with intake mixtures of 100% air, 50% Argon diluent, and 25% CO_2 diluent. Diluted mixtures were created using the calibrated orifices (see: Appendix A) as the regulators. First, the flow was adjusted to set intake surge tank pressure to atmospheric (101.3 kPa) as the engine ran at 600 RPM. The orifice upstream pressure that gave the correct surge tank pressure was recorded, and the air mass flow rate at that condition was calculated from the appropriate calibration curve. The percentage of air in the diluent cases was calculated on a mass basis. For example, in the 50% air/50% Argon case, the 100% air mass flow rate was halved and an appropriate orifice and upstream pressure were chosen to achieve that reduced mass flow rate. The diluent gas flow rate

was increased from zero until the intake surge tank pressure returned to atmospheric at 101.3 kPa. All tests were conducted at an intake temperature of 90º C.

Five sets of data were taken with each intake condition, differentiated by the mass of fuel injected. Fuel/air equivalence ratio is defined as:

$$\Phi = \frac{(F/A)_{Actual}}{(F/A)_{Stoic}} \tag{5.1}$$

where an equivalence ratio of 1 represents a stoichiometric combustion [6]. This was calculated for all conditions tested. All test cases are summarized in Table 5.1.

	Delivered Equivalence Ratio		
Fuel Mass *[mg/cycle]*	**Argon Diluent**	**No Diluent**	**CO2 Diluent**
4	0.2507	--	--
5	0.3134	--	--
6	0.3761	--	--
7	0.4388	0.2269	--
8	0.5014	0.2593	--
9	--	0.2917	--
10	--	0.3241	--
11	--	0.3565	0.4754
12	--	--	0.5186
13	--	--	0.5618
14	--	--	0.6050
16	--	--	0.6915

Table 5-1. Summary of test cases.

Equivalence ratios are different for similar fuel masses with different intake compositions because equivalence ratio is based on a mass ratio of fuel to air, not fuel to total intake gas.

5.2. Pressure and heat release data

Figures 5.1, 5.3, and 5.5 show the pressure data for the 100% air cases, the Argon diluent cases, and the CO_2 diluent cases, respectively. A clear distinction can be seen

between fired pressure traces that exhibit single-stage heat release, and those which have two-stage heat release. This distinction is important, since conditions without a two-stage heat release are incomplete and should exhibit the highest CO emissions along with the lowest OH concentrations.

The HRR is a more useful metric of heat release timing and magnitude, and it is plotted versus crank angle for all cases in Figures 5.2, 5.4, and 5.6. The heat release data, show more clearly that only the single-stage heat release is present for the lowest fuel rates. The heat release rate (HRR) was calculated in EES. The program takes the motored and fired pressure traces from each case as inputs, and outputs total heat release and rate of heat release at every crank angle step specified. The primary equation used in the heat release calculation is:

$$\frac{dQ_{HR}}{d\theta} = \frac{V}{\gamma - 1}\frac{dP}{d\theta} + \gamma \tilde{P}\frac{1}{\gamma - 1}\frac{dV}{d\theta} \tag{5.2}$$

where γ is the ratio of specific heats, V is cylinder volume, and $\tilde{P} \equiv P_f - P_m$. The EES code for this program is included in Appendix G.

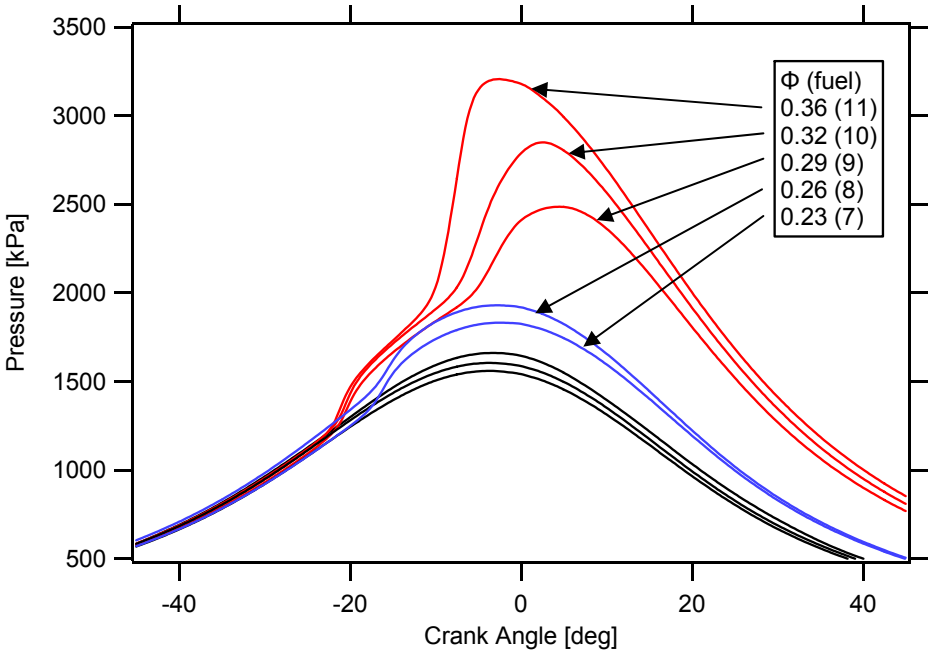

Figure 5-1. 100% Air pressure data.

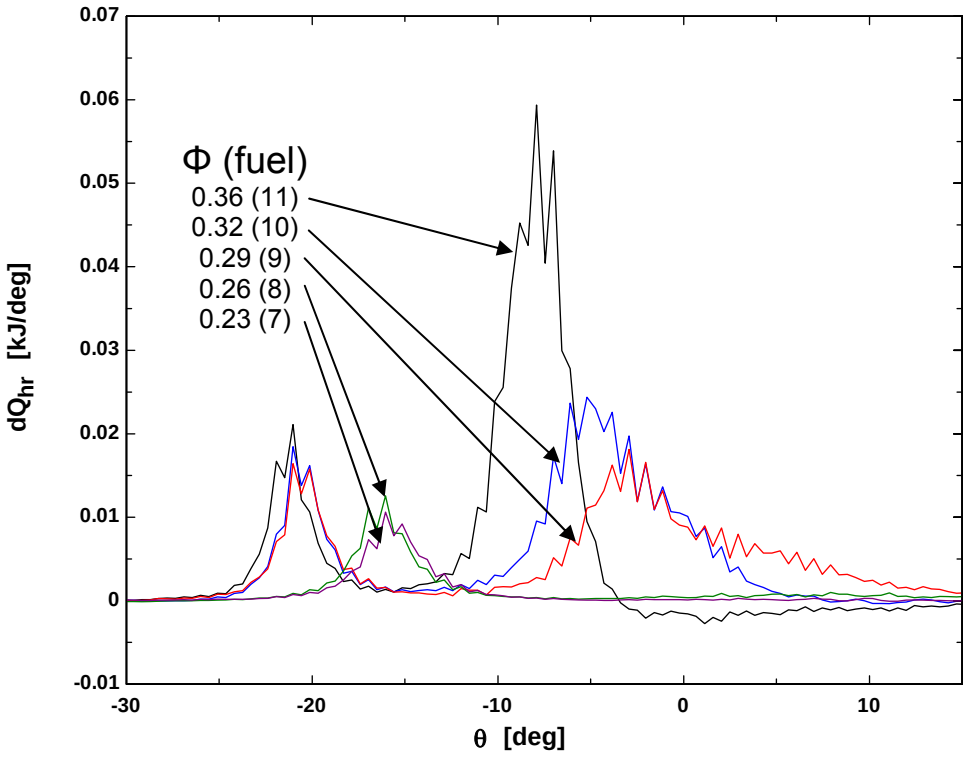

Figure 5-2. 100% Air heat release data.

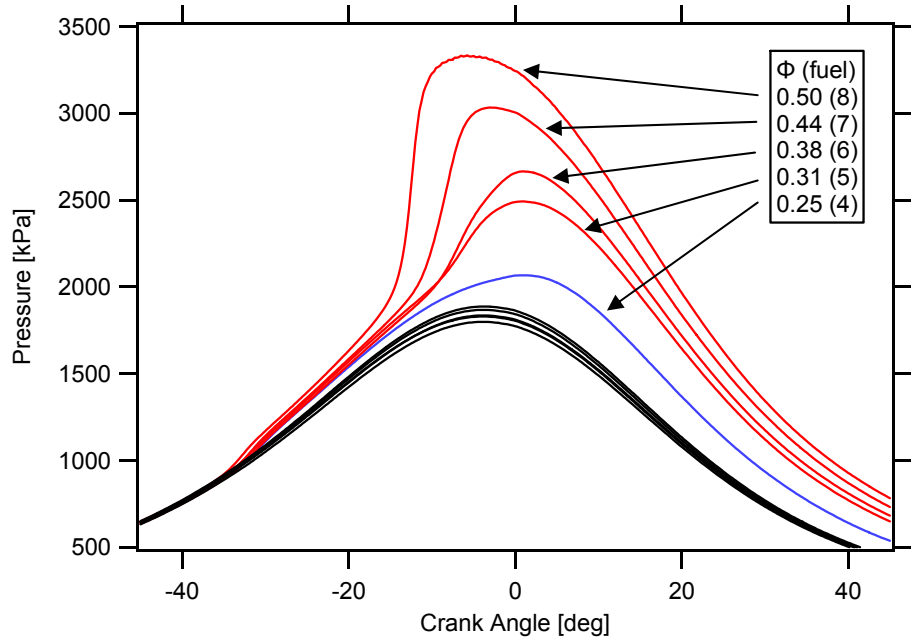

Figure 5-3. 50% Argon diluent pressure data.

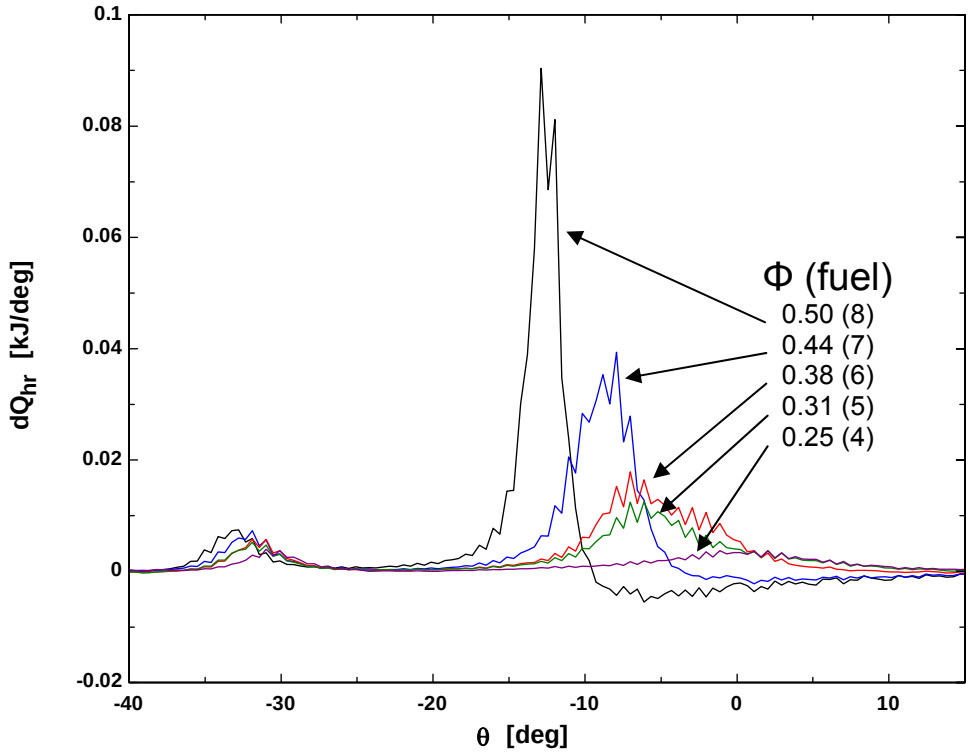

Figure 5-4. 50% Argon diluent heat release data.

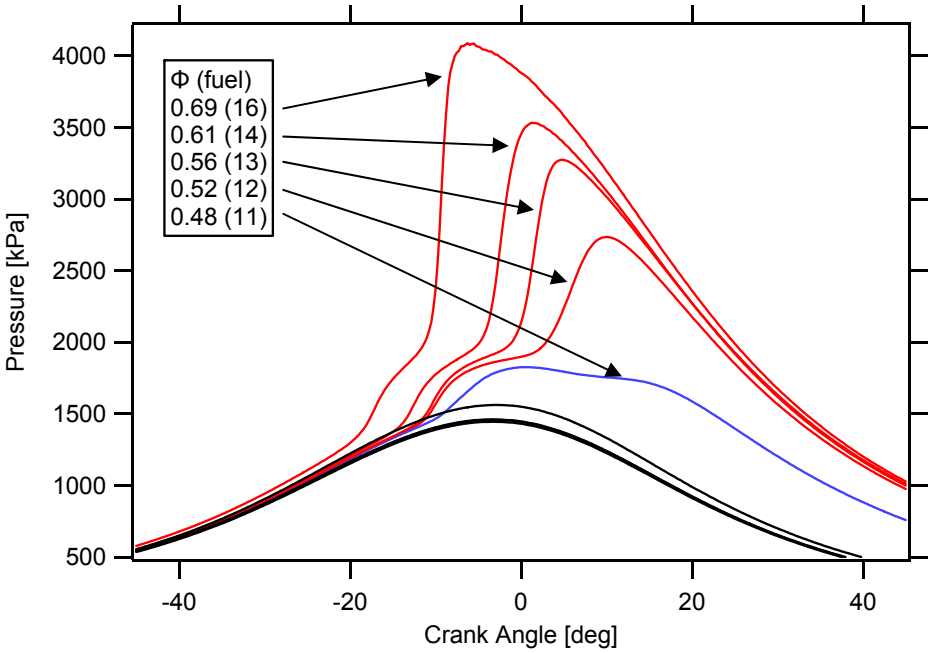

Figure 5-5. 25% CO2 diluent pressure data.

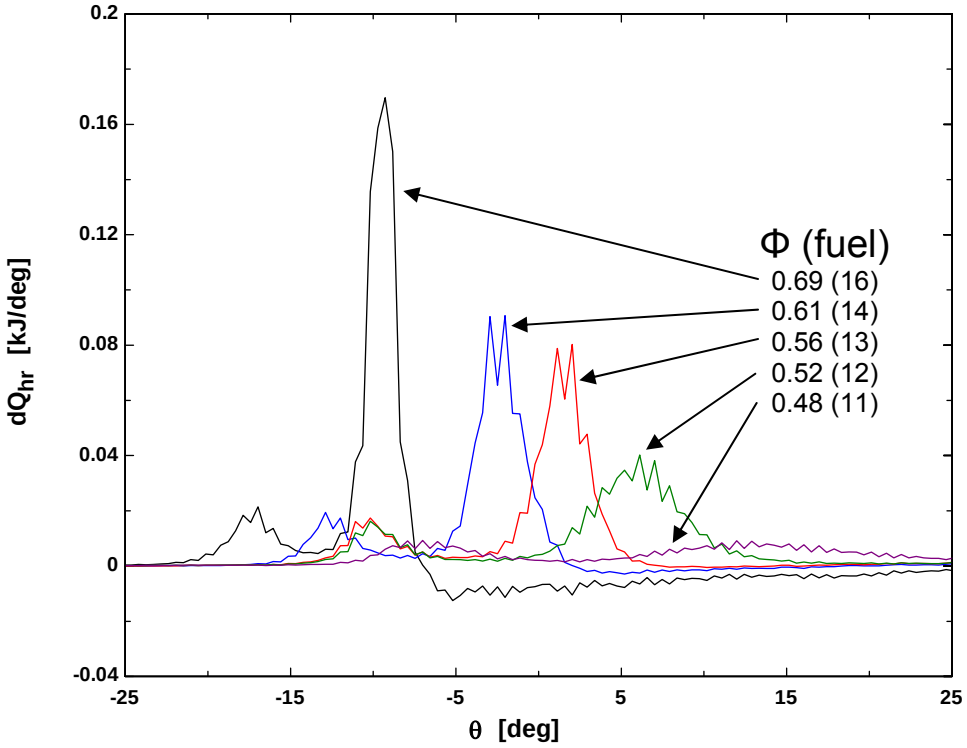

Figure 5-6. 25% CO2 diluent heat release data.

The lowest fuel mass Argon and CO_2 cases exhibit a small second-stage ignition, that can be seen most clearly in the heat release plots. This will be important as emissions are discussed in the next section.

5.3. Emissions data

Emissions measurements were performed using the standard five-gas analysis discussed in section 3.3.2. Using atom balances, the emissions data can provide an estimate of the equivalence ratio. Figure 5.7 shows delivered equivalence ratio (Φ_{Del}) plotted against an equivalence ratio calculated from emissions measurements (Φ_{Emiss}). The good correspondence between Φ_{Del} and Φ_{Emiss} gives confidence in the emissions measurements.

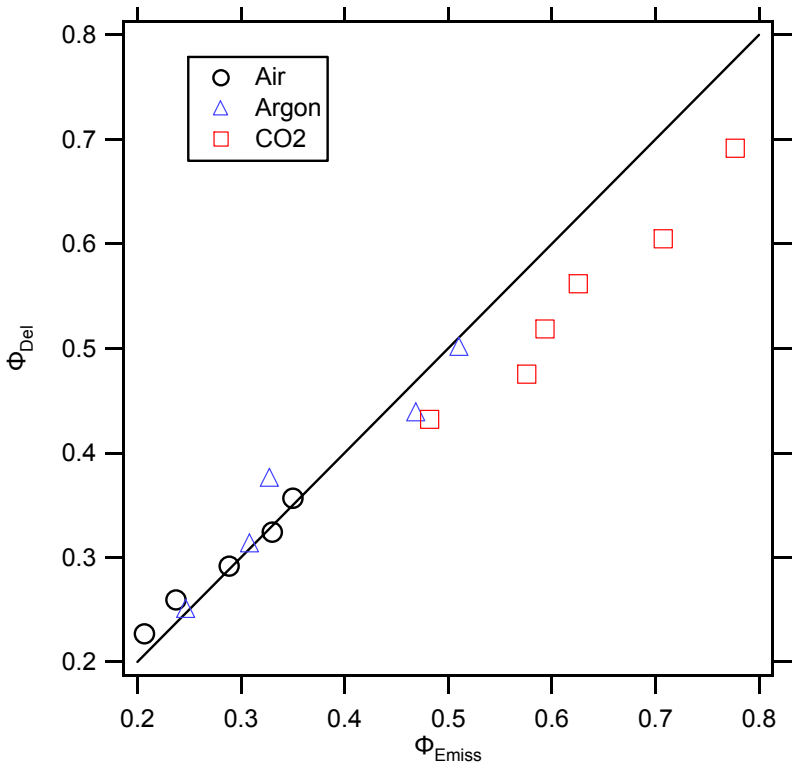

Figure 5-7. Delivered equivalence ratio versus equivalence ratio measured from emissions.

The emissions data were used to calculate the Emissions Index of CO (EICO) in a manner that included the dilution effects of the diluent gases. EICO is the measured mass flow rate of exhaust CO normalized by mass flow rate of fuel into the cylinder.

$$EICO = \frac{\dot{m}_{CO}}{\dot{m}_{fuel}} = \frac{g_{CO}/s}{kg_{fuel}/s} = \frac{g_{CO}}{kg_{fuel}} \tag{5.3}$$

The plot in Figure 5.8 shows EICO versus fuel mass injected for all data points. It can be seen that as fuel mass decreases CO emissions increase, but the transition occurs at different fuel masses depending on the diluent.

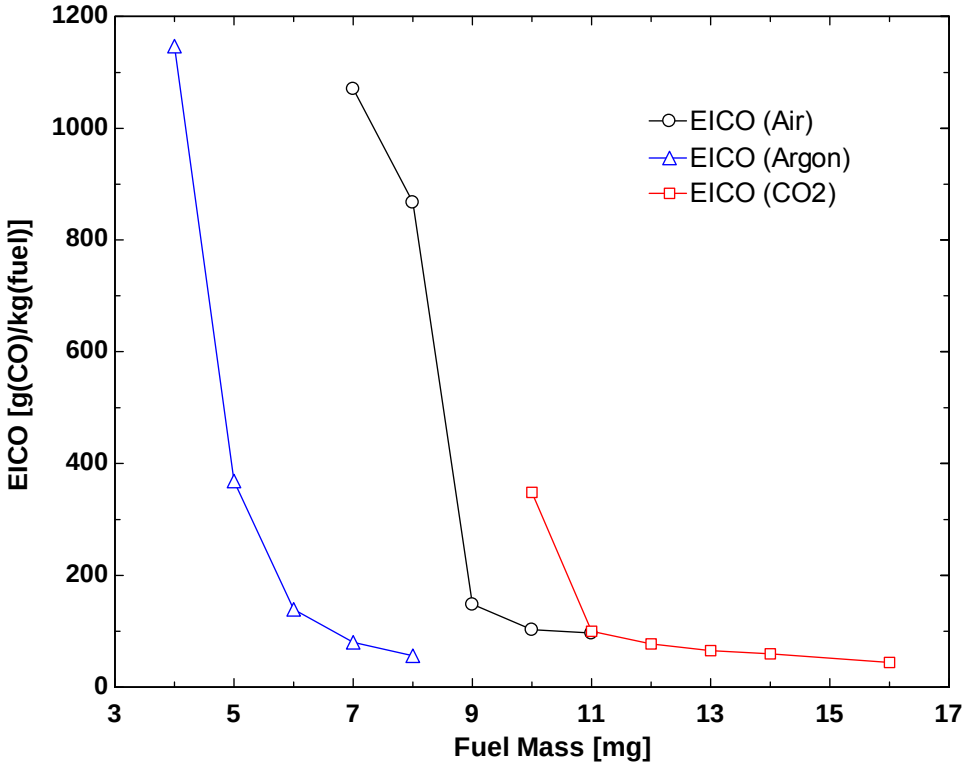

Figure 5-8. EICO versus fuel mass injected.

The observed CO emission trends are explainable based on temperature arguments. If 100% air is the baseline, the 50% Argon mixture has a lower specific heat. This means that it is easier to achieve the critical temperature for CO oxidation, so complete combustion can occur at lower fuel mass inputs. The opposite is true for the CO_2 diluent case: its higher specific heat than air makes it harder to increase temperature, and higher fuel mass inputs are required for complete combustion. The effect of CO_2's specific heat on the mixture properties is so great that a 50/50 air/CO_2 intake charge could not be used because the mixture would not ignite at all, even at fuel mass conditions approaching stoichiometric.

Figure 5.9 replots the EICO information in Figure 5.8 against equivalence ratio. The argon and CO_2 curves shift relative to the air curve due to the dilution effect. They each have less than 100% air, so their diluted equivalence ratios become proportionately higher. EICO and Φ_{Emiss} data are calculated by an EES program reproduced in Appendix H.

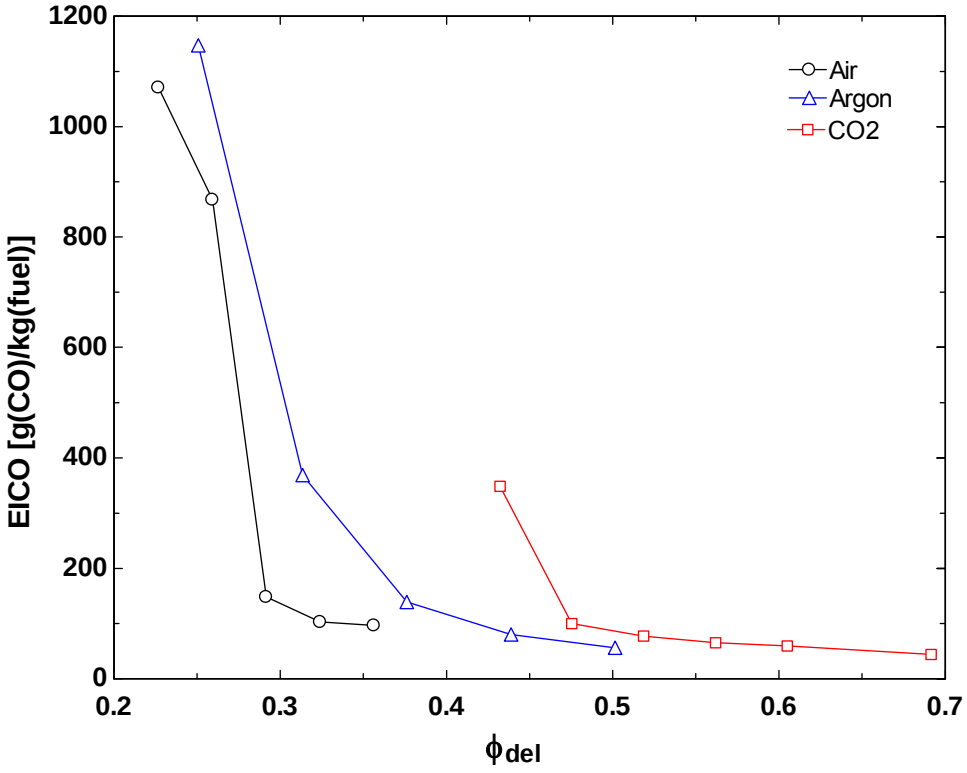

Figure 5-9. EICO versus delivered equivalence ratio.

Figure 5.10 shows the HRR for cases on the low-CO side of the sudden increase in CO, including 100% air at 9 mg fuel, 50% Argon at 6 mg fuel, and 25% CO_2 at 11 mg fuel. All three cases exhibit a strong second stage ignition.

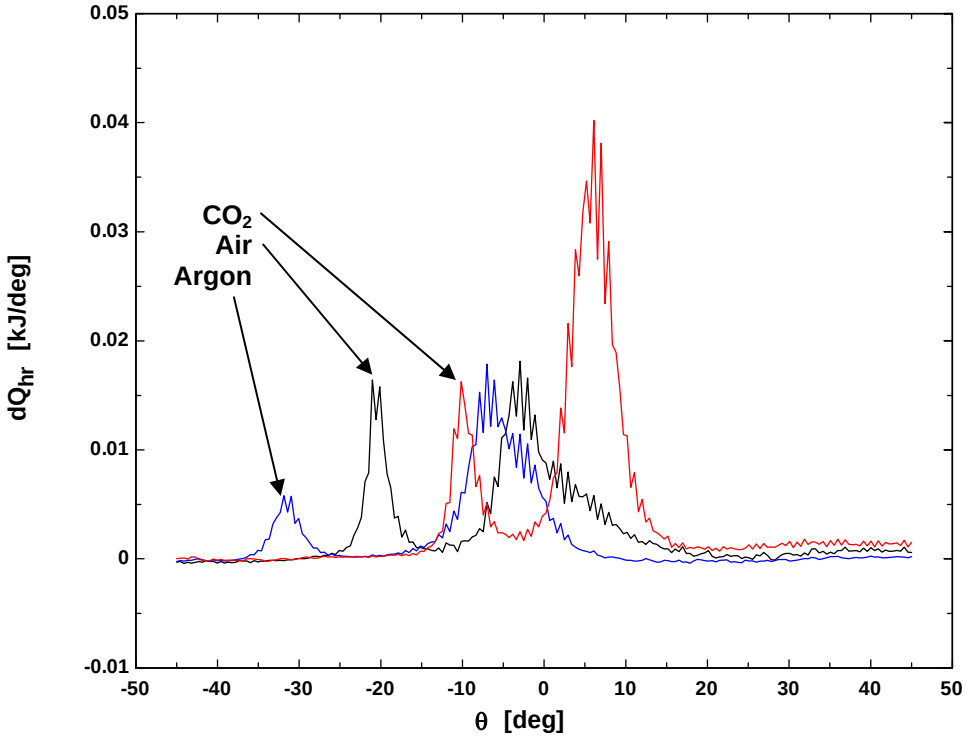

Figure 5-10. Heat release data for marginal cases which do absorb OH, and have a relatively low EICO.

The HRR for cases on the high-CO side of the transition are plotted in Figure 5.11, including 100% air at 8 mg fuel, 50% Argon at 5 mg fuel, and 25% CO_2 at 10 mg fuel. Here a second stage ignition can still be seen in the Argon and CO_2 data, although it is substantially smaller than in Figure 5.10. No second-stage ignition is observed in the air case. This agrees with the emissions data. In Figure 5.8, the jump from low CO to high CO emission as fuel mass is decreased is far more drastic for the air case than either the Argon or CO_2 case. Where 100% air EICO goes from 148 to 867.6—an increase of 719.6 g/kg—Argon and CO_2 only increase by 229.5 and 248.6 g/kg, respectively in the same fuel mass step size.

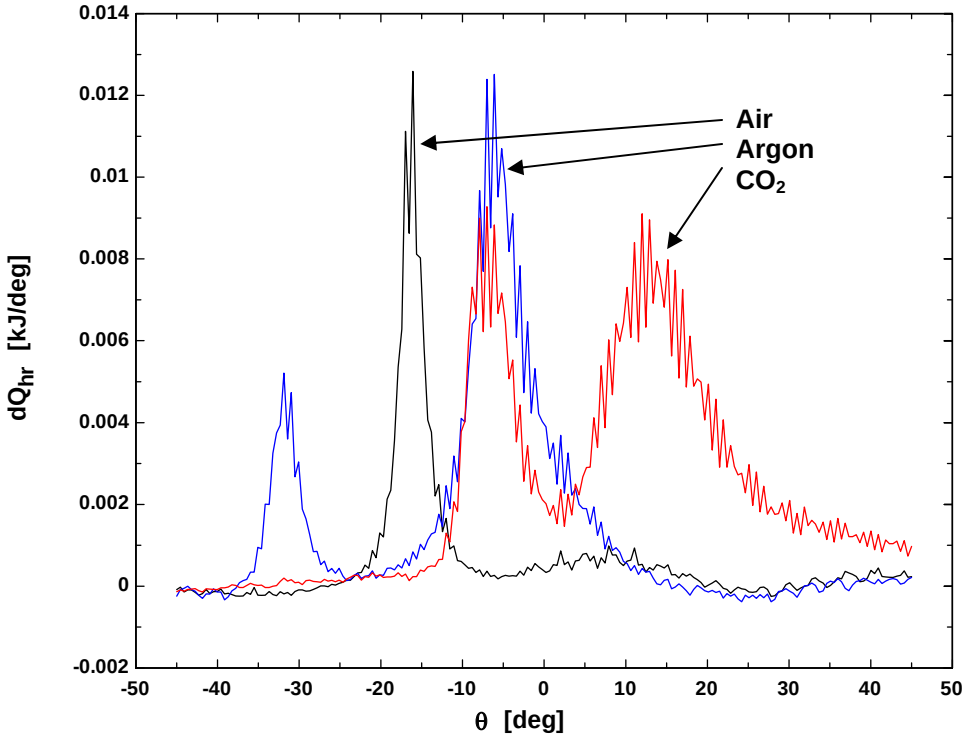

Figure 5-11. Heat release data for marginal cases which do not absorb OH, and have a relatively high EICO.

One feature which is more apparent in Figures 5.10 and 5.11 than in the composition-separated heat release plots is the relative HRR timing for each diluent. Both Figures 5.10 and 5.11 show a result that follows closely with theory. The 50% Argon mixture has a lower specific heat, so it is easier to change the temperature of the intake charge, and in turn easier to make the mixture combust. As a result, ignition happens earlier in the cycle, and combustion quality similar to the pure air case can be achieved at lower fuel mass inputs. In the case of the CO_2 diluent, its higher specific heat than air makes it harder to heat up, ignition happens later in the cycle, and higher fuel mass inputs are required.

5.4. Optical Data

5.4.1. Window fouling

Some examples of motored spectra acquired before and after firing the engine are shown in Figure 5.12, which is meant to illustrate the fouling effect. In all instances, but to varying degrees, both the spectral shape and the intensity at all wavelengths were affected by firing the engine.

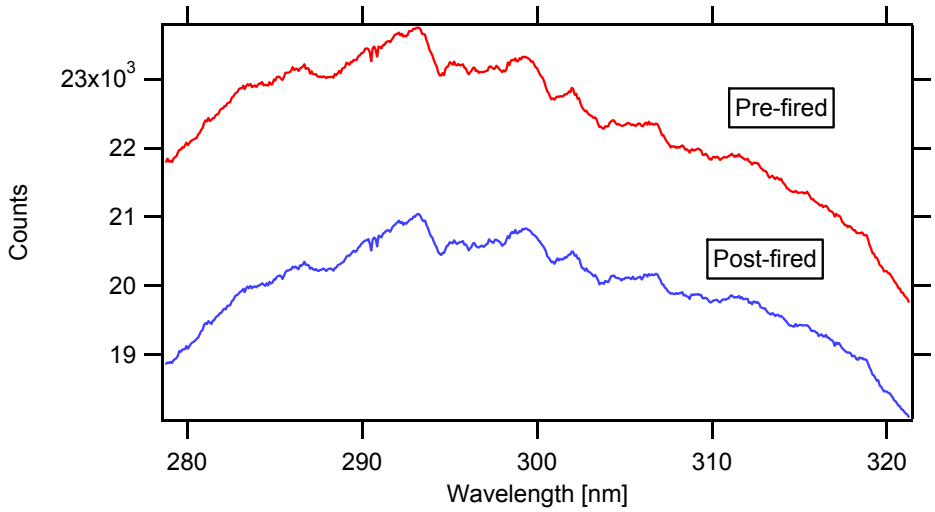

Figure 5-12. Comparison of pre-fired and post-fired motored cases, "high" equivalence ratio: 100% air, 11 mg/cycle.

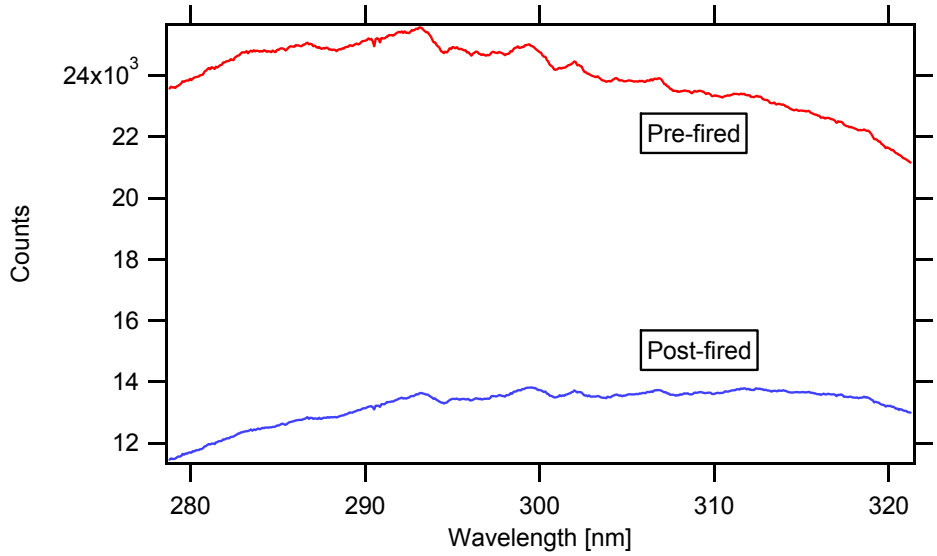

Figure 5-13. Comparison of pre-fired and post-fired motored cases, "moderate" equivalence ratio: 100% air, 9 mg/cycle.

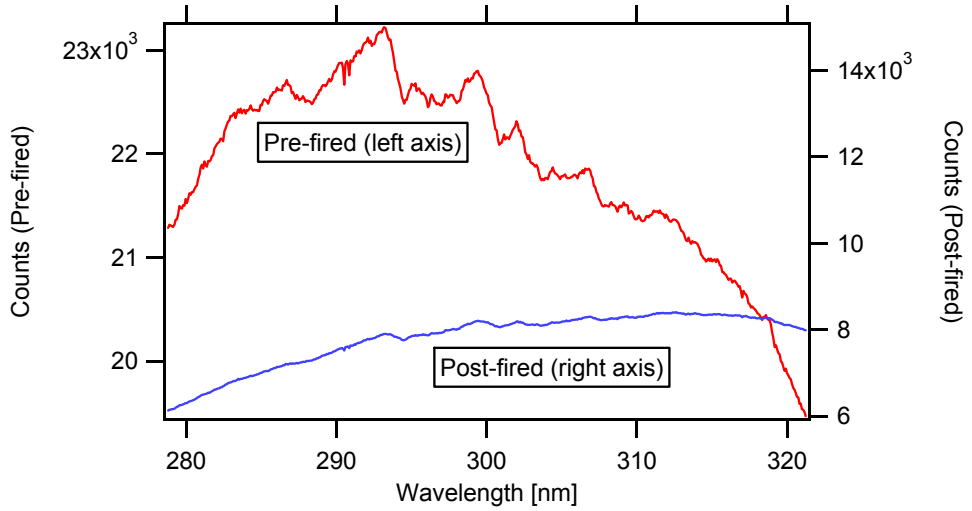

Figure 5-14. Comparison of pre-fired (left axis) and post-fired (right axis) motored cases, "low" equivalence ratio: 100% air, 7 mg/cycle.

In the progression from high equivalence ratio (Figure 5.12) to low equivalence ratio (Figure 5.14) the quality of the second motored spectrum is increasingly affected. In Figure 5.14, the intensity difference between the pre- and post-motored cases is so great that they must be graphed on different axes. In addition, the change in spectral

shape is far more drastic. Since this fouling effect has such an obvious negative influence on the optical data, the spacer ring windows were cleaned after each data set was taken.

Initially, it was thought that the window fouling was simply a cumulative process of fuel intermediates and combustion products condensing on the relatively cool surfaces of the cylinder walls and building up a film which made the windows increase in opacity. Tests were performed which proved that this was not entirely the case. A low equivalence ratio condition was run until the windows fouled, and then a much higher equivalence ratio was run with results shown in Figure 5.15. The windows were in fact "cleaner" in terms of transmitted light after the second run than the first, which would contradict a theory of a constant, slow buildup. As such, in addition to running time, the fouling effect is thought to be a function of cylinder temperature where a weak heat release is not as effective as a strong heat release at vaporizing the condensed substances on the windows.

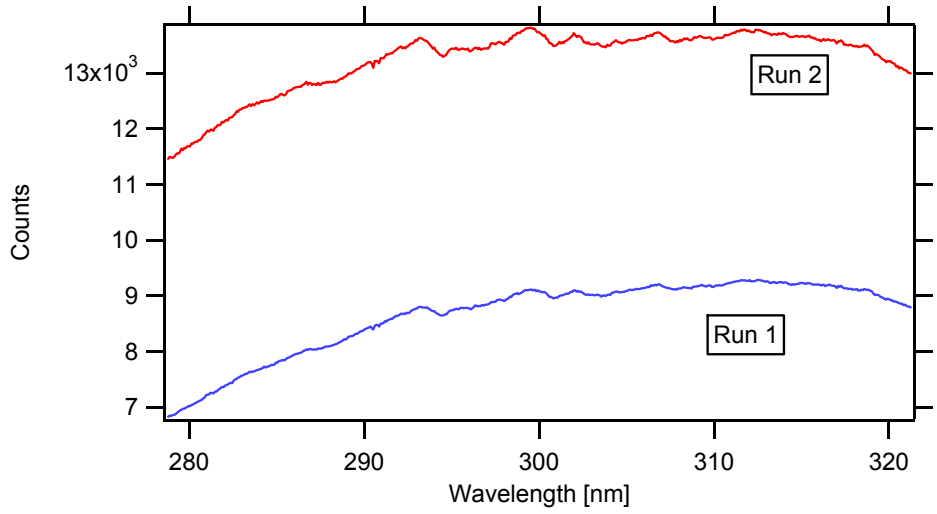

Figure 5-15. Motored traces after Run1 (low equivalence ratio) and Run2 (high equivalence ratio).

5.4.2. Qualitative assessment of optical data

Figures 5.16-5.17 show sample optical data which presents the full information from the Fast Kinetics mode sweep. All 15 "pictures" (spectra) that the camera takes in one capture cycle are shown. Figure 5.16 is a transmission spectrum with strong OH absorption, with the characteristic OH absorption features of Figures 2.8, 4.6, 4.13, and 4.16 easily seen as removed from the changing baseline. Figure 5.17 is a case at a lower equivalence ratio which does not exhibit visible OH absorption, even after processing, although there is a very high overall absorption.

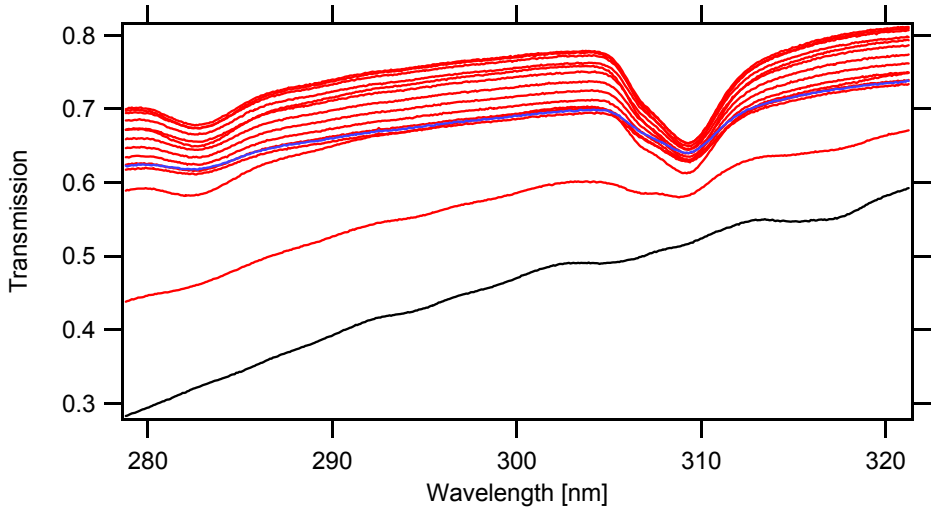

Figure 5-16. Sample optical sweep with strong OH absorption, 100% air, 11 mg/cycle.

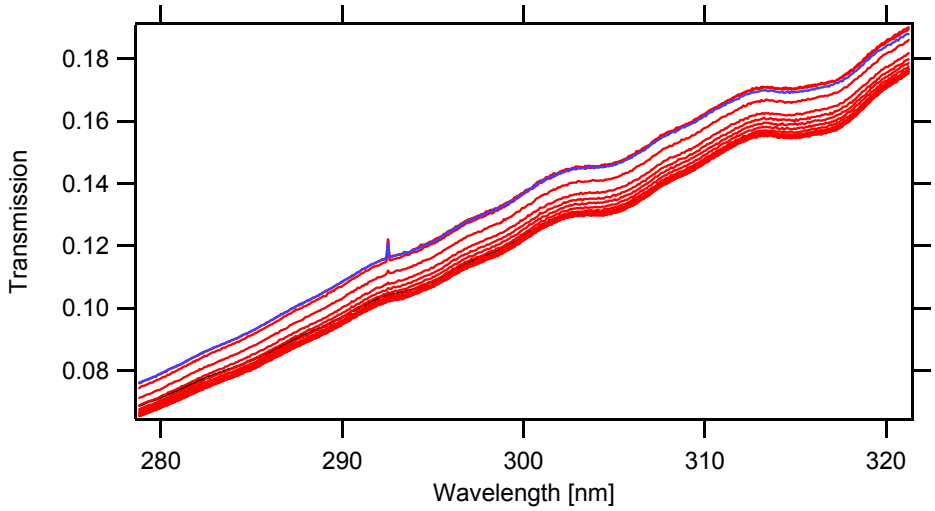

Figure 5-17. Sample optical sweep with no OH absorption, 100% air, 8 mg/cycle.

To give a full picture of the absorption process during the cycle, Figure 5.18 shows a sample pressure and heat release trace with absorption profiles pointed out for those conditions at various points throughout the cycle. Here a progression from low background absorption (before -11.6 CAD), to dominant background absorption (-11.6 to 0.8 CAD), to increasing OH absorption (0.8 to peak at 8 CAD), to gradual falloff of OH absorption (after 8 CAD) can be seen. Spectra from 2.6 CAD onwards are graphed on the same scale for the purpose of comparing absorption peak heights.

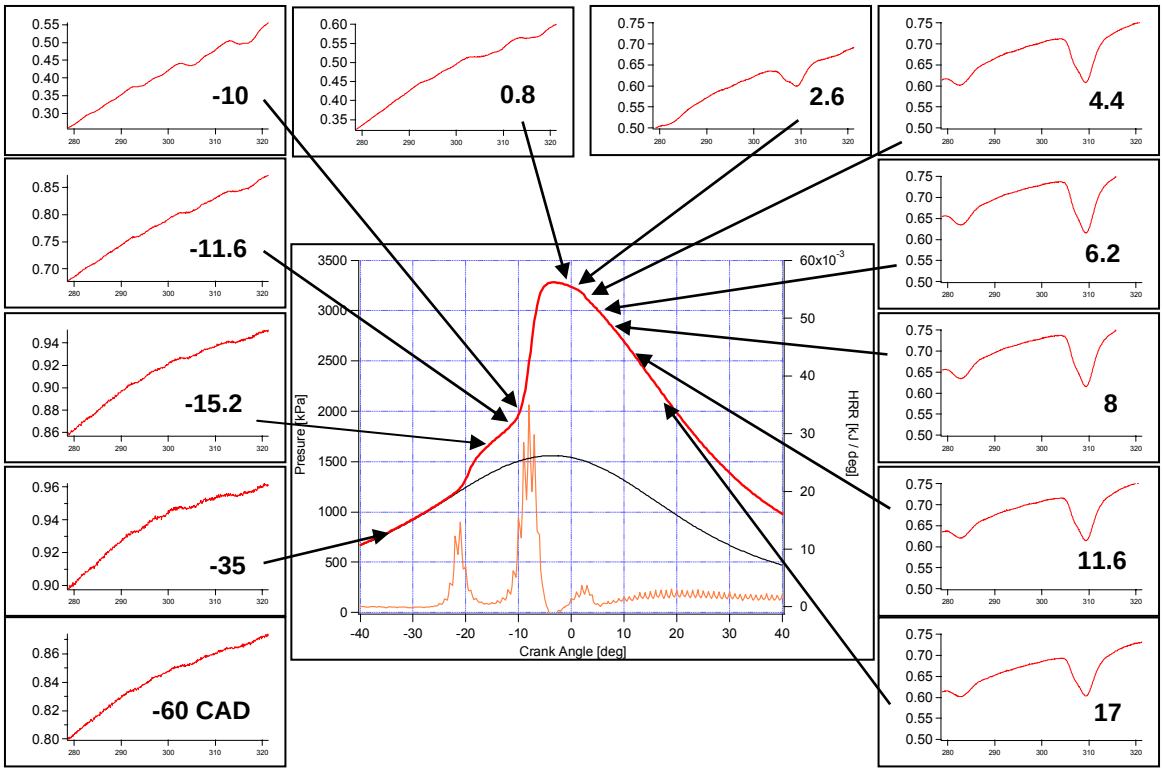

Figure 5-18. OH absorption at various points in the cycle: 100% air, 11 mg/cycle.

When crank angle timing was considered, it was noted that OH formation and absorption do not occur until well into the second stage of heat release. The first indication of OH absorption in Figure 5.12 happens around 0.8º BTDC. OH absorption remains strong very late into the expansion stroke and this effect is due to temperature remaining high well after TDC as shown in Figure 5.19.

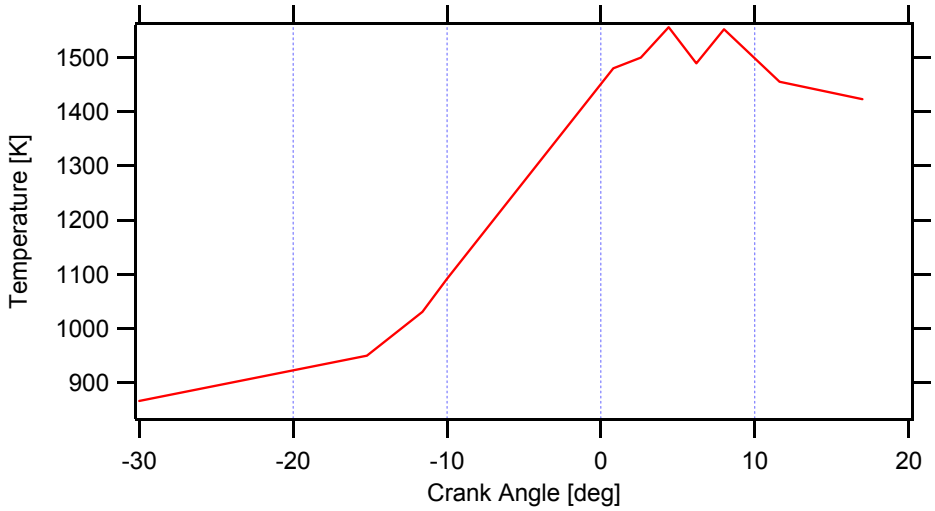

Figure 5-19. Temperature versus crank angle for the case shown in Figure 5.12. Note that cylinder temperature remains high even at 17º ATDC, the last data point.

5.4.3. Quantitative analysis of optical data.

Next, the OH absorption data are summarized in plots that show OH concentration vs. time for each equivalence ratio with detectable absorption. Graphed on the same plots are the corresponding heat release curves for the purpose of comparison and to give an idea of the relative timing of the concentration changes. The temperatures used in the spectral fits were provided by Kranendonk [14, 15]. Only cases that gave fit spectra representative of OH absorption are shown in Figures 5.20-5.22.

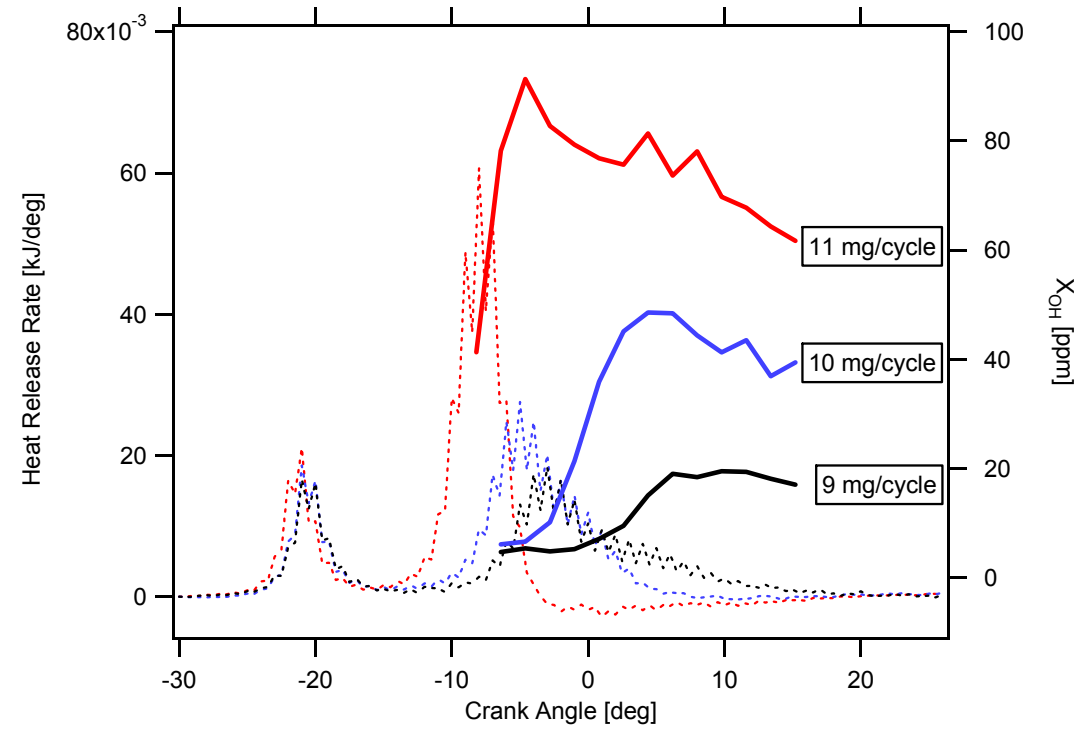

Figure 5-20. OH absorption data (solid lines) shown with heat release data (dotted). 100% air cases.

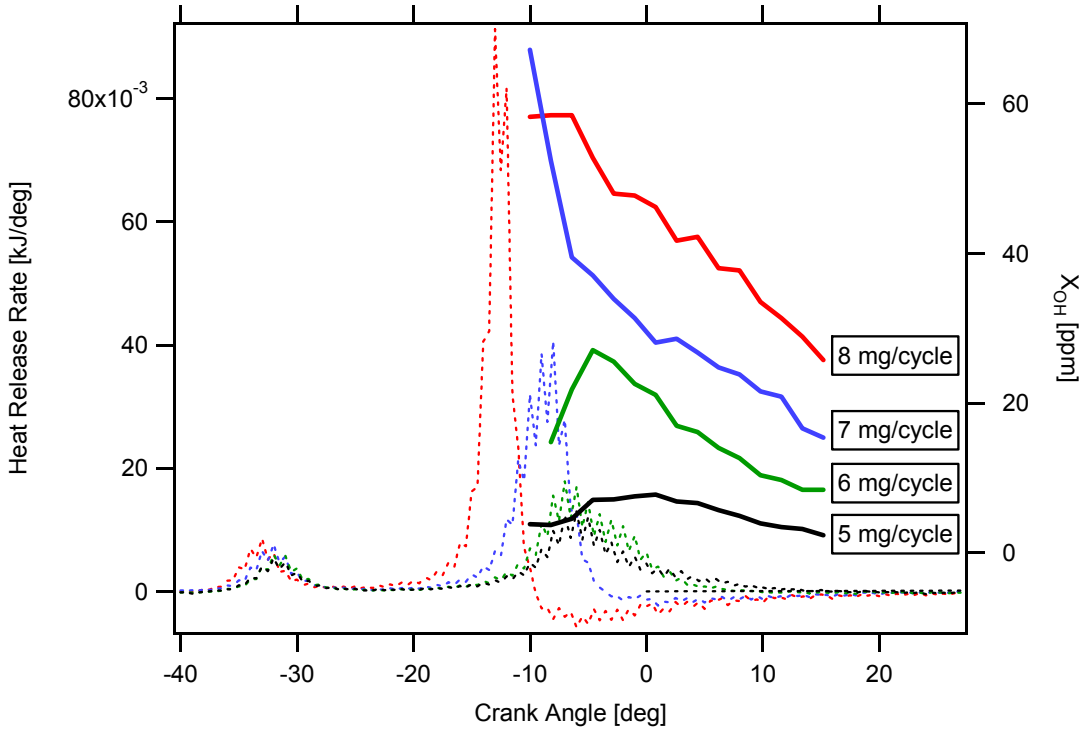

Figure 5-21. OH absorption data shown with heat release data. 50% Argon diluent cases.

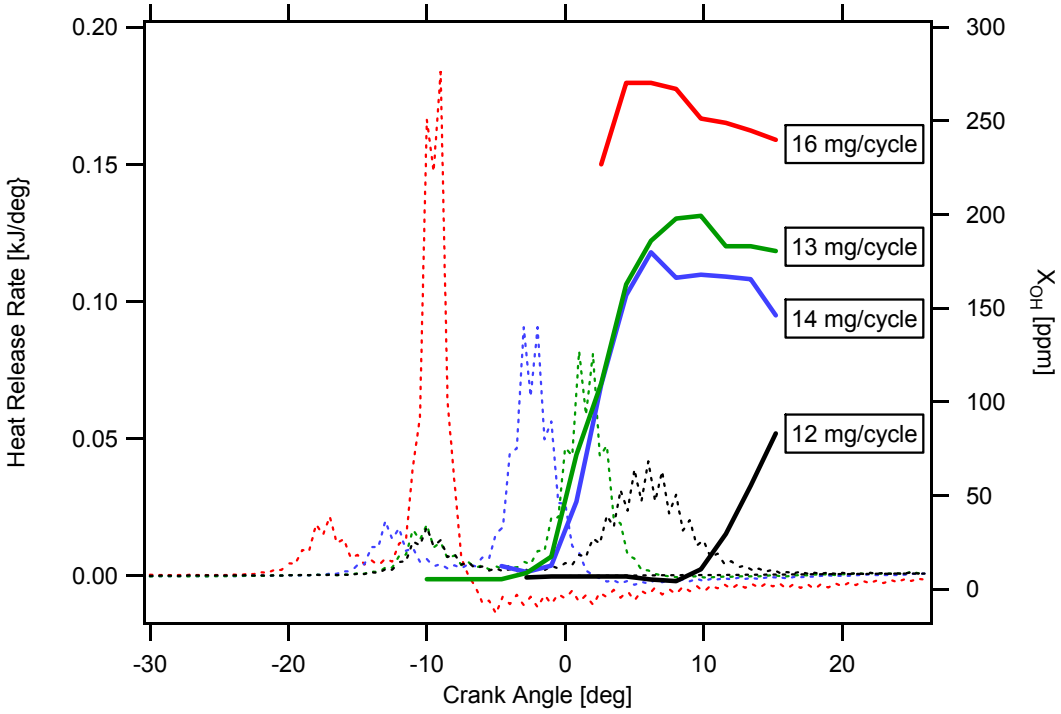

Figure 5-22. OH absorption data shown with heat release data. 25% CO_2 diluent cases.

It should be noted that in general, the decrease in OH concentration vs. crank angle with decreasing equivalence ratio is monotonic, as expected. The only exceptions are the 13 and 14 mg/cycle points of the CO_2 data (Figure 5.22). It is believed that this anomaly is within the error range of the experiment.

Figure 5.23 shows peak OH concentration versus equivalence ratio for all cases that are solvable. It can be seen that at similar equivalence ratios, the 100% air cases exhibit more OH presence than the 50% Argon case. It may seem intuitive that more OH should appear in the Argon diluent cases, since the low specific heat of the mixture makes it easy to heat and temperature is what drives the OH-producing reactions. This is explained, however, by the dilution effect. Although the diluted mixture changes temperature more readily, the oxygen in the OH must come from atmospheric oxygen

(since the fuel is not an alcohol). In the 50% Argon diluted case, there is only 50% of the oxygen available for reaction into OH, and from chemical kinetic theory the rate of that reaction should go down. Figure 5.24 shows that temperatures do in fact remain higher in the 100% air cases than the 50% Argon. The extra oxygen from CO_2 diluent molecules does not have a positive effect on temperature because CO_2 is unreactive at these temperatures—acting as an EGR—and the high specific heat of that mixture drives the peak temperature down at similar equivalence ratios. Overall OH concentrations are still higher in the 25% CO_2 case, however, because the fueling rates required to make that mixture burn were extremely high. This creates a substantial temperature rise during combustion which more than compensates for the smaller temperature rise during compression.

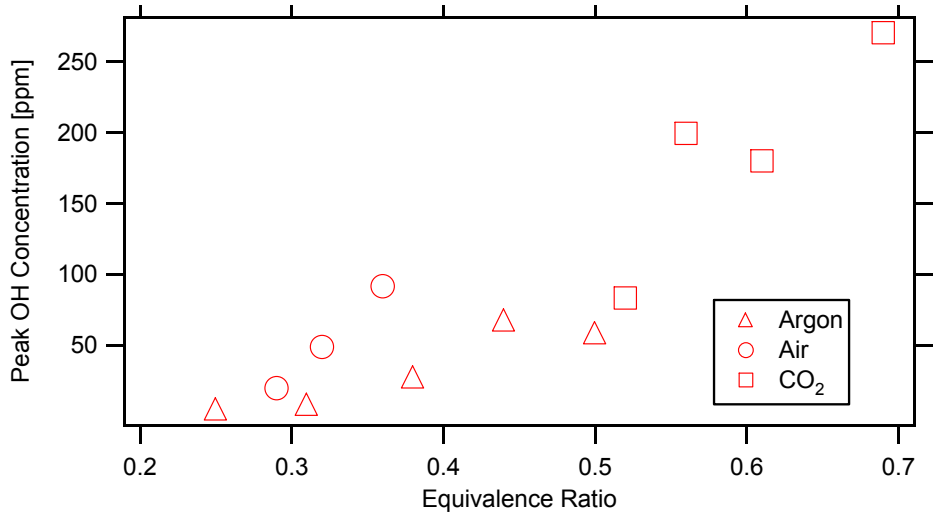

Figure 5-23. Peak OH concentration versus equivalence ratio for 100% Air, 50% Argon, and 25% CO_2 cases which are solvable.

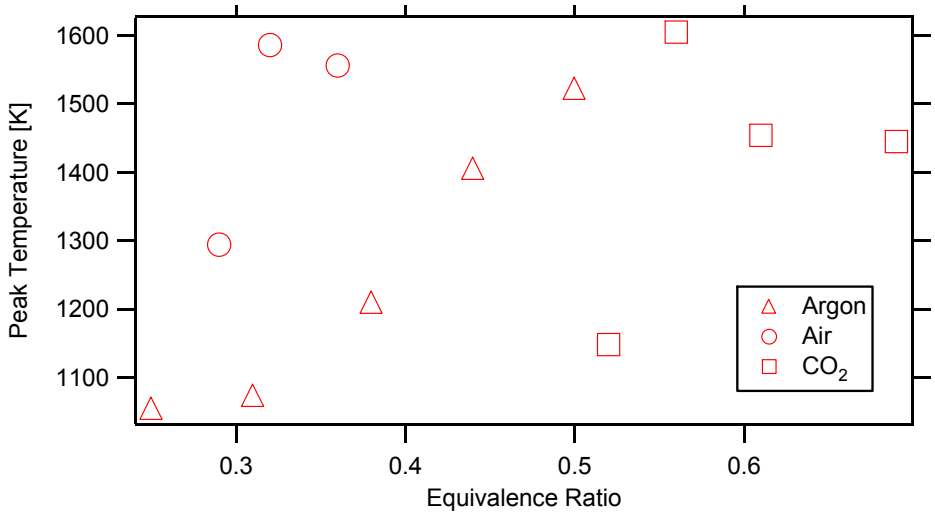

Figure 5-24. Peak temperature versus equivalence ratio for 100% Air, 50% Argon, and 25% CO_2 cases which are solvable.

Figure 5.25 shows peak OH concentration versus peak temperature. There is good agreement in the amount of OH present in the 100% air and 50% Argon mixtures where temperatures are similar, which suggests that OH formation is a function of temperature.

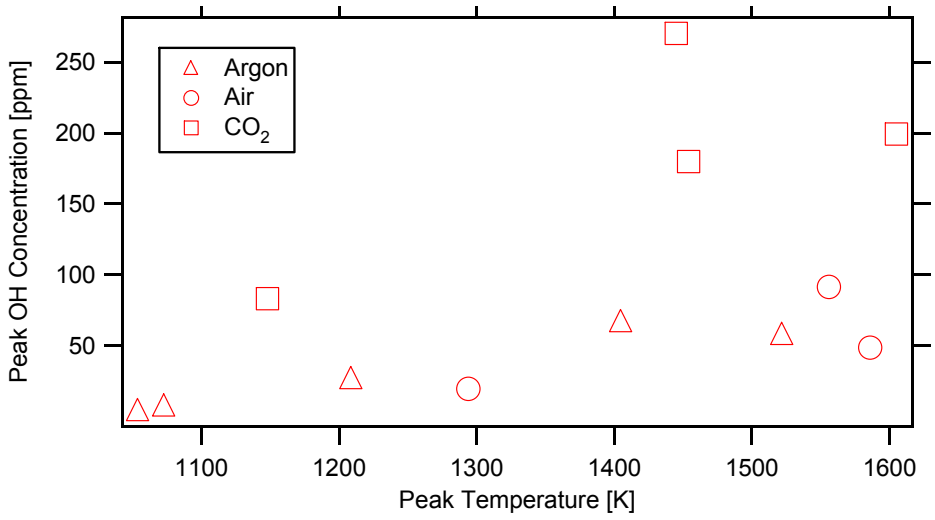

Figure 5-25. Peak OH concentration versus peak cylinder temperature for 100% Air, 50% Argon, and 25% CO_2 cases which are solvable.

5.5. Error Analysis

5.5.1. Temperature error

The main hurdle in this calculation was knowledge of cylinder temperature from the wavelength-agile methods described in section 2.4.3. In general, the temperature data taken were noisy because they were taken in a single cycle, and not averaged over many cycles as the other data (optical—200 cycles, pressure—100 cycles) were. The measured temperature was then rounded to match the increment on the database of absorption profiles (100º C), so the resolution of the database introduces a "bit noise" into the temperature error. Some error in this last stage could be avoided by recalculating predicted absorption based on the temperature measured to make the process iterative. This method was not used here. Examples of temperature versus crank angle data are shown in Figures 5.26 and 5.27.

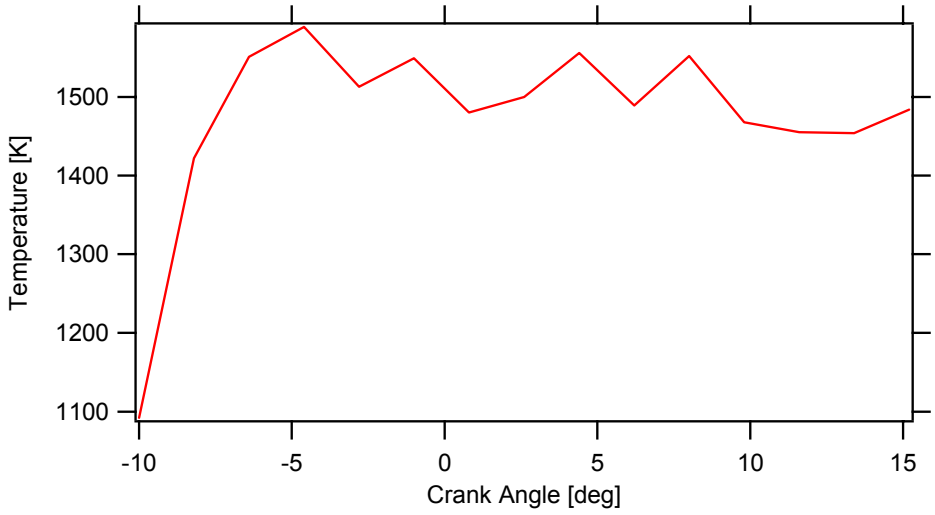

Figure 5-26. Temperature versus crank angle, 100% air, 11 mg/cycle.

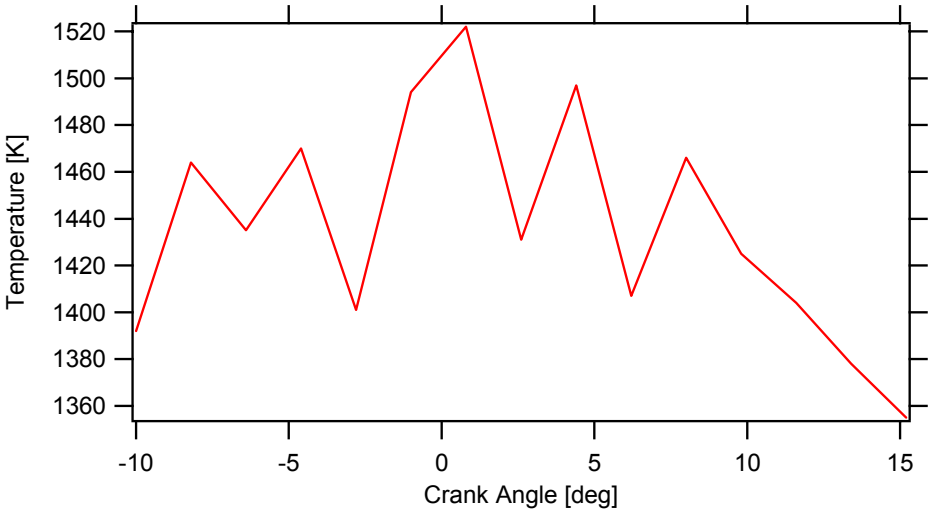

Figure 5-27. Temperature versus crank angle, 50% Argon, 7 mg/cycle.

A brief error analysis was conducted where measured temperature input was changed by ±100º C. This forces the OH fitting program to lookup the next highest and next lowest database spectra for that case, changing the absorption profile against which the observed spectra is compared. The absorption spectra at fixed X_{OH} is shown in Figure 5.28 with error bars corresponding to the values obtained with the different temperatures. Figure 5.29 shows the change in calculated OH concentration from the three temperature values tested. Intuitively, error bars are smallest in non-absorbing regimes because changes in temperature have no effect on the amount of OH absorption at wavelengths that do not absorb OH.

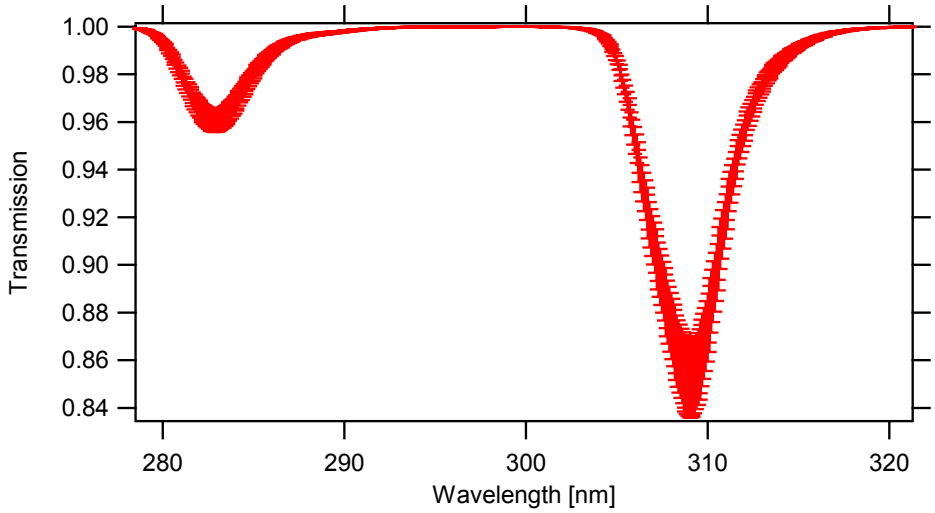

Figure 5-28. Absorption profile with error bars for ±100° C temperature input. 50% Argon, 8 mg/cycle.

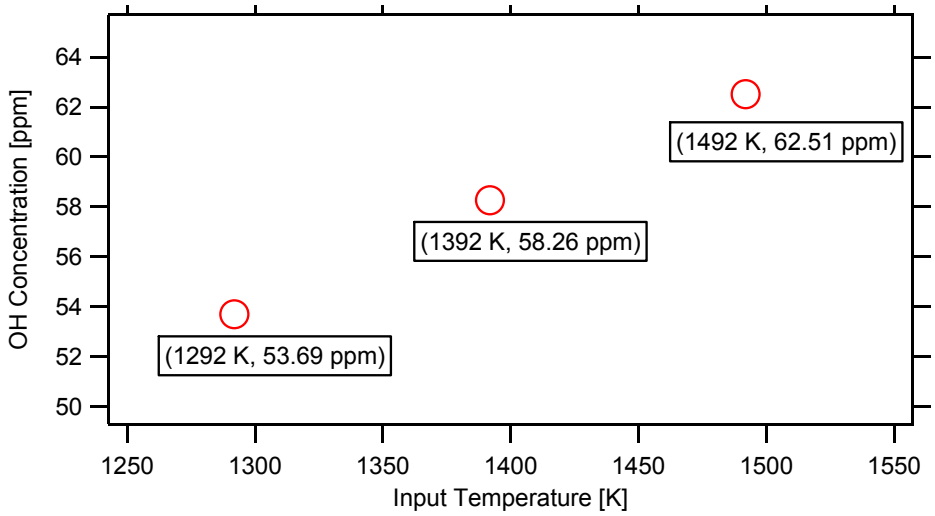

Figure 5-29. Change in calculated OH concentration versus input temperature.

5.5.2. Optical error

In general, the optical error contributed much less to the overall error than the temperature. ADU counts averaged over 200 cycles had a variance of mean on the order of 60-90 out of 20,000. Since error is calculated directly by the cycle averaging program

(Appendix E), the total error in a given transmission spectrum can be described by Equation 5.3.

$$Trans + \Delta_{Trans} = \frac{I + \Delta I}{I_0 + \Delta I_0} \tag{5.3}$$

For a division of errors, if the result of a calculation, x, is

$$x = a/b \tag{5.4}$$

then error in x, e_x, is described as:

$$e_x = x\sqrt{\left(\frac{e_a}{a}\right)^2 + \left(\frac{e_b}{b}\right)^2} \tag{5.5}$$

Figure 5.30 shows a sample spectrum with error bars that account for error in the incident and transmitted spectra as calculated from Equation 5.5.

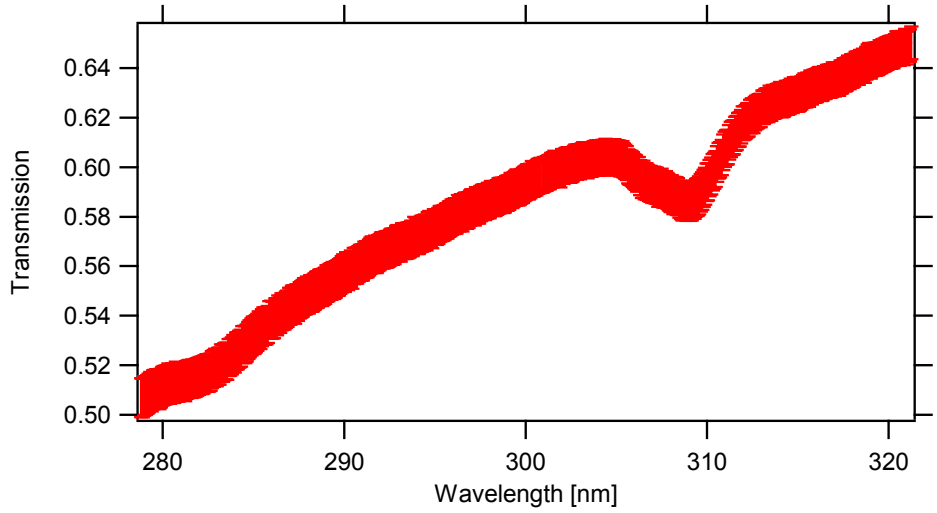

Figure 5-30. Transmission spectrum with error bars corresponding to the error due to noise in the optical data collected by the spectrograph. 100% Air, 10 mg/cycle.

5.5.3. Fitting errors from other absorption

Shown below in Figures 5.31 and 5.32 are some examples of output from the absorption curve fitter program, similar to Figure 4.14. Theoretical absorption profiles are compared with measured absorption on the left hand vertical axis, and the error squared between the two is graphed on the right hand axis. These are shown in order to make qualitative remarks about the errors seen here. Figure 5.33 is a fit from a low-absorbing case (100% air, 9 mg/cycle) shown to demonstrate SNR. The error is more visible qualitatively but it remains relatively low in magnitude compared to the absorption peaks.

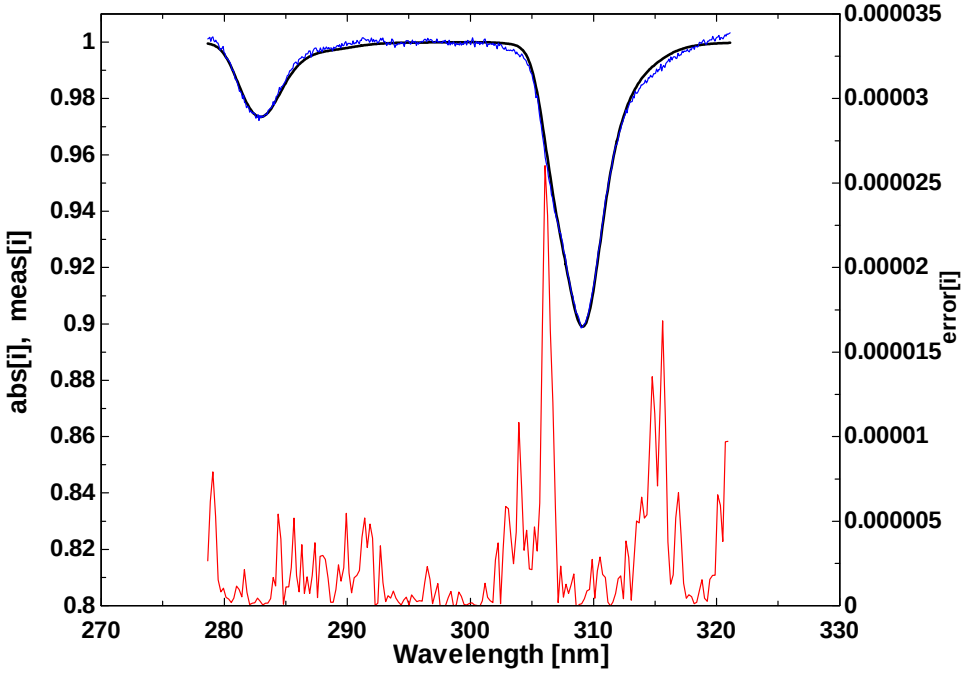

Figure 5-31. Calculated absorption, measured absorption (left axis), and error squared (right axis), 100% Air, 10 mg/cycle, 6.2 ATDC.

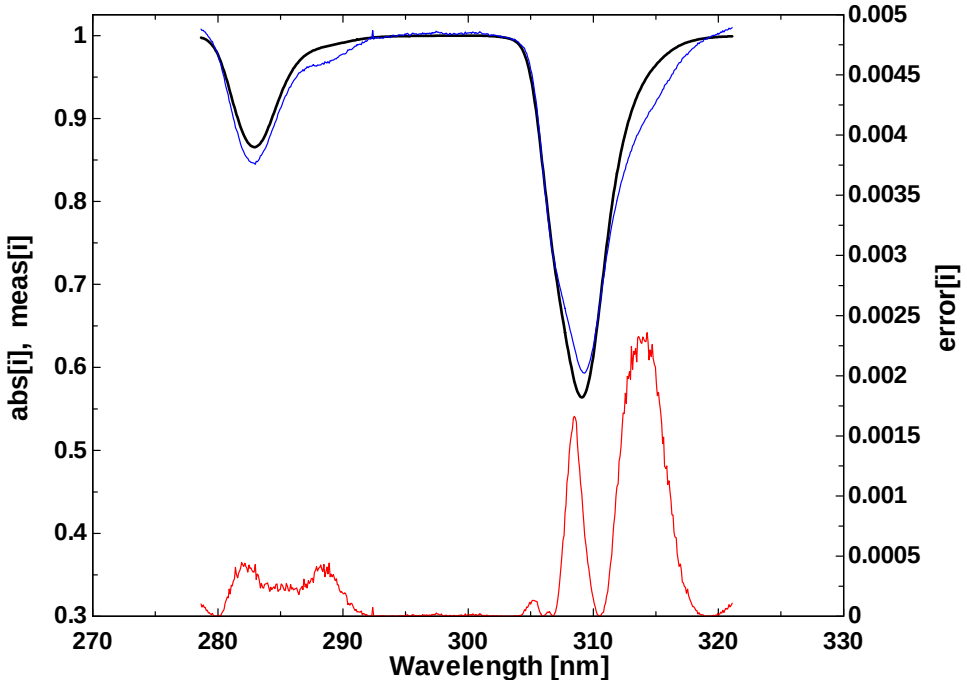

Figure 5-32. Calculated absorption, measured absorption (left axis), and error squared (right axis), 25% CO2, 16 mg/cycle, 15.2 ATDC.

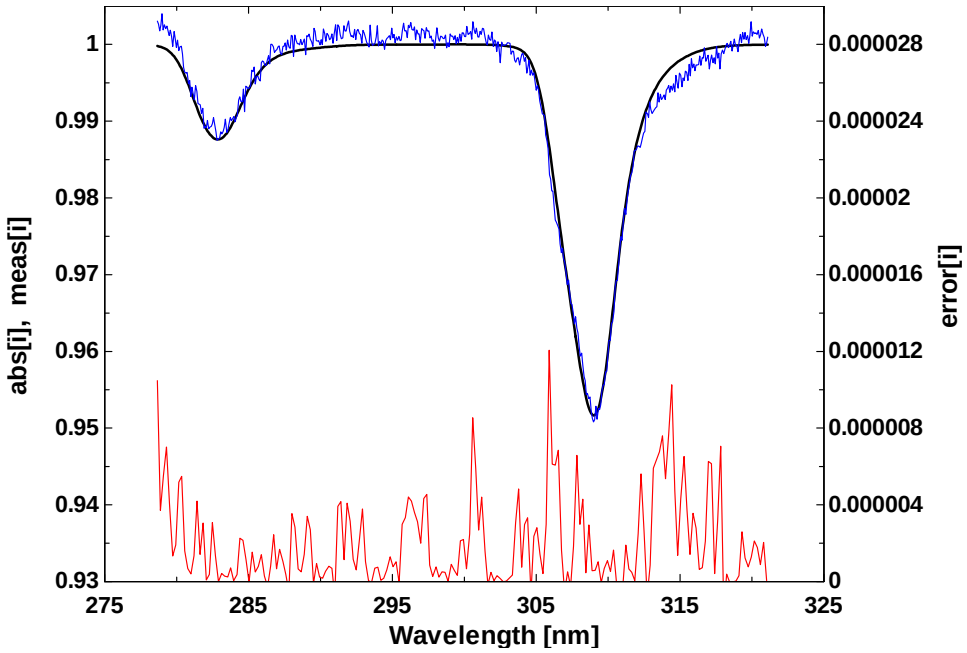

Figure 5-33. Calculated absorption, measured absorption (left axis), and error squared (right axis), 100% air, 9 mg/cycle, 9.8 ATDC. Shown to demonstrate signal-to-noise ratio. This case had the lowest measurable absorption for the air data, and SNR remains reasonably high.

The bulk of the error observed from the fitting scheme is extra absorption around 287, 305, and 315 nm. The fitter can only compare measured absorption to the absorption that OH alone should exhibit at the same temperature and pressure conditions. However, there are other intermediate species in the cylinder at the crank angle times investigated and they may absorb in these wavelengths as well. Absorption of species other than OH can be highlighted by examining a case at a low equivalence ratio that does not absorb OH. Figure 5.34 shows a sample run for CO_2 at 11 mg/cycle. The first spectrum taken is the one nearest to the top. As time passes, the transmittance drops due to combustion, and absorption features that do not resemble OH can be seen in the last ten spectra.

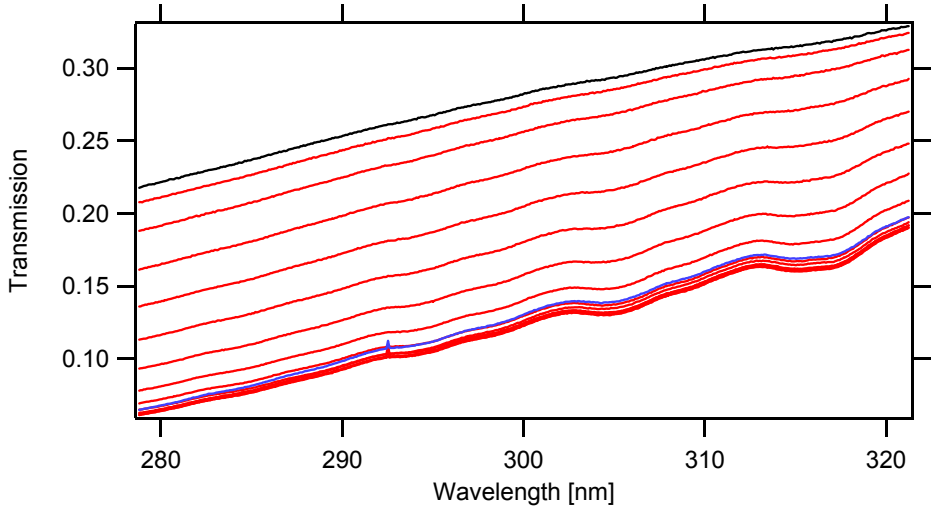

Figure 5-34. CO2 absorption at 11 mg/cycle.

Figure 5.35 selects one spectrum from Figure 5.34 (the 12th) in order to highlight three main absorption peaks around 294, 305, and 315 nm and one small peak around 285 nm.

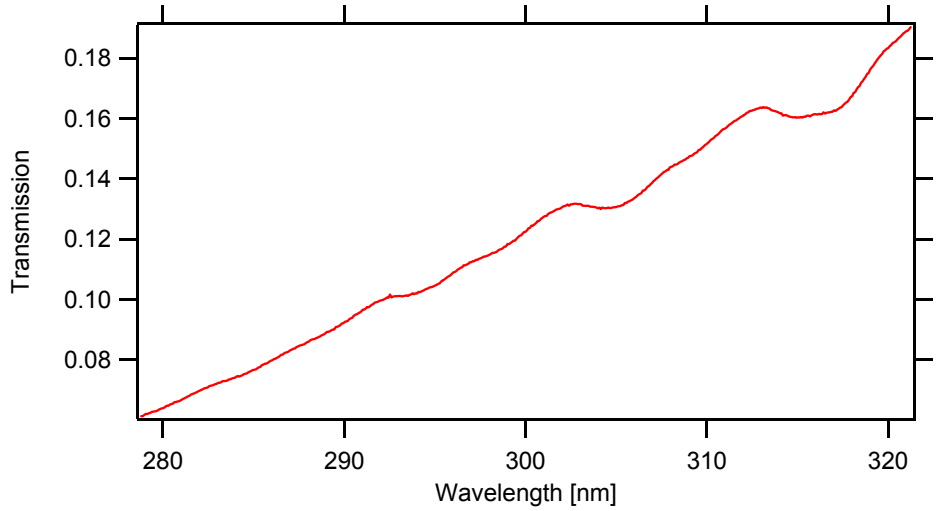

Figure 5-35. CO2 absorption from Figure 5.25, showing four absorbing wavelengths.

It is thought that this absorption is caused by formaldehyde, which is another combustion intermediate that appears between the first and second stages of combustion. The same spectral shape can be seen in other non-absorbing cases such as Figure 5.17 and before absorption starts in cases that do absorb (Figure 5.18 at -10 CAD).

An example of a formaldehyde absorption measurement by Bai *et al.* is shown in Figure 5.36 [25]. There are clearly absorption peaks near 285, 294, 305, and 315.

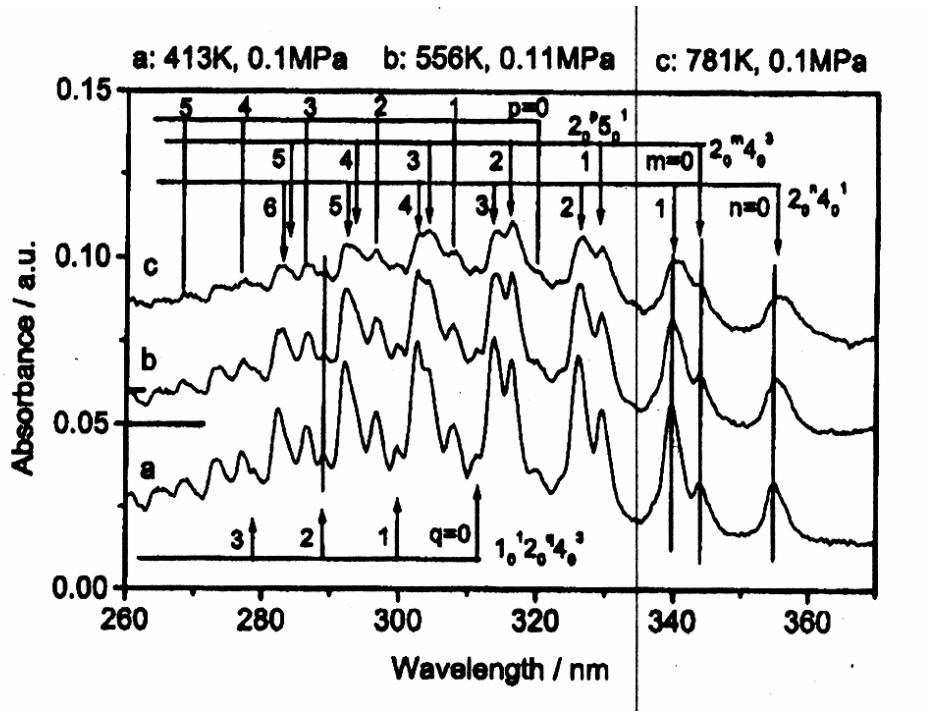

Figure 5-36. Vibronic $\tilde{A}^1A2 \leftarrow X^1A_1$ absorption spectra for different temperatures at 0.1 MPa. Curves (a), (b) and (c) have the respective offsets: 0.00, 0.06 and 0.05. Reprinted from [25].

These errors posed no threat to the integrity of the absorption calculation since they were small in magnitude relative to the height of the main OH peaks used to determine the mole fraction of OH.

5.6. Discussion of results

It is important to note that in the 100% air case, the 50% Argon case, and the 25% CO_2 case, as the equivalence ratio is decreased the transition from visible to undetectable OH absorption, low to high CO emission, and strong to weak second stage heat release occur at roughly the same fuel mass level. The CO_2 data were the only exception, where absorption ceased one data point before second-stage ignition disappeared and the CO emissions increased markedly.

Figure 5.37 is a plot of the maximum absorption in each of the three 100% air cases that do exhibit OH absorption. These are the cases with the highest fuel mass input per cycle and thus the highest equivalence ratios. The correct trend of a monotonic decrease OH concentration with decreasing equivalence ratio can be seen clearly. It should be noted that these same three data points are those that show a low CO emission (highlighted with circles in Figure 5.38) and a substantial second-stage heat release (Figure 5.39). The next data point below these in terms of fuel mass is that shown in Figure 5.17, and it is impossible to distinguish any OH absorption in that case. This is also the first case where the CO emissions increased by a large amount (highlighted with a square on Figure 5.38) and where second stage heat release was not strong.

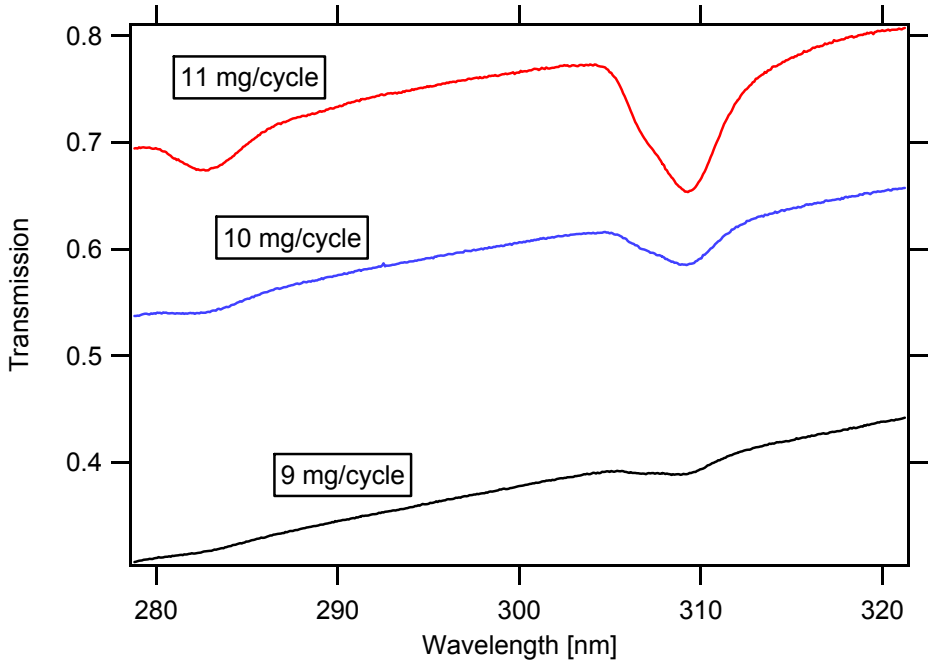

Figure 5-37. Peak absorption in 100% air cases.

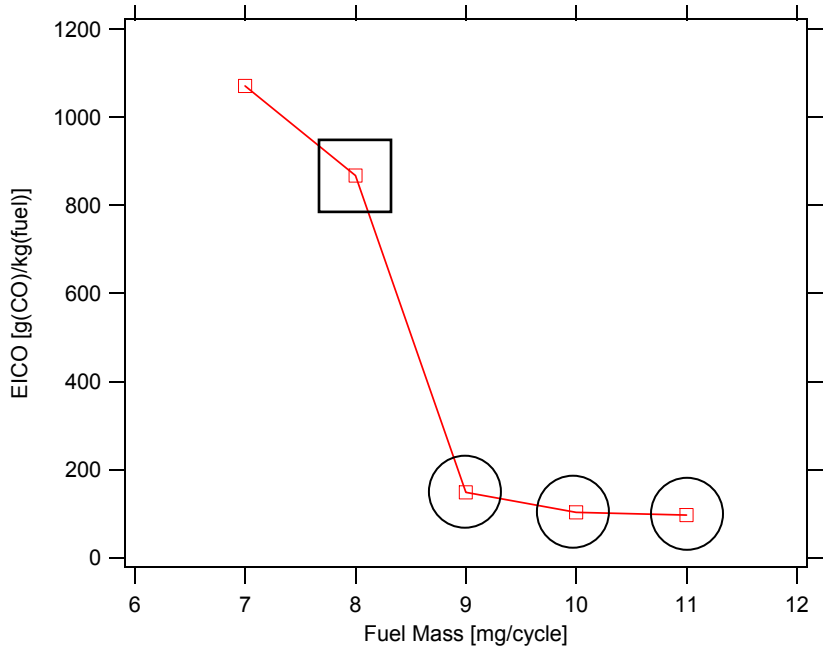

Figure 5-38. Replot of emissions data for 100% air cases. Data points are highlighted to illustrate the connection between absorption and combustion completeness. Circled data points are ones with apparent OH absorption (shown in Figure 5.37). The squared data point is the first point where no OH absorption can be distinguished.

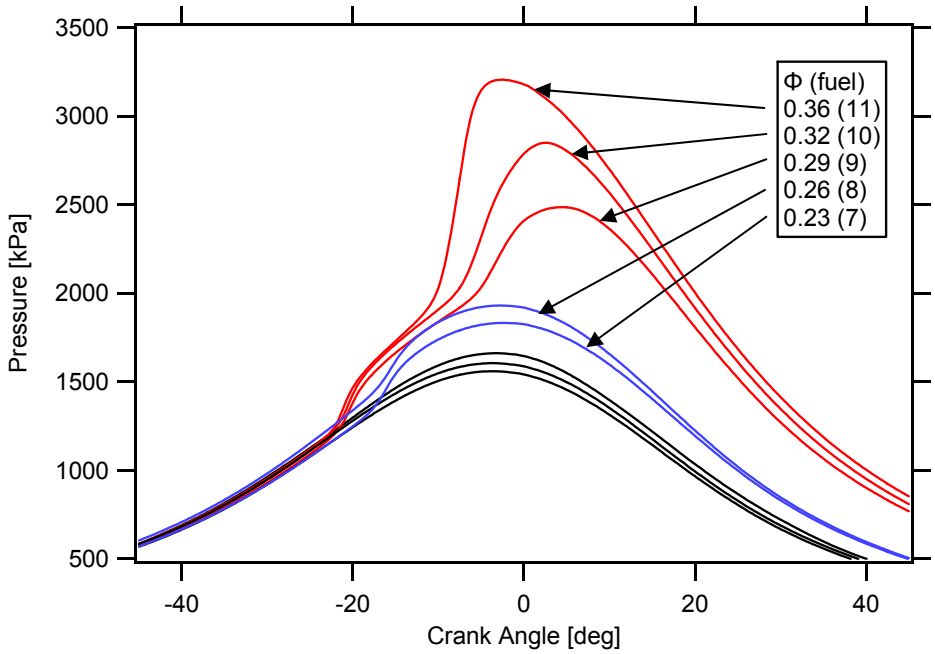

Figure 5-39. Replot of pressure data for 100% air cases. The top three equivalence ratios show a definite two-stage combustion, and correspond to the three cases in Figure 5.37. The two smallest equivalence ratios have no apparent second stage and show no absorption.

These data show a strong correlation between the amount of OH present in the cylinder and the eventual completeness of combustion. The low-load limit of the HCCI engine must lie somewhere in the regime between strong and weak second stage as this is where CO emission increases to an unacceptable amount. Since OH absorption follows the same transition, it can be used as a tool to help find this limit.

6. Conclusions

6.1. Project overview

The purpose of this research was to examine the light-load limit of the HCCI combustion process. Absorption spectroscopy of the OH molecule was used to quantify the OH concentration in the cylinder as a function of time. Optical results were compared to cylinder pressure and emissions data, with a focus on the transition from low to high engine-out CO emissions. The goal of the work was to experimentally verify a low-load emissions limit to practical HCCI combustion that has been predicted by detailed kinetic simulations.

6.2. Summary of results and conclusions

Absorption data was taken at a time resolution of 400 μs (~1.8 CAD at 600 RPM) using a "Fast Kinetics" acquisition mode on the CCD camera software so that the changes in absorption within a single cycle could be tracked. The size of the CCD allowed a 15-image burst of spectra to be taken and stored. Successive spectra assigned crank angle times based on the start of imaging and camera delay (see Figure 5.12) show that OH forms during the second-stage heat release just after TDC and remains in the cylinder well into the expansion stroke.

In addition to pure air, two diluted mixtures were tested to study the effect of mixture specific heats: 50% air/50% Argon; and 75% air/25% CO_2. These mixtures had lower and higher specific heats than air, respectively, and thus exhibited lower and higher temperature histories during the compression stroke. Emissions data showed low exhaust

CO concentrations at high fuel rates, and higher CO concentrations at low fueling rates. This agrees with theory and previous literature, which establishes a limit for HCCI combustion according to the percentage of fuel carbon exhausted as CO.

In general, OH absorption decreased monotonically with decreasing load, or the mass of fuel injected per cycle. For example, in the 100% air cases, calculated peak OH concentrations were 91, 49, and 19 ppm at 11, 10, and 9 mg/cycle, respectively. Other diluent cases showed similar results. These results matched with predictions since a mixture at a lower equivalence ratio will experience a smaller temperature rise and a weaker second stage ignition, thus a lesser concentration of OH radicals that form during the second stage. Peak OH concentration data show a correlation with temperature, which agrees with kinetic theory. Based on this information, it can be argued that the light-load limit of HCCI combustion is indeed a temperature constraint.

Of interest qualitatively, the detection limit for OH coincided with the onset of increased engine-out CO emissions and the transition from strong to weak second stage heat release. These data suggest that the three phenomena are linked. This agrees with theory since the OH radical is a main contributor to the completion of the overall CO $\rightarrow$ CO_2 oxidation reaction, *i.e.* the more OH present in the cylinder, the further the reaction can progress to the CO_2 side and the smaller the engine-out CO emissions. Additionally, the CO $\rightarrow$ CO_2 reaction is understood to be the main heat release mechanism. Where the progression to CO_2 is least, second-stage heat release is weakest. These tendencies have been demonstrated in the data. As emissions are the practical limitation to the light-load operation of the HCCI engine, this threefold transition is the light-load limit.

Broadband absorption from other chemical species was an issue, but it was found to be very smooth and regular in cases that exhibited OH absorption, and could be corrected by using a 2nd order polynomial fit. This worked extremely well, and evidence of a background is very hard to detect after the baseline correction. For cases early in the cycle, a residual signal was observed that matched the absorption spectrum of formaldehyde. The timing of this absorption tended to confirm this conclusion. Formaldehyde appears prior to the first stage of ignition and is consumed at the second stage. Each case where a claimed formaldehyde absorption can be seen is at a crank angle before OH absorption starts (prior to the second stage) or is a case where no OH absorption occurs at all (no second stage, thus the formaldehyde is not consumed).

In conclusion, this work has demonstrated that absorption spectroscopy is a valid method of determining in-cylinder OH concentration when temperature can be measured independently, and that OH absorption is a reasonable indicator of combustion completeness. Due to noise issues in the temperature data, the temperatures at which the transitions from desirable to undesirable operation happened could not be determined exactly. Given accurate temperature information, the low-load limit of the HCCI engine can be established and used as a baseline for future development.

6.3. Recommendations for future work

As the biggest source of error in this work was accurate measurement of temperature, that technique should be refined. The temperature could be taken as an average over a hundred cycles, as was done with OH and pressure, to improve signal-to-noise ratio.

On the other end, integrating a temperature iteration into the solution might also yield better results. If it can be assumed that OH concentration is in equilibrium at any given time, it is possible to calculate a temperature from the OH mole fraction and mixture composition. That temperature could be reinserted into the fitting scheme, a new concentration could be calculated, and the process repeated until the temperature converges.

The database of OH absorption data introduces a "bit noise" into the concentration calculation. This could be eliminated by recalculating absorption each time based on the measured temperature, rather than at preset intervals. It would require a considerable time investment, however, as the absorption information in the database is not easy to create. The bit noise could also be reduced simply by increasing the resolution of the database.

Recently, lasers that emit a broad spectrum in the UV range have become available. These would be excellent as a light source for an experiment such as this, especially since the input power has potential to be much greater than the 30W deuterium lamp used here. As a result, for a similar percentage of absorption, the power difference between incident and transmitted light in would be much greater and SNR would increase accordingly. This would be an excellent approach for examining the area between data points in this work where the transitions are made from low to no OH absorption.

References

[1] Onishi, S., Jo, S.H., Shoda, K., Jo, P.D., and Kato, S., 1979, "Active Thermo-Atmosphere Combustion (ATAC)—A new Combustion Profess for Internal Combustion Engines," SAE Paper No. 790501, 1979.

[2] Thring, R.H., "Homogeneous Charge Compression Ignition (HCCI) Engine," SAE Paper No. 892068, 1989.

[3] Stanglmaier, R.H., and Roberts, C.E., "Homogeneous Charge Compression Ignition (HCCI): Benefits, Compromises, and Future Engine Applications," SAE Paper No. 1999-01-3682, 1999.

[4] Noguchi, M., Tanaka, Y., Tanaka, T., and Takeuchi, Y., "A Study on Gasoline Engine Combustion by Observation of Intermediate Reactive Products during Combustion," SAE Paper No. 790840, 1979.

[5] Roberts, C.E., and Matthews, R.D., "Development and Application of an Improved Ring Pack Model for Hydrocarbon Emission Studies," SAE Paper No. 961966, 1996.

[6] Heywood, J.B., *Internal Combustion Engine Fundamentals*, McGraw-Hill, Inc. New York, NY, ISBN 0-07-028637-X, 1988.

[7] Dec, J.E., and Sjöberg, M., "An Investigation into lowest acceptable combustion temperatures for hydrocarbon fuels in HCCI engines," *Proceedings of the Combustion Institute*, Vol. 30 (2005) pp. 2719-2726.

[8] Najt, P.M., and Foster, D.E., "Compression-Ignited Homogeneous Charge Combustion," SAE Paper No. 830264, 1983.

[9] Gray III, A.W., and Ryan III, T.W., "Homogeneous Charge Compression Ignition (HCCI) of Diesel Fuel," SAE Paper No. 971676, 1997.

[10] Nakagome, K., Shimazaki, N., Miimura, K., and Kobayashi, S., "Combustion and Emissions Characteristics of Premixed Lean Diesel Combustion Engine," SAE Paper No. 970898, 1997.

[11] Turns, S.R., *An Introduction to Combustion*, 2nd Ed. McGraw-Hill, Inc. Madison, WI, ISBN 0-07-230096-5, 2000.

[12] Corcione, F.E., Merola, S.S., and Vaglieco, B.M., "Absolute NO and OH Concentrations During Diesel Combustion Process by Multiwavelength Absorption Spectroscopy," SAE Paper No. 2002-01-0892, 2002.

[13] Richter, M., Franke, A., Alden, M., Hultqvist, A., and Johansson, B., "Optical Diagnostics Applied to a Naturally Aspirated Homogeneous Charge Compression Ignition Engine," SAE Paper No. 1999-01-3649, 1999.

[14] Kranendonk, L.A., Walewski, J.W., Kim, T., and Sanders, S.T., "Wavelength-agile sensor applied for HCCI Engine Measurements," *Proceedings of the Combustion Institute*, Vol. 30 (2005) pp. 1619-1627.

[15] Kranendonk, L.A., Personal communication.

[16] Sanders, S.T., *Diode-lasers sensors for harsh environments with application to pulse detonation engines*, in Mechanical Engineering, Stanford University: Stanford, 2001.

[17] Bright, A.G., *Residual Gas Mixing in Engines*, M.S. Thesis, Department of Mechanical Engineering, University of Wisconsin-Madison, 2004.

[18] Probst, D.M. *Spray Mixing in Engines*, M.S. Thesis, Department of Mechanical Engineering, University of Wisconsin-Madison, 2001.

[19] Wiles, M.A., *Characterization of Operating Parameters' Authority on the Flow-Field Mixedness of a DISI Engine*, M.S. Thesis, Department of Mechanical Engineering, University of Wisconsin-Madison, 2003.

[20] Luque, J., Crosley, D.R., "LIFBASE: Database and Spectral Simulation Program (Version 1.5)," Report No. MP 99-009, SRI International, 1999.

[21] Davidson, D.F., Rohrig, M., Petersen, E.L., Di Rosa, M.D., and Hanson, R.K., "Measurements of the OH A-X (0,0) 306 nm absorption bandhead at 60 atm and 1735 K," JQSRT, 55 (6) pp. 755-762, 1996.

[22] Herbon, J.T., *Shock Tube Measurements of CH_3+O_2 Kinetics and the Heat of Formation of the OH Radical*, Ph.D. Thesis, Department of Mechanical Engineering, Stanford Univeristy, 2004.

[23] *A User's Guide to Andor CCDs, Version 2C*, Andor Technology Limited, 2003.

[24] Augusta, R., *Spectroscopic Investigation of Chemiluminescence in Gasoline Homogeneous Charge Compression Ignition Engine*, M.S. Thesis, Department of Mechanical Engineering, University of Wisconsin-Madison, 2004.

[25] Bai, X., Metz, T., Ossler, F., and Aldén, M., "Absorption of formaldehyde (H2CO) in the $\tilde{A}^1A_2 \leftarrow X^1A_1$ band system at elevated temperatures and pressures," *Spectrochimica Acta* Part A 60 (2004) pp. 821-828.

Appendix A – Intake air orifice calibration data*

*Orifice #3 calibration data by Bright [17].

	CONSTANT	MEASURED		CALCULATED			
	Flow	Upstream Pressure	Time	Flow	Flow Rate	Density	Mass Flow
	(ft^3)	*(psi)*	*(s)*	*(m^3)*	*(m^3/s)*	*(kg/m^3)*	*(kg/s)*
Orfice #1	4	14.4	79.84	0.11327	0.00142	1.25	0.0017733
	4	20	65.81	0.11327	0.00172	1.25	0.0021514
	4	25	57.81	0.11327	0.00196	1.25	0.0024491
	4	30	51.28	0.11327	0.00221	1.25	0.002761
	4	35	46.03	0.11327	0.00246	1.25	0.0030759
	4	40	41.96	0.11327	0.00270	1.25	0.0033743
	4	45	38.31	0.11327	0.00296	1.25	0.0036957
	4	50	35.53	0.11327	0.00319	1.25	0.0039849
	4	55	32.93	0.11327	0.00344	1.25	0.0042995
	4	60	30.5	0.11327	0.00371	1.25	0.0046421
	4	65	28.5	0.11327	0.00397	1.25	0.0049679
	4	70	26.96	0.11327	0.00420	1.25	0.0052516
Orfice #2	4	20	39.46	0.11327	0.00287	1.25	0.003588
	4	25	34.9	0.11327	0.00325	1.25	0.0040568
	4	30	30.62	0.11327	0.00370	1.25	0.0046239
	4	35	27.5	0.11327	0.00412	1.25	0.0051485
	4	40	24.81	0.11327	0.00457	1.25	0.0057067
	4	45	22.71	0.11327	0.00499	1.25	0.0062344
	4	50	20.93	0.11327	0.00541	1.25	0.0067646
	4	55	19.28	0.11327	0.00587	1.25	0.0073436
	4	60	17.84	0.11327	0.00635	1.25	0.0079363
	4	65	16.62	0.11327	0.00682	1.25	0.0085189
	4	70	15.62	0.11327	0.00725	1.25	0.0090643

Mass Flow vs. Upstream Pressure (Orfice #1)

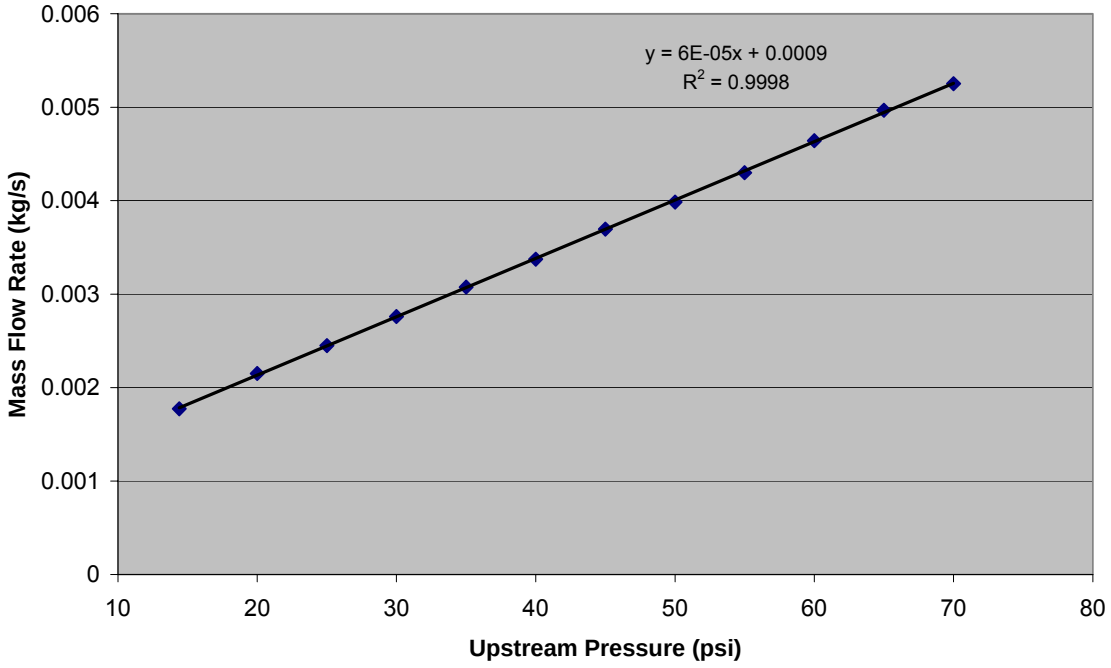

Mass Flow vs. Upstream Pressure (Orfice #2)

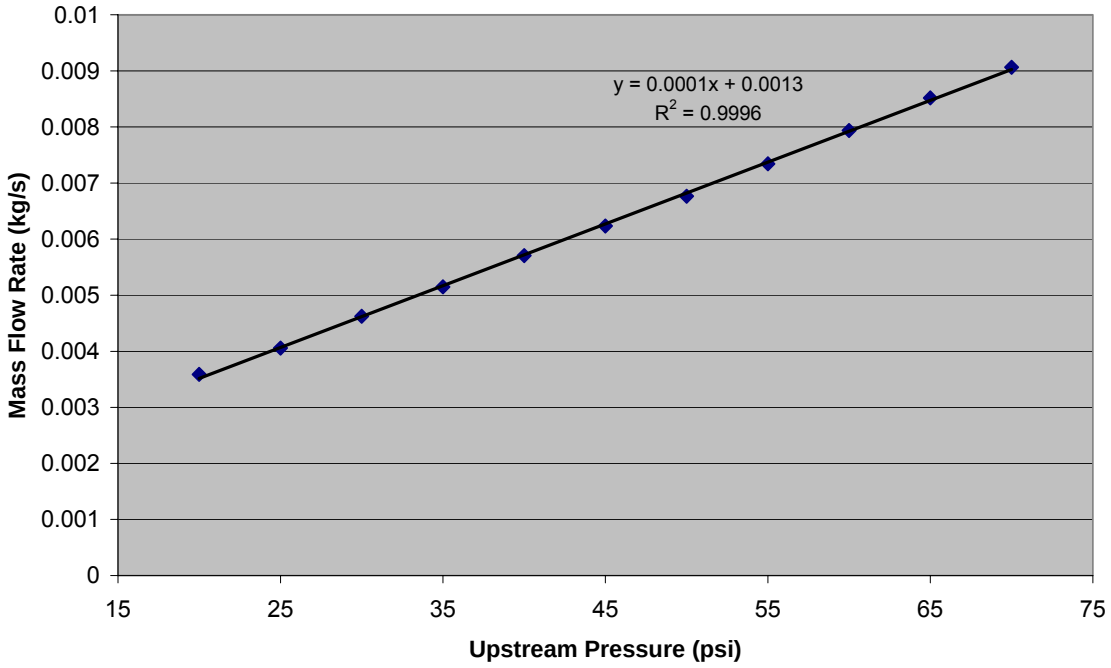

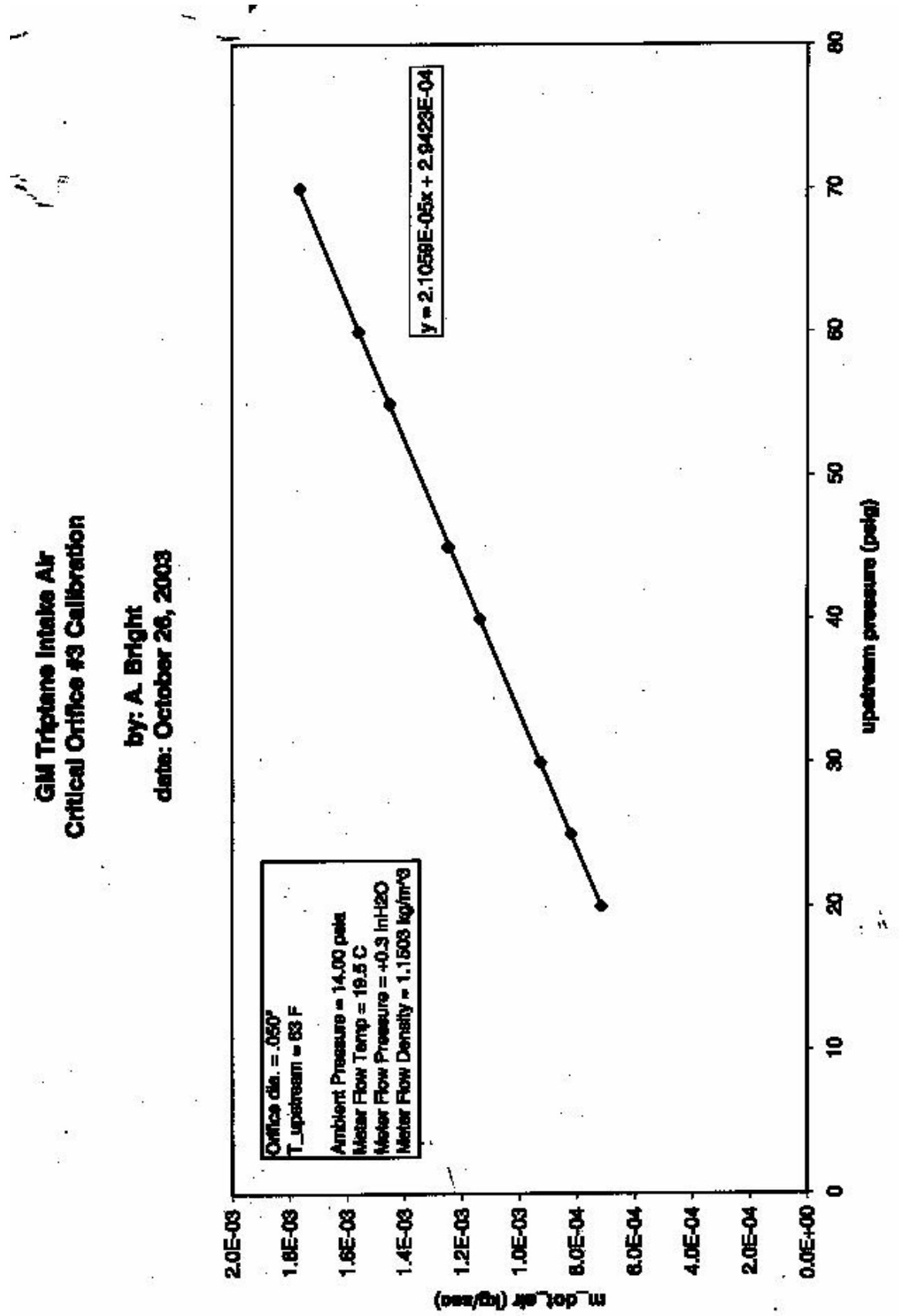
GM Triptane Intake Air
Critical Orifice #3 Calibration
by: A. Bright
date: October 26, 2003
Orifice dia. = .050"
T_upstream = 63 F
Ambient Pressure = 14.00 psia
Meter Flow Temp = 19.5 C
Meter Flow Pressure = +0.3 InH2O
Meter Flow Density = 1.1503 kg/m^3
y = 2.1059E-05x + 2.9423E-04
m_dot_air (kg/sec)
upstream pressure (psig)
2.0E-03
1.8E-03
1.6E-03
1.4E-03
1.2E-03
1.0E-03
8.0E-04
6.0E-04
4.0E-04
2.0E-04
0.0E+00
0
10
20
30
40
50
60
70
80

Appendix B – Emissions analyzer CO/CO_2 calibration data

CO @ 2.692%		Range = 0-5 V
% component	% Voltage	% CO
0	0.0025	0
10	0.0905	0.2692
20	0.1645	0.5384
30	0.229	0.8076
40	0.2865	1.0768
50	0.339	1.346
60	0.386	1.6152
70	0.427	1.8844
80	0.465	2.1536
90	0.5025	2.4228
100	0.538	2.692

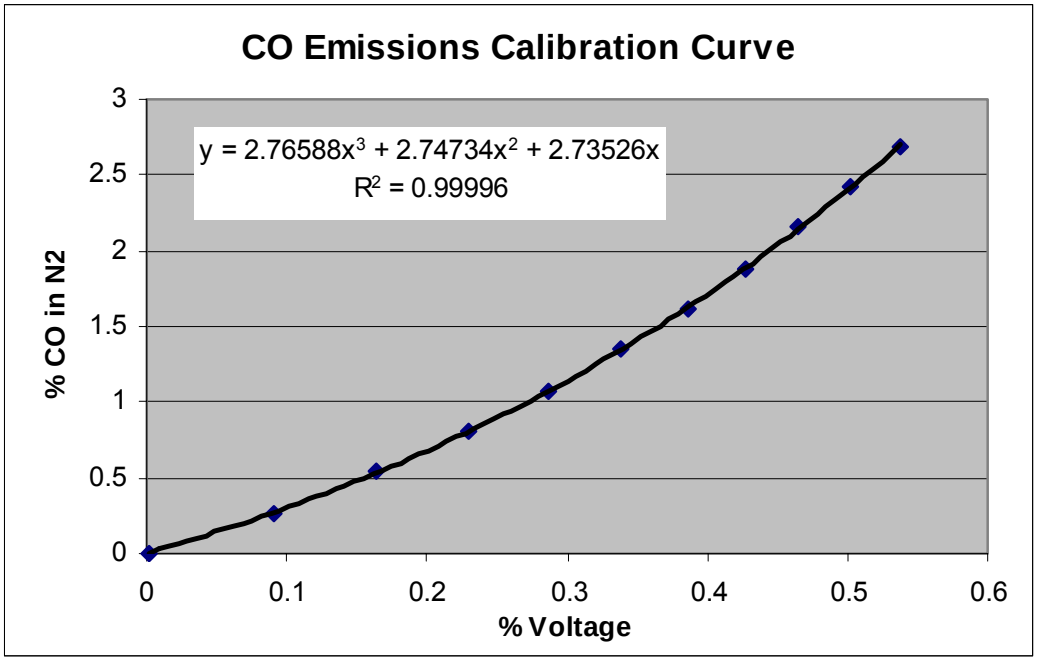

CO2 @ 10.1%		Range = 0-16%
% component	% Voltage	% CO2
0	0.0015	0
10	0.082	1.01
20	0.1575	2.02
30	0.231	3.03
40	0.298	4.04
50	0.3615	5.05
60	0.4205	6.06
70	0.477	7.07
80	0.532	8.08
90	0.582	9.09
100	0.631	10.1

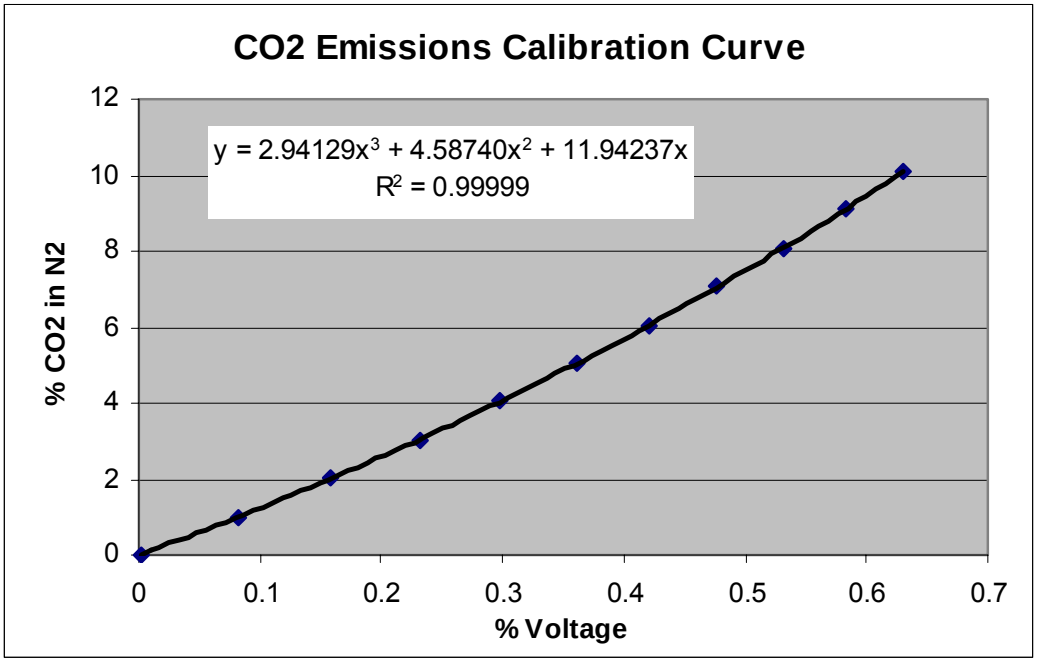

Appendix C – Peg and Convolve code

```
#include <stdio.h>
#include <math.h>
#include <string.h>
#include <fcntl.h>
#include <stdlib.h>
#include <errno.h>
#define PI 3.14159265

/*
This program reads data from the input file named "abs_input.dat" which
contains:

on line 1 the FWHM of a Gaussian spectrometer function in [m]
on each following line the names of two input and one output file.

The Herbon data are integrated as a function of frequency [cm^-1] over the
range cm1 -> cm2.  The Luque data are also integrated over the same frequency
region, then they are corrected to the Herbon data.  The Luque data are then
converted to wavelength and a convolution with the Gaussian is performed in
wavelength space.  The resulting output is written to the output file and the
process is repeated for as many lines as there are in the input file.

Written by:  Jaal Ghandhi
8 February 2005
*/

/*
Some changes to code format for clarity.  Included a print statement for the
variable "lcount".  Addition of EES lookup file header format.

By:  Sean Younger
Date: 21 July 2005
*/

main()
{
       double lfreq[30000], labs[30000], lwav[30000], lconv[30000];
       double cm1, cm2, /*c,*/ minwav, FWHM, consum, del;
       double hsum, lsum, hfreq, habs, delhfreq, factor;
       int i, j, hcount, lcount, lintcount, delta;
       char herb[40], luq[40], out_dat[40];

       //Define input filenames (Herbon, Luque, Data Ouput)
       FILE *hp,*lp,*op,*ip;

       //Define constants
       cm1=32685.0; //Start frequency of line matching [cm^-1]
       cm2=32705.0; //End frequency of line matching [cm^-1]

       /* File handling */

       if ((ip=fopen ("abs_input.dat","r")) == NULL)
       //Input matrix "abs_input.dat" lists input filenames
              printf("Can't open input file\n");
       fscanf (ip,"%lf",&FWHM);
```

```
	while (feof(ip)==0)
	{	//This is a big outer loop that reads from ip until end of file
		fscanf(ip,"%s\t%s\t%s\n", herb, luq, out_dat);
		//For each case read input and output file names
		printf("\n%s\t%s\n", herb, luq);

		if ((hp=fopen (herb,"r")) == NULL)
			printf("Can't open Herbon file\n");
		if ((lp=fopen (luq,"r")) == NULL)
			printf("Can't open Luque file\n");
		if ((op=fopen (out_dat,"w")) == NULL)
			printf("Can't open output file\n");

		//Read Herbon data

		for (i=1; i<=5; i++)
			while (fgetc(hp)!='\n');   //Get rid of first 5 lines

		fscanf(hp,"%lf%lf",&hfreq,&habs);
		fscanf(hp,"%lf%lf",&delhfreq,&habs);
		delhfreq=delhfreq-hfreq;   //Find the frequency interval
		hcount=0;
		hsum=0;
		while (fscanf(hp,"%lf",&hfreq)!=EOF)
		{
			fscanf(hp,"%lf\n",&habs);  //Read data line
			if ((hfreq>=cm1) && (hfreq<=cm2))
			{	//If you are inside the integration window add the
results
				hsum+=habs;
				hcount++;
			}
		}

		printf("%f\t%f\t%d\n", delhfreq,hsum,hcount);

		//Read Luque data

		lcount=0;	lsum=0;		lintcount=0;
		while (fscanf(lp,"%lf",&lfreq[lcount])!=EOF)
		{	//Read frequency
			while (getc(lp)!=',');	//Find the comma
			fscanf(lp,"%lf\n",&labs[lcount]);//Read absorption
			if ((lfreq[lcount]>=cm1) && (lfreq[lcount]<=cm2))
			{	//If you are inside the integration window, add the
results
				lsum+=labs[lcount];
				lintcount++;
			}
			lcount++;
		}

		printf("%f\t%f\t%d\n", lfreq[2]-lfreq[1],lsum,lintcount);

		//Peg Luque data and convert to wavelength

		factor=(hsum*delhfreq)/(lsum*(lfreq[2]-lfreq[1]));
		for (i=0; i<lcount; i++)
		{
			labs[i]*=factor;
			lwav[i]=1e-2/lfreq[i];
		}
		printf("%e\t%e\t%f\n", lwav[1],lwav[lcount-1],factor);
```

```
                minwav=lwav[lcount-2]-lwav[lcount-1];
                delta=(int)(4*FWHM/minwav+1);
                printf("%e\t%d\t%d\n",minwav,delta,lcount);

                //Perform convolution

                for (j=delta+1; j<lcount-delta; j++)
                {       //j is the index of the center wavelength
                        consum=0;
                        for (i=-delta; i<=delta; i++)
                        {
                                del=pow((lwav[j]-lwav[j+i])/FWHM,2);
                                consum+=labs[j+i]*exp(-del)*(lwav[j+i-1]-lwav[j+i]);
                        }
                        lconv[j]=consum/FWHM/sqrt(PI);
                }

                fprintf(op, "%d\t-2\n", lcount-((2*delta)+1));
                fprintf(op, "E6\tWavelength\t[m]\n");
                fprintf(op, "F5\tk_nu\n");

                for (j=delta+1; j<lcount-delta; j++)
                //j is the index of the center wavelength
                        fprintf (op,"%e\t%10.5f\n",lwav[j],lconv[j]);

                fclose (hp);
                fclose (lp);
                fclose (op);

        }       //End of "big" while loop

        fclose (ip);

} /* end of main */
```

Appendix D – Fast kinetics auto save procedure

This procedure covers the operation and calibration of the spectrograph as well as the practical aspects of using the Fast Kinetics Auto Save (FKAS) program written by Augusta [24].

1. **Connect the SMA fiber to the input slit of the spectrograph.**
2. **Turn on the computer that controls the CCD camera.**
3. **Turn on the spectrograph.** The grating set will scan wavelength and then move to a "home" position.
4. **Set the trigger parameter on the MotoTune software.** This is generally one of the spark signals.
5. **Open the Andor MCD software.** Double-click on the "Andor MCD" icon on the desktop.
6. **Turn on the camera cooler** by selecting Hardware > Temperature. The function of camera cooling is to eliminate as much dark noise as possible [23]. -40ºC is a good setting, and was used for these experiments.
7. **Change the trigger level setting.** Select Hardware > Shutter Control, and click on "TTL Low." This setting determines the size (in voltage) of the TTL signal needed to trigger the camera shutter. The system used here does not output enough voltage to use the "TTL High" setting.
8. **Calibrate the spectrograph.** Select Calibrate > X-calibration by Spectrograph. This opens a dialog, which allows the user to set the units and center wavelength of the wavelength axis. The scale is automatically determined by the software

based on the grating specifications. For these experiments, units were always nm and the spectra center wavelength set at 300 nm.

a. Make sure that the "Move Spectrograph" and "Apply Calibration to New Acquisitions" options are checked. If not, the calibration will not take place or the calibration will be lost upon the next acquisition.
b. Select the desired grating on the Grating pull-down menu.
c. Click "Calibrate" and wait for the spectrograph to position the grating. Clicking "Close" before this process is complete will cause the program to freeze.
d. A manual X-calibration can be performed by selecting Calibrate > Manual X-Calibration, which allows the user to manually label peaks identified by the software. Wavelength axis scale is then automatically calculated.

9. **Choose the acquisition parameters.** Select Acquisition > Setup Acquisition. This is where the software is set to Fast Kinetics mode. Choose settings as follows:
    a. **Acquisition Mode:** Fast Kinetics
    b. **Readout Mode:** Full Vertical Binning
    c. **Readout time per pixel:** 16 μsec
    d. **Vertical shift speed:** 4 μsec
    e. **Exposure time:** 400 μsec
    f. **Sub area height:** 25 rows
    g. **Number in series:** 15
10. **Choose the auto-save settings:** Select Acquisition > Auto Save Configuration.

a. Choose a directory to save files in.
b. Select a descriptive filename stem.
c. Make sure that “Auto Increment” is checked. If not, the auto save will attempt to overwrite with the same filename each time data is taken. Make sure that “Auto Save” is checked.

11. **Run the FKAS program.** Select File > Run Program by Filename.
    a. The program is located at: C:\Program Files\Andor Technology\Fast Kinetics Auto Save 2.pgm
    b. The program will prompt you to enter a number of data sets. This number is the number of times the program will repeat and auto save the files.
    c. The program run command can be repeated automatically by clicking on the “Run Program” icon on the toolbar.

The FKAS program is designed to take into account the readout time of the camera when taking multiple sets of data. Most process data which fast kinetics acquisition is designed to acquire happens quickly and in a repetitive process (consecutive cycles of the engine), the next data set time may occur before the camera is finished reading out the previous fast kinetics data set. The FKAS program skips cycles until the camera is finished reading out the previous data set. When the camera is clear, the next data set is recorded and the process repeated for the number of data sets entered. The auto-save/auto-increment function allows these data to be saved automatically with filenames that are similar [24].

Appendix E – Absorption data averager code

```
#include <stdio.h>
#include <math.h>
#include <float.h>
#include <string.h>
#include <fcntl.h>
#include <stdlib.h>
#include <errno.h>

/*
This program averages a set of tab-delimited, numerical ascii files.  It will
also include separate files which show the standard deviation and variance of
the mean of those averages.  Also, it creates a separate .txt file of the
average data in an EES lookup table format.  Data is taken from the camera
"backwards" with respect to wavelength, so this program reverses wavelength
data.

       Written by: Sean J. Younger
       Date written: April 8, 2005
*/

main()
{
       /* Counters */
       int row;
       int column;
       int file_count;

       /* Inputs */
       int num_files;
       int num_columns;
       int num_rows = 512;        // Based on size of camera, so hard coded...

       /* Data handling */
       float sheet[512][30] = {0};      // Initialize input array
       float sum[512][30] = {0};        // Initialize sum array
       float square_sum[512][30] = {0}; // Initialize "square-of-the-sums"
array
       float sum_square[512][30] = {0}; // Initialize "sum-of-the-squares"
array
       float average[512][30] = {0};    // Initialize average (output) array
       float stdev[512][30] = {0};      // Initialize standard deviation
(output) array
       float mean_var[512][30] = {0};   // Initialize mean variance
(delta_x_bar) array

       /* Filename handling */
       char file_stem[40];
       char file_name[50];
       char counter[5];
       char out_stem[40];
       char avg_name[50];
       char std_name[50];
       char vom_name[50];
       char lu_name[50];

       FILE *input,*avg,*std,*vom,*alu;
```

```
	/* Collect these parameters from the user */

	printf( "\nEnter the filename stem (all characters except ending
numeral): " );
	scanf( "%s", &file_stem );
	printf( "\nEnter number of columns (number of exposures in FK series +
1): " );
	scanf( "%d", &num_columns );
	printf( "\nEnter the number of files to be averaged: " );
	scanf( "%d", &num_files );
	printf( "\nEnter an output filename stem: " );
	scanf( "%s", &out_stem );

	strcpy ( avg_name, out_stem );
	strcpy ( std_name, out_stem );
	strcpy ( vom_name, out_stem );
	strcpy ( lu_name, out_stem );

	strcat ( avg_name, "_avg.asc" );
	strcat ( std_name, "_std.asc" );
	strcat ( vom_name, "_vom.asc" );
	strcat ( lu_name, "_lu.txt" );


	/* A big loop that gathers data from all consecutively numbered files */

	for( file_count = 0; file_count < num_files; file_count++ )
	{
		sprintf( counter, "%d", file_count );   // Make counter into a
string
		strcpy ( file_name, file_stem );        // Copy filename stem to
"FILENAME"
		strcat ( file_name, counter );    // Concatenate counter to stem
		strcat ( file_name, ".asc" );     // Add .asc extension


		// Open file with designated filename (read)
		if ((input=fopen( file_name, "r" )) == NULL)
			printf( "\nCan't open input file: %s!\n\n", file_name );

		// Read data into 2-D input array "sheet"
		for( row = 0; row < num_rows; row++ )
			for( column = 0; column < num_columns; column++ )
				fscanf( input, "%f", &sheet[row][column] );

		fclose ( input );   // Close input file

		// Compute running sum and running sum-of-the-squares
		for( row = 0; row < num_rows; row++ )
			for( column = 0; column < num_columns; column++ )
			{
				sum[row][column] += sheet[row][column];
				sum_square[row][column] +=
sheet[row][column]*sheet[row][column];
			}

		printf( "\n File %d input!", file_count );

	}	/* End for( file_count...) */
```

```
	/* Make sheet computations */

	for( row = 0; row < num_rows; row++ )
		for( column = 0; column < num_columns; column++ )
		{
			// Compute average
			average[row][column] = sum[row][column]/num_files;

			// Compute square-of-the-sum
			square_sum[row][column] =
		sum[row][column]*sum[row][column];

			// Compute standard deviation
			stdev[row][column] =
sqrt((num_files*sum_square[row][column] -
square_sum[row][column])/(num_files*(num_files - 1)));

			// Compute variance of the mean
			mean_var[row][column] =
		1.96*stdev[row][column]/sqrt(num_files);
		}

	/* Write data to files */

	if ((avg=fopen ( avg_name, "w" )) == NULL)
		printf("\nCan't open average output file!\n");
	if ((std=fopen ( std_name, "w" )) == NULL)
		printf("\nCan't open standard deviation output file!\n");
	if ((vom=fopen ( vom_name, "w" )) == NULL)
		printf("\nCan't open variance of mean output file!\n");
	if ((alu=fopen ( lu_name, "w" )) == NULL)
		printf("\nCan't open average lookup table output file!\n");

	fprintf( alu, "%d\t-%d\n", num_rows, num_columns );
	fprintf( alu, "F6\tWavelength\t[m^-9]\n" );
	for( column = 1; column < num_columns; column++ )
		fprintf( alu, "F6\tPic_%d\n", column);

	for( row = 0; row < num_rows; row++ )
	{
		// Write wavelength column (forwards)
		column = 0;
		fprintf( avg, "%f\t", average[row][column] );
		fprintf( std, "%f\t", stdev[row][column] );
		fprintf( vom, "%f\t", mean_var[row][column] );
		fprintf( alu, "%f\t", average[row][column] );

		// Write data columns (backwards)
		for(column = 1; column < num_columns; column++ )
		{
			fprintf( avg, "%f\t", average[num_rows - (row + 1)][column]
);	// Average data to "average.asc"
			fprintf( std, "%f\t", stdev[num_rows - (row + 1)][column]
);	// Standard dev. data to "stdev.asc"
			fprintf( vom, "%f\t", mean_var[num_rows - (row +
1)][column] );	// Variance of mean data to "mean_var.asc"
			fprintf( alu, "%f\t", average[num_rows - (row + 1)][column]
);	// Average data to "average_lu.txt"
		}
		fprintf( avg, "\n" );		// Newlines...
		fprintf( std, "\n" );
		fprintf( vom, "\n" );
		fprintf( alu, "\n" );
```

```
        }

        fclose ( avg );
        fclose ( std );
        fclose ( vom );
        fclose ( alu );

        printf( "Averaged %d files!", file_count );


} /* End main */
```

Appendix F – Spectral fit code

This is a program which compiles temperature, pressure, and optical data in order to calculate OH concentration.

A parametric table is used to minimize meanerr using concentration of OH as an independent variable.

Developed by: J.B. Ghandhi
Modified by : S.J. Younger

This determines the quadratic relationship used to model the broadband absorption. It is performed outside of the loop to speed up the procedure because it can be uniquely solved

lambda1 = 279

lambda2 = 297

lambda3 = 320

$$I\backslash I_{0,1} = \frac{\textbf{Interpolate}(\text{fired\$}, \text{'Wavelength'}, \text{DATASET\$}, \text{'Wavelength'} = \text{lambda1}) - \text{background}}{\textbf{Interpolate}(\text{motored\$}, \text{'Wavelength'}, \text{DATASET\$}, \text{'Wavelength'} = \text{lambda1}) - \text{background}}$$

$$I\backslash I_{0,2} = \frac{\textbf{Interpolate}(\text{fired\$}, \text{'Wavelength'}, \text{DATASET\$}, \text{'Wavelength'} = \text{lambda2}) - \text{background}}{\textbf{Interpolate}(\text{motored\$}, \text{'Wavelength'}, \text{DATASET\$}, \text{'Wavelength'} = \text{lambda2}) - \text{background}}$$

$$I\backslash I_{0,3} = \frac{\textbf{Interpolate}(\text{fired\$}, \text{'Wavelength'}, \text{DATASET\$}, \text{'Wavelength'} = \text{lambda3}) - \text{background}}{\textbf{Interpolate}(\text{motored\$}, \text{'Wavelength'}, \text{DATASET\$}, \text{'Wavelength'} = \text{lambda3}) - \text{background}}$$

$$I\backslash I_{0,1} = a0 + a1 \cdot \text{lambda1} + a2 \cdot \text{lambda1}^2$$

$$I\backslash I_{0,2} = a0 + a1 \cdot \text{lambda2} + a2 \cdot \text{lambda2}^2$$

$$I\backslash I_{0,3} = a0 + a1 \cdot \text{lambda3} + a2 \cdot \text{lambda3}^2$$

Spectra database lookup

$$\text{Tround} = 100 \cdot \textbf{Round}\left[\frac{T}{100}\right]$$

$$\text{Pround} = 5 \cdot \textbf{Round}\left[\frac{P}{5}\right]$$

a$ = **CONCAT$** (**String$** (Tround), '')

b$ = **CONCAT$** (a$, **String$** (Pround))

profile$ = **CONCAT$** (b$, '.dat')

Pressure and temperature data

$$P = \frac{\textbf{Interpolate}\ (\ \text{pressure\$},\ \text{'theta'}\ ,\ \text{'pressure'}\ ,\ \text{'theta'} = \ CA\ )}{101.3}$$

Lambert-Beer law loop

Rows = 512

L = 9.2 Length in cm

shift = 0.15 Wavelength shift in nm to get the peaks to match the Hg lamp calibration

background = 500 The average background is very steady at 500 counts

λ_j = **Lookup** (fired$, j , 1) – shift for j = 1 to Rows

$I_{0,j}$ = **Lookup** (motored$, j , DATASET$) – background for j = 1 to Rows

I_j = **Lookup** (fired$, j , DATASET$) – background for j = 1 to Rows

$k_{\nu,j}$ = **Interpolate** $\left[\ \text{profile\$},\ \text{'Wavelength'}\ ,\ \text{'k}_{nu}\text{'}\ ,\ \text{'Wavelength'} = \ 1.0 \times 10^{-9} \cdot \lambda_j\ \right]$ for j = 1 to

abs_j = **exp** ($-k_{\nu,j} \cdot P \cdot x_{OH} \cdot L$) for j = 1 to Rows

$$meas_j = \frac{I_j}{I_{0,j} \cdot (a0 + a1 \cdot \lambda_j + a2 \cdot \lambda_j^{\,2})} \quad \text{for } j = 1 \text{ to Rows}$$

$error_j = (meas_j - abs_j)^2$ for j = 1 to Rows

$$trans_j = \frac{I_j}{I_{0,j}} \quad \text{for } j = 1 \text{ to Rows}$$

$trans2_j = a0 + a1 \cdot \lambda_j + a2 \cdot \lambda_j^{\,2}$ for j = 1 to Rows

$$meanerr = \sum_{j=1}^{Rows} (error_j)$$

Appendix G – Heat release rate calculation code

This program is a single-zone heat release calculator
Developed by: J.B. Ghandhi
Last Modified: 22 November 2004

$\theta_{step} = 0.5$ Step size for integration

$p_m = \textbf{Interpolate}(LUT_{mot\$}, \text{'theta'}, press\$, \text{'theta'} = \theta)$

$dp_m = \textbf{Differentiate1}(LUT_{mot\$}, \text{'theta'}, press\$, \text{'theta'} = \theta)$

$p_f = \textbf{Interpolate}(LUT\$, \text{'theta'}, press\$, \text{'theta'} = \theta)$

$dp_f = \textbf{Differentiate1}(LUT\$, \text{'theta'}, press\$, \text{'theta'} = \theta)$

$p = p_f - p_m$

$dp = dp_f - dp_m$

$V = \textbf{Interpolate}(LUT\$, \text{'theta'}, \text{'volume'}, \text{'theta'} = \theta)$

$dV = \textbf{Differentiate1}(LUT\$, \text{'theta'}, \text{'volume'}, \text{'theta'} = \theta)$

$gam = 1.35$

$$\left[\frac{V}{gam - 1}\right] \cdot dp + gam \cdot p \cdot \left[\frac{dV}{gam - 1}\right] = dQ_{hr}$$

$$Q_{tot} = \int_{\theta_{start}}^{\theta_{end}} (dQ_{hr})\, d\theta$$

dQ_{hr} is the rate of heat release. This quantity is plotted versus crank angle in the heat release plots used in the thesis.

Appendix H – Diluted emissions calculation code

This program calculates an equivalence ratio based on atom balances, and exhaust emissions indices which are measures of mass flow of emissions out (in grams) normalized by mass flow of fuel into the cylinder (in kg).

Developed by: J.B. Ghandhi

Carbon:

$$1 + n_{CO2,f} = n_{CO2} + n_{CO} + n_{HC}$$

Hydrogen:

$$N + 2 \cdot n_{H2O,f} = 2 \cdot n_{H2O} + 2 \cdot n_{H2} + N \cdot n_{HC}$$

Oxygen:

$$2 \cdot n_{O2,f} + 2 \cdot n_{CO2,f} + n_{H2O,f} + 2 \cdot n_{air} = 2 \cdot n_{CO2} + n_{CO} + n_{H2O} + 2 \cdot n_{O2} + n_{NO} + 2 \cdot n_{SO2}$$

Nitrogen:

$$2 \cdot (n_{N2,f} + 3.76 \cdot n_{air}) = 2 \cdot n_{N2} + n_{NO}$$

Inert:

$$n_{I,f} = n_I$$

Sulfur:

$$n_{S,f} = n_{SO2}$$

$$C_{CO2} = 100 \cdot \frac{n_{CO2}}{n_{exh,d}}$$

$$C_{CO} = 100 \cdot \frac{n_{CO}}{n_{exh,d}}$$

$$C_{O2} = 100 \cdot \frac{n_{O2}}{n_{exh,d}}$$

$$3 \cdot C_{HC} = 100 \cdot \frac{n_{HC}}{n_{exh,d}}$$

$$C_{NO} = 100 \cdot \frac{n_{NO}}{n_{exh,d}}$$

$$C_{H2} = 100 \cdot \frac{n_{H2}}{n_{exh,d}}$$

$$C_{H2} = 0.25 \cdot N \cdot C_{CO}$$

Fuel properties

$$n_{exh,d} = n_{CO2} + n_{CO} + n_{H2} + n_{O2} + n_{N2} + n_{NO} + n_S + n_I + n_{HC}$$

$$A\backslash F = n_{air} \cdot 4.76 \cdot \left[\frac{\mathbf{MolarMass}\ (\text{'Air'})}{12 + N} \right]$$

$$EICO2 = 1000 \cdot C_{CO2} \cdot \mathbf{MolarMass}\ (\text{'CO2'}) \cdot \left[\frac{\frac{n_{exh,d}}{100}}{12 + N} \right]$$

$$EICO = 1000 \cdot C_{CO} \cdot \mathbf{MolarMass}\ (\text{'CO'}) \cdot \left[\frac{\frac{n_{exh,d}}{100}}{12 + N} \right]$$

$$EINO = 1000 \cdot C_{NO} \cdot \mathbf{MolarMass}\ (\text{'NO'}) \cdot \left[\frac{\frac{n_{exh,d}}{100}}{12 + N} \right]$$

$$EIHC = 1000 \cdot C_{HC} \cdot \frac{n_{exh,d}}{100}$$

$$n_{CO2,f} = percCO2dil \cdot 4.76 \cdot n_{air}$$

$$n_{H2O,f} = 0$$

$$n_{I,f} = percArgondil \cdot 4.76 \cdot n_{air}$$

$$n_{S,f} = 0$$

$$n_{N2,f} = 0$$

$$n_{O2,f} = 0$$

$$N = \frac{16}{7}$$